

1

CAMPINAS STATE UNIVERSITY

2

DOCTORAL THESIS

3

---

4 **Search of Z and Higgs boson decaying into  $\Upsilon + \gamma$**   
5 **in pp collisions at CMS/LHC**

---

6

7 *Author:*

Felipe Torres da Silva de Araujo

*Supervisor:*

Dr. José Augusto Chinellato

*Co-Supervisor:*

Dr. Alberto Franco de Sá Santoro

8

*A thesis submitted in fulfillment of the requirements  
for the degree of Doctor of Physics*

10

*in the*

11

Graduate Program of  
"Gleb Wataghin" Institute of Physics

12

13

August 20, 2020

<sup>14</sup> “Sometimes science is a lot more art than science. A lot of people don’t get that.”

<sup>15</sup>

Rick Sanchez

<sup>16</sup> “Então, que seja doce. Repito todas as manhãs, ao abrir as janelas para deixar entrar o sol ou o  
<sup>17</sup> cinza dos dias, bem assim, que seja doce. Quando há sol, e esse sol bate na minha cara amassada do  
<sup>18</sup> sono ou da insônia, contemplando as partículas de poeira soltas no ar, feito um pequeno universo;  
<sup>19</sup> repito sete vezes para dar sorte: que seja doce que seja doce que seja doce e assim por diante. Mas,  
<sup>20</sup> se alguém me perguntasse o que deverá ser doce, talvez não saiba responder. Tudo é tão vago como  
<sup>21</sup> se fosse nada.”

<sup>22</sup>

Caio Fernando Abreu

23 CAMPINAS STATE UNIVERSITY

24 *Abstract*

25 "Gleb Wataghin" Institute of Physics

26 Doctor of Physics

27 **Search of Z and Higgs boson decaying into  $\Upsilon + \gamma$  in pp collisions at CMS/LHC**

28 by Felipe Torres da Silva de Araujo

29 Searches for Standard Model Higgs and Z bosons decaying to a  $\Upsilon(1S, 2S, 3S)$  and a photon, with  
30 subsequent decay of the  $\Upsilon(1S, 2S, 3S)$  to  $\mu^+ \mu^-$  are presented. The analyses is performed using  
31 data recorded by CMS detector from proton-proton collisions at center-of-mass energy of 13 TeV  
32 corresponding to an integrated luminosity of  $35.86 \text{ fb}^{-1}$ . We put a limit, 95% confidence level, on  
33  $H \rightarrow \Upsilon(1S, 2S, 3S) + \gamma$  decay branching fraction at  $(6.8, 7.1, 6.0) \times 10^{-4}$  and on  $Z \rightarrow \Upsilon(1S, 2S, 3S) +$   
34  $\gamma$  decay branching fraction at  $(2.6, 2.3, 1.3) \times 10^{-6}$ . Contributions to operation, maintenance and  
35 R&D of Resistive Plate Chambers (RPC) of CMS are also presented. **EXPANDIR**

DRAFT

36

## *Acknowledgements*

37 I would like to thank:

- 38 • the Campinas State University for providing the institutional support for this study;
- 39 • the Rio de Janeiro State University for the cooperation with Campinas State University in  
40 their high-energy physics program. This was a key factor for this study;
- 41 • the National Council for Scientific and Technological Development (CNPq) for the financial  
42 support for this work;
- 43 • the European Laboratory for Particle Physics (CERN) for the construction and operation of  
44 the Large Hadron Collider (LHC);
- 45 • the Compact Muon Solenoid (CMS) collaboration for the construction, operation and provi-  
46 sion of the instrumental means for this study.

DRAFT

# 47 Contents

48	<b>Abstract</b>	iii
49	<b>Acknowledgements</b>	v
50	<b>1 Introduction</b>	1
51	<b>2 Rare Z and Higgs decays to quarkonia</b>	3
52	2.1 Standard Model and Local Gauge Invariance . . . . .	3
53	2.2 Recent results . . . . .	7
54	<b>3 Experimental Setup</b>	9
55	3.1 Tracker . . . . .	10
56	3.2 Electromagnetic Calorimeter . . . . .	10
57	3.3 Hadronic Calorimeter . . . . .	10
58	3.4 Muon System . . . . .	10
59	3.4.1 DT . . . . .	10
60	3.4.2 CSC . . . . .	10
61	3.4.3 RPC . . . . .	10
62	3.4.4 GEN . . . . .	10
63	3.5 Trigger and Data Acquisition . . . . .	10
64	3.6 Simulation, reconstruction and computing . . . . .	10
65	3.7 Particle Flow Algorithm . . . . .	10
66	<b>4 Physics Analysis</b>	11
67	4.1 Datasets and simulated events . . . . .	11
68	4.1.1 Data samples . . . . .	11
69	4.1.2 Simulated datasets . . . . .	11
70	4.2 Contribution of the $\Upsilon(nS)$ polarisation . . . . .	13
71	4.3 Kinematical studies using MC generator . . . . .	15
72	4.4 Event selection . . . . .	18
73	4.5 Trigger and physics object selection (Group I) . . . . .	18
74	4.5.1 Trigger . . . . .	18
75	4.5.2 Muon Identification . . . . .	18
76	4.5.3 Photon Identification . . . . .	20
77	4.5.4 Kinematical distributions . . . . .	20
78	4.6 Kinematical selection (Group II) . . . . .	30

79	4.7	Event categorization and yields . . . . .	38
80	4.7.1	R9 reweighting . . . . .	38
81	4.7.2	Event counting and yields . . . . .	38
82	4.8	Background modeling . . . . .	40
83	4.9	Signal modeling . . . . .	48
84	4.10	Systematic uncertainties . . . . .	54
85	4.10.1	Uncertainties on the predicted signal yields . . . . .	54
86	4.10.2	Uncertainties that affect the signal fits . . . . .	55
87	4.11	Modeling Cross checks . . . . .	58
88	<b>5</b>	<b>Results and conclusion</b>	<b>65</b>
89	5.1	The $CL_s$ formalism for upper limits setting at CMS . . . . .	65
90	5.2	Branching fraction upper limits . . . . .	67
91	<b>6</b>	<b>CMS Resistive Plate Chambers - RPC</b>	<b>71</b>
92	6.1	Resistive Plate Chambers . . . . .	71
93	6.1.1	Principles and operation modes . . . . .	71
94	6.2	CMS Resistive Plate Chambers . . . . .	73
95	6.2.1	Performance . . . . .	76
96	6.3	Contribution to the CMS RPC project . . . . .	79
97	6.3.1	RPC Operation - Shifts and Data Certification . . . . .	79
98	6.4	RPC Online Software . . . . .	79
99	6.4.1	iRPC R&D . . . . .	81
100	6.4.2	LS2 and the RPC Standard Maintenance . . . . .	87
101		HV maintenance . . . . .	87
102		LV and control maintenance . . . . .	88
103		Detector commissioning . . . . .	89
104	<b>Bibliography</b>		<b>91</b>

# <sup>105</sup> 1 Introduction

<sup>106</sup> INTRODUÇÃO  
<sup>107</sup> MOTIVAÇÃO PARA A ANÁLISE, RESUMO DO MÉTODO E RESULTADOS.  
<sup>108</sup> USAR UM PAPER DE CMS MUON PERFORMANCE PARA DIZER PORQUE  
<sup>109</sup> TRABALHAR COM DETECTORES DE MUONS

DRAFT

## <sup>110</sup> 2 Rare Z and Higgs decays to quarkonia

### <sup>111</sup> 2.1 Standard Model and Local Gauge Invariance

<sup>112</sup> Physics understands the matter and how it interacts in terms of two components: four funda-  
<sup>113</sup> mentals forces and elementary particles. From the weakest to the strongest, the fundamental forces  
<sup>114</sup> are: gravitational, weak, electromagnetic and strong. All share common characteristics like, being  
<sup>115</sup> mediated by particles <sup>1</sup>, being relevant within some effective range and have a associate a charge-like  
<sup>116</sup> quantity (i.e. intrinsic characteristic of the object) that defines whether or not, particles might be  
<sup>117</sup> subjected to a specific interaction.

<sup>118</sup> Along with the fundamental interactions, the Standard Model (or simply *SM*) defines every  
<sup>119</sup> existing matter in the Universe as a set of fundamental quantum objects, with properties that define  
<sup>120</sup> their interaction. Those objects are said to be fundamental since, in the context of the SM, they  
<sup>121</sup> are the smallest possible components of matter. We shall refer to them as fundamental particles.  
<sup>122</sup> There four of those mediating particles (force carriers), gluon ( $g$  - for the strong interaction), photon  
<sup>123</sup> ( $\gamma$  - for the electromagnetic interaction), Z and W (for weak interaction), all of them being vector  
<sup>124</sup> bosons (spin 1). Besides the interaction mediators, described at Table 2.1, the fundamental particles  
<sup>125</sup> are divided in two groups (*quarks* and *leptons*), with three generations, each. These are not force  
<sup>126</sup> carriers, but elementary particles, endowed with charge-like characteristics that allow them to by  
<sup>127</sup> exchange the vector bosons. Those are the building blocks of Matter in our Universe.

<sup>128</sup> Figure 2.1 summarizes their properties. Table 2.1 presents the relative strength and effective  
<sup>129</sup> range, for each one of the four fundamental interactions. The gravitational force is not study subject  
<sup>130</sup> of the Standard Model.

Table 2.1: Relative strength (with respect to the strong force) and effective range of action for the four fundamentals interactions.

	Mediator	Relative Strength	Effective Range
Gravitational	Graviton	$10^{-41}$	$\infty$
Weak	W and Z bosons	$10^{-16}$	$10^{-18}$ m
Electromagnetic	Photon	$10^{-3}$	$\infty$
Strong	gluons	1	$10^{-15}$ m

<sup>131</sup> There are six quark, up and down ( $u$  and  $d$  - first generation), charm and strange ( $c$  and  $s$  -  
<sup>132</sup> second generation), top and bottom ( $t$  and  $b$  - first generation), in increasing invariant mass order  
<sup>133</sup> of the generations. Since they interact thought all the three fundamental forces of the SM, they are  
<sup>134</sup> said to possess electrical charge, flavour and color. Their generational counterparts, the leptons,

---

<sup>1</sup>There is no evidence of the existence of the Graviton (force carrier associated to the gravitational force), even though, it is theorized by models that wish to comprehend gravity in a quantum perspective.

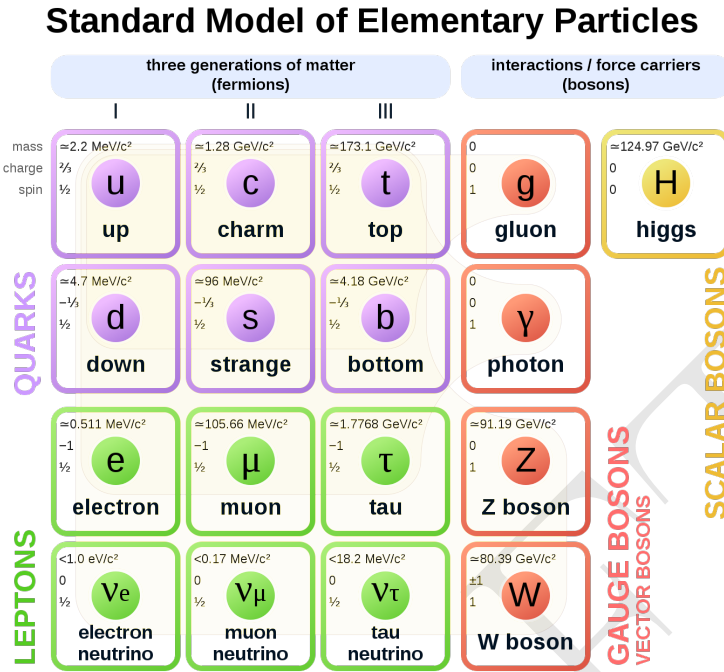


Figure 2.1: Elementary particles of the Standard Model, with their masses charges and spin. Those particles can be divided in two classes: boson (the interaction/force carriers) and the fermions, which are divided in three generations. Source: [1].

135 don't interact via strong interaction, that is why they are said to have only flavours and electric  
 136 charge. The leptons are electron and electron neutrino ( $e$  and  $\nu_e$  - first generation), muon and muon  
 137 neutrino ( $\mu$  and  $\nu_\mu$  - second generation) and tau and tau neutrino ( $\tau$  and  $\nu_\tau$  - third generation).  
 138 The neutrinos, within the SM, are massless, even though, experimental measurements have shown  
 139 that they actually have mass [2]. Neutrinos are also electrically neutral, meaning that they only  
 140 interact through weak interactions.

141 Figure 2.1 also presents the Higgs Boson ( $H$ ) which is part of the SM and shall be discussed  
 142 later.

143 Within the Standard Model, the theoretical basis that describe the fundamental interactions are  
 144 derived from a common principle: the local gauge invariance. According to Salam and Ward [3]:

145 "Our basic postulate is that it should be possible to generate strong, weak and electro-  
 146 magnetic interaction terms [...], by making local gauge transformations on the kinetic-  
 147 energy terms in the free Lagrangian for all particles."

148 Taking the Quantum Electrodynamics (QED) as an example: the quantum field theory that  
 149 describes the x

150 The fundamental theories that compose the Standard Model are all derived from a fundamental  
 151 principle call

152 The electromagnetic force, in the context of fundamental interactions, is described by a gauge  
 153 theory called quantum electrodynamics.

154 **Electroweak**

155      **Higgs discovery Production modes Decay modes**

156      **Yukawa coupling**

157      **Higgs results at CMS**

158      The rare decays of the Higgs boson [4, 5] to a quarkonium state and a photon provide a unique  
 159      sensitivity to the magnitude of the Yukawa couplings of the Higgs boson to quarks [6–8]. These  
 160      couplings are difficult to access on hadronic collisions through direct decay of Higgs in quark-  
 161      antiquark, due to the immense background from QCD [9].

162      Among the channels available to explore Yukawa’s couplings of light quarks [7, 8] are those  
 163      with heavy-quarkonia. The rare modes of decay of the Z boson have attracted attention focused on  
 164      establishing its sensitivity to New Physics [10], being configured as an alternative environment to  
 165      investigate the Yukawa couplings of the Higgs boson.

166      Also, the exclusive rare decays of vector bosons (Z, W) provide a favorable environment for test-  
 167      ing the factorization of QCD, thus allowing an approach in a context where the power of corrections  
 168      are definitely under control. The main focus of this kind of analysis are the hadronic radioactive  
 169      decays,  $Z \rightarrow M\gamma$ , where M can be a pseudoscalar or a vector meson ( $J/\psi, \phi, \Upsilon_n$ ).

170      They offer the perfect way to explore some of the leading order properties of the light-cone  
 171      distribution amplitudes (LCDAs) [11] of several mesons, but they present a difficulty, considering  
 172      that in the LHC energy scale the branching ratio of these processes is very small. There are  
 173      theoretical predictions [12, 13] that point out a branching ratio for several decay channels in the  
 174      Standard Model, as shown in the Table 2.2.

Physics Processes	Branching Ratio ( $\text{BR}_{SM}$ ):
$H \rightarrow \Upsilon(1S) + \gamma$	$5.22 \times 10^{-9}$
$H \rightarrow \Upsilon(2S) + \gamma$	$1.42 \times 10^{-9}$
$H \rightarrow \Upsilon(3S) + \gamma$	$9.10 \times 10^{-10}$
$Z \rightarrow \Upsilon(1S) + \gamma$	$4.88 \times 10^{-8}$
$Z \rightarrow \Upsilon(2S) + \gamma$	$2.44 \times 10^{-8}$
$Z \rightarrow \Upsilon(3S) + \gamma$	$1.88 \times 10^{-8}$

Table 2.2: Summary of cross section and branching ratio for  $H/Z \rightarrow \Upsilon(1S, 2S, 3S) + \gamma \rightarrow \mu^+ \mu^- + \gamma$  analysis. The effective cross-section will be discussed in section 4.1.2.

175      Recent studies on exclusive Higgs boson decays [14–16] in final states containing a simple vector  
 176      meson and a photon have caused interest in these physics topics. It was proposed to use these decays  
 177      as a possible way to explore non-standard Yukawa couplings of the Higgs boson. Such measures are  
 178      quite challenging in the LHC environment. The observation of hadronic decays of vector bosons  
 179      provides could provide a new frontier for the nature of heavy quarkonia production in hadronic  
 180      collisions.

181      Along the same lines, the simple exploration of rare SM decays, even in scenarios where anomalous  
 182      couplings are, in principle, ruled out by direct measurements [17], as in the case of this analysis  
 183      ( $H \rightarrow \Upsilon(nS) + \gamma$ ), are still important as a stress test of the SM and as reference for future mea-  
 184      surements. Specially the later one, when you consider that the small predicted cross sections from  
 185      Table 2.2, most probably, would imply that an observation of this decay would be unlikely even in  
 186      the HL-LHC [18].

This measurement is sensitive to the direct and indirect production (Figure 2.2). The *direct* process consists in the decay of boson (Higgs or Z) to a quark anti-quark pair, in which, one of the quarks radiates a photon and the pair hadronizes to a meson (a  $\Upsilon(nS)$ , for this study), while in *indirect* process, the decay happens to a  $\gamma\gamma^*(Z)$ , with the subsequent decay of the  $\gamma^*(Z)$  to a quark anti-quark that hadronizes.

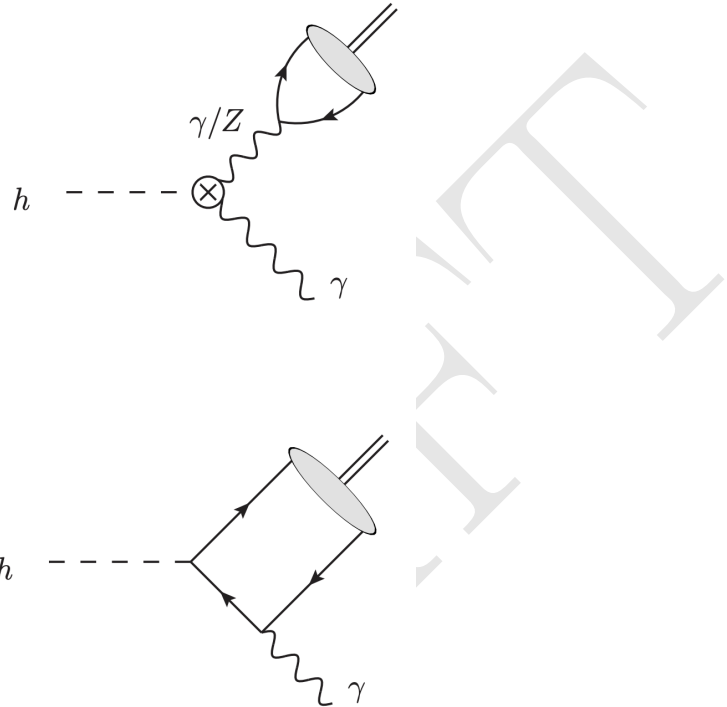


Figure 2.2: Example of leading order diagrams for the indirect (top) and direct (bottom) production mechanisms. In the diagrams, the  $h$  can also be understood as a  $Z$  boson.

Clearly, only the direct process is sensible to the Yukawa coupling of the boson with the quarks, but, since both processes are indistinguishable in their final state, the indirect process needs to be taken into account. In this study, a dimuon final state is used to tag the  $\Upsilon(nS)$ .

Even though there are different theoretical predictions for the cross section of this process and its twin brother ( $H \rightarrow J/\Psi + \gamma$ ), each one taking into account different levels of complexity, the 2013 paper [6], from G. Bodwin, F. Petriello, S. Stoynev and M. Velasco, summarizes very well and in a simpler manner, the most relevant phenomenological results on these decays. For the decay to  $J/Psi + \gamma$ , the quantum interference with the indirect amplitude, enhances the directed production, leading to a larger, and potentially observable, cross section. This is not true for the  $\Upsilon(nS) + \gamma$  decay, since the interference is destructive, diminishing the cross sections.

Another interesting aspect of this study is that, for both  $Hc\bar{c}$  and  $Hb\bar{b}$  direct coupling measurements are not sensible to the sign of the Yukawa coupling, while the presence of the indirect process in the  $H \rightarrow M + \gamma$  ( $M$  standing for  $J/Psi$  or  $\Upsilon(nS)$ ) decays resolve this ambiguity.

Finally, since the  $\Upsilon(nS) + \gamma$  decay has a much smaller cross section, because of the destructive quantum interference between direct and indirect production mechanisms, a small deviation in the  $Hb\bar{b}$  Yukawa coupling, can lead a large increase in the expected branching ratio, making this channel

208 sensible any non-Standard Model process that might interfere in this final state. This becomes clear  
 209 when we look to Figure 2.3.

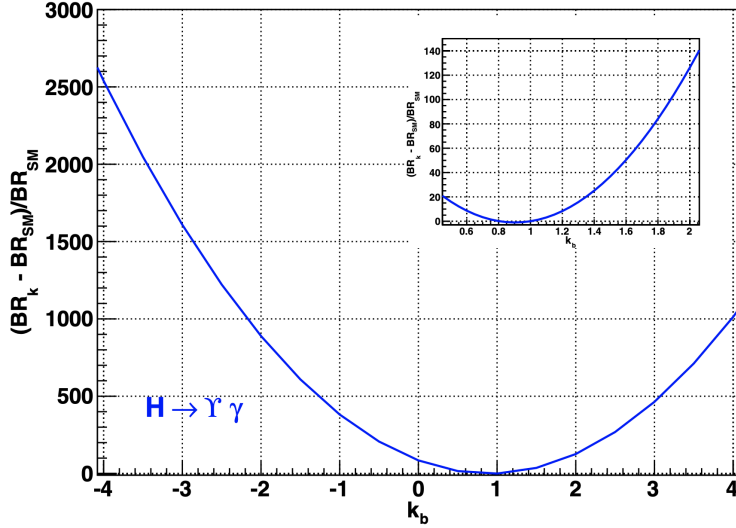


Figure 2.3: Expected relative variation of the branching ratio for the  $H \rightarrow \Upsilon(nS) + \gamma$  to  $k_b$ , where  $k_b = g(Hb\bar{b})/g(Hb\bar{b})_{SM}$  is the ratio for the observed and expected Yukawa coupling oh  $Hb\bar{b}$ . [6]

## 210 2.2 Recent results

211 The ATLAS experiment [19] already have two results on this decays [20, 21]. The first one  
 212 corresponds to data taken from 2015, while the former one, corresponds to data from 2016 (the  
 213 same data taking period to which this study refers).

214 The what concerns the most updated result, the study corresponded to  $36.1 \text{ fb}^{-1}$  at  $\sqrt{s} = 13$   
 215 TeV and no significant excess was found by the experiment. Upper limits for the were obtained,  
 216 assuming the Standard Model branching fractions predictions, at 95% confidence level, according  
 217 to table 2.3.

Decay	$\mathcal{BF}$ at 95% CL
$H \rightarrow J/\Psi + \gamma$	$< 4.5 \times 10^{-4}$
$H \rightarrow \Psi(2S) + \gamma$	$< 2.0 \times 10^{-3}$
$H \rightarrow \Upsilon(1S) + \gamma$	$< 4.9 \times 10^{-4}$
$H \rightarrow \Upsilon(2S) + \gamma$	$< 5.9 \times 10^{-4}$
$H \rightarrow \Upsilon(3S) + \gamma$	$< 5.7 \times 10^{-4}$
<hr/>	
$Z \rightarrow J/\Psi + \gamma$	$< 2.3 \times 10^{-6}$
$Z \rightarrow \Psi(2S) + \gamma$	$< 4.5 \times 10^{-6}$
$Z \rightarrow \Upsilon(1S) + \gamma$	$< 2.8 \times 10^{-6}$
$Z \rightarrow \Upsilon(2S) + \gamma$	$< 1.7 \times 10^{-6}$
$Z \rightarrow \Upsilon(3S) + \gamma$	$< 4.8 \times 10^{-6}$

Table 2.3: Observed upper limits, by the ATLAS experiment, on the branching fractions for the Higgs and Z decays (last result). Detailed comparisons with the results obtained in this study will be presented in chapter 5.

218 It is worth it to mention that the ATLAS papers present a broader analysis, including the decays  
 219 to  $J/\Psi + \gamma$  and  $\Psi(2S) + \gamma$ .

220 CMS [22] also have a result on  $J/\Psi + \gamma$  and  $\Psi(2S) + \gamma$  decay channel, of the Higgs and Z  
 221 boson [23]. The observed upper limit on the branching fraction for these decays are presented in  
 222 table 2.4.

Channel	Polarization	$\mathcal{B}F$ at 95% CL
$Z \rightarrow J/\Psi + \gamma$	Unpolarized	$< 1.4 \times 10^{-6}$
	Transverse	$< 1.5 \times 10^{-6}$
	Longitudinal	$< 1.2 \times 10^{-6}$
$H \rightarrow J/\Psi + \gamma$	Transverse	$< 7.6 \times 10^{-4}$

Table 2.4: Observed upper limits, by CMS, on the branching fractions for the Higgs and Z decays. The number are compatible with the ones obtained by ATLAS. The results presented for different polarization scenarios of the  $J/\Psi$ .

223 No result on the Z and Higgs decays to  $\Upsilon(nS) + \gamma$  have been published by CMS, yet.

224 The results presented here, are a subset of a broader topic related to the rare decays of Standard  
 225 Model (SM) boson, involving quarkonia. Sticking only to CMS results, we can cite:

- 226 • Search for Higgs and Z boson decays to  $J/\psi$  or  $\Upsilon$  pairs in proton-proton collisions at  $\sqrt{s} =$   
 227 13 TeV [24].
- 228 • Observation of the  $Z \rightarrow \psi\ell^+\ell^-$  decay in pp collisions at  $\sqrt{s} = 13$  TeV [25]. This one specifically,  
 229 is the first observation a such decay, involving a Z boson.

230 **verificar resultados se outros foram publicados.**

### 231 3 Experimental Setup

232 The central feature of the CMS apparatus is a superconducting solenoid of 6 m internal diameter,  
233 providing a magnetic field of 3.8 T. Within the solenoid volume are a silicon pixel and strip tracker,  
234 a lead tungstate crystal electromagnetic calorimeter (ECAL), and a brass and scintillator hadron  
235 calorimeter (HCAL), each composed of a barrel and two endcap sections. Forward calorimeters ex-  
236 tend the pseudorapidity coverage provided by the barrel and endcap detectors. Muons are detected  
237 in gas-ionization chambers embedded in the steel flux-return yoke outside the solenoid.

238 The silicon tracker measures charged particles within the pseudorapidity range  $|\eta| < 2.5$ . It  
239 consists of 1440 silicon pixel and 15 148 silicon strip detector modules. For non-isolated particles of  
240  $1 < p_T < 10 \text{ GeV}$  and  $|\eta| < 1.4$ , the track resolutions are typically 1.5% in  $p_T$  and 25–90 (45–150)  $\mu\text{m}$   
241 in the transverse (longitudinal) impact parameter [26]

242 The ECAL consists of 75 848 lead tungstate crystals, which provide coverage in pseudorapidity  
243  $|\eta| < 1.48$  in a barrel region (EB) and  $1.48 < |\eta| < 3.0$  in two endcap regions (EE). Preshower  
244 detectors consisting of two planes of silicon sensors interleaved with a total of  $3X_0$  of lead are  
245 located in front of each EE detector [27]. In the barrel section of the ECAL, an energy resolution of  
246 about 1% is achieved for unconverted or late-converting photons that have energies in the range of  
247 tens of GeV. The remaining barrel photons have a resolution of about 1.3% up to a pseudorapidity  
248 of  $|\eta| = 1$ , rising to about 2.5% at  $|\eta| = 1.4$ . In the endcaps, the resolution of unconverted or late-  
249 converting photons is about 2.5%, while the remaining endcap photons have a resolution between  
250 3 and 4% [28]. When combining information from the entire detector, the jet energy resolution  
251 amounts typically to 15% at 10 GeV, 8% at 100 GeV, and 4% at 1 TeV, to be compared to about  
252 40%, 12%, and 5% obtained when the ECAL and HCAL calorimeters alone are used.

253 Muons are measured in the pseudorapidity range  $|\eta| < 2.4$ , with detection planes made using  
254 three technologies: drift tubes, cathode strip chambers, and resistive plate chambers. The single  
255 muon trigger efficiency exceeds 90% over the full  $\eta$  range, and the efficiency to reconstruct and  
256 identify muons is greater than 96%. Matching muons to tracks measured in the silicon tracker  
257 results in a relative transverse momentum resolution, for muons with  $p_T$  up to 100 GeV, of 1% in  
258 the barrel and 3% in the endcaps. The  $p_T$  resolution in the barrel is better than 7% for muons with  
259  $p_T$  up to 1 TeV [29].

260 A two-tiered trigger system [30]. The first level (L1), composed of custom hardware processors,  
261 uses information from the calorimeters and muon detectors to select events at a rate of around  
262 100 kHz within a time interval of less than 4  $\mu\text{s}$ . The second level, known as the high-level trigger  
263 (HLT), consists of a farm of processors running a version of the full event reconstruction software  
264 optimized for fast processing, and reduces the event rate to around 1 kHz before data storage.

265 A more detailed description of the CMS detector, together with a definition of the coordinate  
266 system used and the relevant kinematic variables, can be found in Ref. [31].

267 falar do sistema de coordenadas e definir  $\eta$

268 **3.1 Tracker**

269 FAZER!

270 **3.2 Electromagnetic Calorimeter**

271 FAZER!

272 **3.3 Hadronic Calorimeter**

273 FAZER!

274 **3.4 Muon System**

275 FAZER!

276 **3.4.1 DT**

277 FAZER!

278 **3.4.2 CSC**

279 FAZER!

280 **3.4.3 RPC**

281 FAZER!

282 **3.4.4 GEN**

283 FAZER!

284 **3.5 Trigger and Data Acquisition**

285 FAZER!

286 **3.6 Simulation, reconstruction and computing**

287 FAZER!

288 **3.7 Particle Flow Algorithim**

289 FAZER!

# 290 4 Physics Analysis

291 **DEFINIR A ANALISE**

292 **EXPLICAR O PROCESSO E EXEMPLOS DE GRAFICO**

293 **EXPLICAR A ESTRATEGIA**

## 294 4.1 Datasets and simulated events

### 295 4.1.1 Data samples

296 The data sample used in this analysis consists of the 2016 13 TeV run with 25 ns bunch separation  
 297 recorded by CMS. This data sample is composed only by events that were certified from all CMS  
 298 subsystems and and reconstruction specialist as good for physics analysis.

299 This data sample corresponds to  $35.86 \text{ fb}^{-1}$  of integrated luminosity [32].

### 300 4.1.2 Simulated datasets

301 Data simulation at CMS is done by the use of Monte Carlo (from here on, simply called MC)  
 302 simulations the generates pseudo-random events, constrained by the physics of the related process to  
 303 which we are interested, including the effect of the produced particles interacting with the detector.  
 304 The simulation starts with the **hard-scattering** process, at parton (constituents of the proton)  
 305 level, done usually, by matrix element generators, which impose to the incoming and outgoing  
 306 partons, the dynamics of the simulated process, according to some pre-defined theoretical model.  
 307 Along the hard interaction simulation, the **fragmentation** process takes place. Since the the matrix  
 308 element generator provide information on the parton level, it is necessary to extract the momentum  
 309 distribution of the parton as a function of the  $Q^2$  (transferred momentum) of the process. TO do  
 310 so, MC generators use the PDFs (parton distribution functions) to sample those values, accordingly.  
 311 The matrix element formalism also allows the simulation of the process, taking into account, different  
 312 orders of perturbations, like NLO (next-to-leading-order), NNLO (next-to-next-to-leading-order),  
 313 and so on.

314 After the hard-scattering, the **showering** process simulates the radiation emission by gluons  
 315 and quarks in the initial and final states. Along the hard interaction, the other proton constituents  
 316 may also interact through soft interaction. This part of the simulation is called **multiple parton**  
 317 **interaction** (MPI). The last components of the simulation is the **hadronization** and the **decay**  
 318 **of heavy hadrons and leptons**. The former one, imposes the QCD confinement to low energy  
 319 quarks and gluons <sup>1</sup>, while the latter one, implements specific models to decays heavy hadrons and  
 320 leptons, like  $B$  hadrons and taus.

---

<sup>1</sup>QCD forbids coloured objects to exist in non-asymptotic states. They must decays to more complex systems, until they form stable colorless states.

Usually, different generators are used to simulate a process. Each specialized in one or more steps.

A summary of the signal and background MC samples used is presented in Table 4.1. These simulated data are comparable with the proton-proton collision using 2016 data conditions and the **pileup**<sup>2</sup> events are added to the simulated event in this step. The pileup events distribution used is modeled as a Poisson pdf (probability distribution function) with mean of 23 events, as recommended by CMS. Detector response in the MC samples is simulated using a detailed description of the CMS detector, based on GEANT4 [33].

The signal MC samples are simulated for the Higgs bosons decaying to  $\Upsilon(nS)(\rightarrow \mu\mu) + \gamma$  channels with POWHEG v2.0 [34–36], at next-to-leading order (NLO) of Feynman graphs computation, for the following production modes: gluon-gluon fusion (ggF), vector boson fusion (VBF), associated production (VH) and associated top production (ttH), with cross-section summarized at table 4.1. A extensive review of these production modes can be found at [37]. The PYTHIA 8 generator [38, 39] is used for hadronization and fragmentation with underlying event tune CUETP8M1 [40]. The parton distribution functions (pdf) NNPDF3.0 [41] are used.

For Z decaying to  $\Upsilon(nS)(\rightarrow \mu\mu) + \gamma$  channels, the signal samples are simulated with MADGRAPH 5 \_MC@NLO 2.6.0 matrix element generator [42] at next leading order and the PYTHIA 8 generator [38, 39] for hadronization and fragmentation with underlying event tune CUETP8M1 [40].

The Drell-Yan process,  $pp \rightarrow Z \rightarrow \mu\mu\gamma_{FSR}$ , results in the same final state as the signal. This process exhibits a peak in the three-body invariant mass,  $m_{\mu\mu\gamma}$ , at the Z boson mass,  $m_Z$ , and it is a resonant background for this channel, therefore referred to as a Peaking Background.

It is taken into account when deriving the upper limit on the branching fraction for  $Z \rightarrow \Upsilon(nS) + \gamma \rightarrow \mu\mu + \gamma$ . The MADGRAPH 5 \_MC@NLO 2.6.0 matrix element generator [42] at leading order, interfaced with PYTHIA 8.226 for parton showering and hadronization with tune CUETP8M1 [40], is used to generate a sample of these resonant background events. The photons in these events are all produced as final-state radiation from the  $Z \rightarrow \mu\mu$  decay and therefore the  $m_{\mu\mu\gamma}$  distribution peaks at the Z boson mass and there is no continuum contribution.

Similarly, the Higgs boson Dalitz decay [43],  $H \rightarrow \gamma^*\gamma \rightarrow \mu\mu + \gamma$ , is a Peaking Background (resonant) to  $H \rightarrow \Upsilon(nS) \rightarrow \mu\mu + \gamma$ . It is simulated at NLO with MADGRAPH 5 \_MC@NLO 2.6.0 matrix element generator [42] at next-to-leading order and the PYTHIA 8 generator [38, 39] for hadronization and fragmentation with underlying event tune CUETP8M1 [40]. This Higgs Dalitz Decay sample, was generated only for the ggF production mode, but its cross-section was rescaled to the full Higgs cross-section. This process will present a small contribuition of selected events, so this approximation should be sufficient for the Higgs Peaking Background modeling.

There are also background processes that do not give resonance peaks in the three-body invariant mass spectrum. They are modeled from data, as it will be explained latter in more details.

---

<sup>2</sup>Each LHC collision recorded by CMS, is composed not by a single  $pp$  interaction, but by a bunch of protons crossing. In this case, a hard interaction is actually surrounded by many soft interaction between adjacent protons. The extra activity produced in these interactions, and caught by the detector, is called **pileup** and has its signal mixed with the hard one. Since, during the data taking, the number of pileup interactions varies according to the instantaneous luminosity, the MC are mixed some soft interaction only sample, called Minimum Bias. The number of mixed soft interaction (pileup events) is governed by a Poisson distribution with a pre-defined mean. The MC samples are then reweighted to match the same distribution of primary vertexes for the corresponding Data. Systematics related to this procedure will be discussed later.

Physics Processes	Branching Ratio ( $BR_{SM}$ )	Effective $\sigma$ (in pb)	Generator	Sample Type
$H \rightarrow \Upsilon(1S) + \gamma$	$5.22 \times 10^{-9}$	$7.14 \times 10^{-9}$	POWHEG 2.0	Signal
$H \rightarrow \Upsilon(2S) + \gamma$	$1.42 \times 10^{-9}$	$1.51 \times 10^{-9}$	POWHEG 2.0	Signal
$H \rightarrow \Upsilon(3S) + \gamma$	$9.10 \times 10^{-10}$	$1.10 \times 10^{-9}$	POWHEG 2.0	Signal
$Z \rightarrow \Upsilon(1S) + \gamma$	$4.88 \times 10^{-8}$	$6.80 \times 10^{-5}$	MADGRAPH 5	Signal
$Z \rightarrow \Upsilon(2S) + \gamma$	$2.44 \times 10^{-8}$	$2.69 \times 10^{-5}$	MADGRAPH 5	Signal
$Z \rightarrow \Upsilon(3S) + \gamma$	$1.88 \times 10^{-8}$	$2.34 \times 10^{-5}$	MADGRAPH 5	Signal
H Dalitz Decay	$3.83 \times 10^{-5}$	$2.13 \times 10^{-3}$	MADGRAPH 5	Peaking Background
$Z \rightarrow \mu\mu\gamma_{FSR}$	—	$7.93 \times 10^{-2}$	MADGRAPH 5	Peaking Background

Table 4.1: Datasets simulated (MC) for 2016 conditions. Assuming that  $\sigma(pp \rightarrow H)$ , taking into consideration all the simulated Higgs production modes, is  $55.13 \text{ pb}$  [44] and  $\sigma(pp \rightarrow Z \rightarrow \mu\mu)$  is  $57094.5 \text{ pb}$ , including the next-to-next-to-leading order (NNLO) QCD contributions, and the next-to-leading order (NLO) electroweak corrections from fewz 3.1 [45] calculated using the NLO PDF set NNPDF3.0, with the phase space selection in invariant mass of the dimuon system of  $m_{\mu\mu} > 50 \text{ GeV}$ . For the Higgs Dalitz  $\sigma$ , we consider only the gluon fusion contribution ( $\sigma_{ggF} = 48.6 \text{ pb}$ ) [44]. The Higgs Dalitz Decay  $BR_{SM}$  and the  $Z \rightarrow \mu\mu\gamma_{FSR}$  were obtained with MCFM 6.6 [46] (as in the CMS search for Higgs Dalitz Decay in at  $\sqrt{s} = 8 \text{ TeV}$  [47]) and with MADGRAPH 5 \_MC@NLO, respectively. The  $BR_{\Upsilon(1S,2S,3S) \rightarrow \mu\mu}^{PDG} = (2.48, 1.93, 2.18) \times 10^{-2}$  is quoted from Particle Data Group report (PDG) [2]. The "Effective  $\sigma$ " for the signal samples is  $\sigma(pp \rightarrow Z(H)) \times BR_{SM} \times BR_{\Upsilon(nS) \rightarrow \mu\mu}^{PDG}$ .

357     The number of simulated events is rescaled by the Effective  $\sigma$ , from table 4.1, in order to match  
 358      $35.86 \text{ fb}^{-1}$  of integrated luminosity, from the recorded data. Being  $N = \sigma\mathcal{L}$ ,  $N$  in the number of  
 359     events for a process,  $\sigma$  is the cross-section and  $\mathcal{L}$  is the integrated luminosity, the reweighting factor,  
 360     for a simulated sample is:

$$w_{MC} = \frac{\sigma\mathcal{L}}{N_{sim}}, \quad (4.1)$$

361     where  $N_{sim}$  is the number of simulated events for a specific process.

362     The simulated sample are also corrected by the data pile-up distribution, since the pileup dis-  
 363     tribution of MC is different from the pileup distribution of data. The way to correct the MC is to  
 364     assign a weight to each bin of the MC pileup distribution, with respect to the data. The rescaling is  
 365     defined as the ratio between normalized Pile-up (PU) distribution for Data and MC.

$$w_{PU}(n) = \frac{P_{PU}^{Data}(n)}{P_{PU}^{Sim}(n)}, \quad (4.2)$$

366     where  $n$  is the number of interaction per bunch crossing (pile-up).

## 367     4.2 Contribution of the $\Upsilon(nS)$ polarisation

368     Measurements of quarkonium polarization observables may yield information about quarkonium  
 369     production mechanisms that are not available from the study of unpolarized cross sections alone.  
 370     The three polarization states of a  $J = 1$  quarkonium can be specified in terms of a particular  
 371     coordinate system in the rest frame of the quarkonium. This coordinate system is often called the  
 372     "spin-quantization frame".

In a hadron collider,  $\Upsilon(1S, 2S, 3S)$  are reconstructed through their electromagnetic decays into a lepton pair. The information about the polarization of the quarkonium state is encoded in the angular distribution of the leptons. This angular distribution is usually described in the quarkonium rest frame with respect to a particular spin-quantization frame [48]. The polarization of the  $\Upsilon(1S, 2S, 3S)$  is not simulated for signal MC sample and we only apply a reweighting scale factor to each event and so we can emulate the polarization effects [49]. Figure 4.1 present the distributions of  $\cos \Theta$  of  $\Upsilon \rightarrow \mu\mu$ , where  $\Theta$  is the angle between the positive muon and the  $\Upsilon$  in the Z (Higgs) rest-frame. At Table 4.2 we show the the analytical functions used to describe the extremes scenarios (Unpolarized, Transverse Polarization and Longitudinal Polarization) reweighting, presented in this analysis.

It is worth stating that, for the Higgs decay, on the Transverse Polarization is considered. For the Z decay, because of its spin nature, the Unpolarized scenario is used as the nominal one, and the effects of the two other extremes (Transverse Polarization and Longitudinal Polarization) are quoted as systematics.

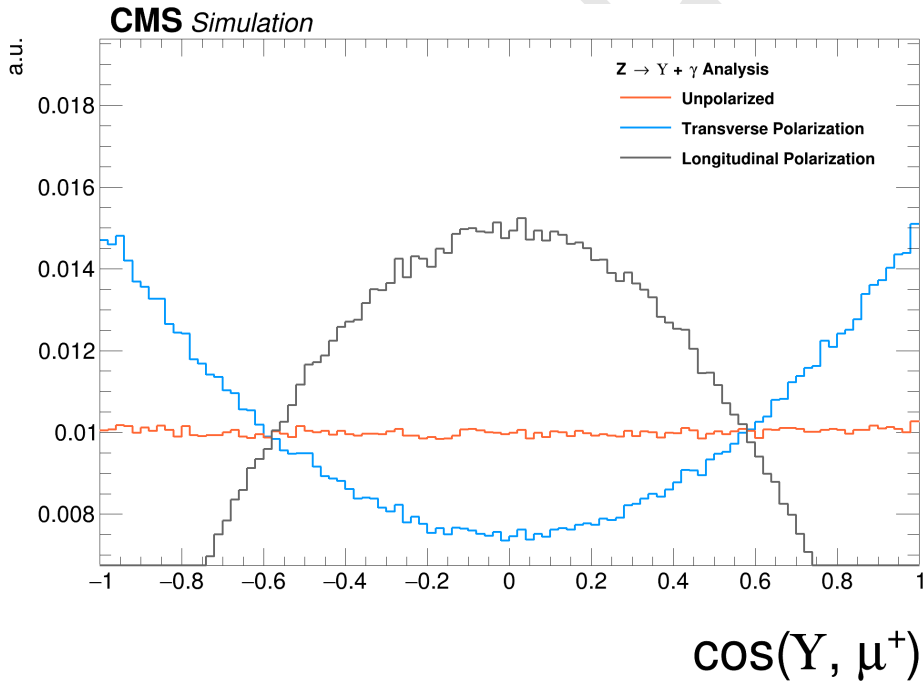


Figure 4.1: Distributions of  $\cos \theta$  of  $\Upsilon \rightarrow \mu\mu$  and  $\gamma^* \rightarrow \mu\mu$ . The orange distribution is the  $Z \rightarrow \Upsilon(1S, 2S, 3S) + \gamma$  sample before reweighting (Unpolarized); the blue and gray distributions are  $Z \rightarrow \Upsilon(1S, 2S, 3S)$  sample after reweighting, for the Transverse and Longitudinal Polarization.

$J_Z$	Polarisation Scenario	Analytic Description
$\pm 1$	Transverse	$3/4 \times (1 + (\cos \Theta)^2)$
0	Longitudinal	$3/2 \times (1 - (\cos \Theta)^2)$

Table 4.2: Summary of the impact of reweighted of polarization contribution using several scenarios.

### 387 4.3 Kinematical studies using MC generator

388 Using the PYTHIA 8.226 generator, the Monte Carlo signals are produced for Higgs (Z) boson  
 389 events decaying in  $\Upsilon(1S,2S,3S) + \gamma$ , which are highly boosted. Observing the kinematic generator  
 390 level distributions in Figure 4.2 for Z boson and Figure 4.3 for Higgs boson, we could conclude that  
 391 the high- $E_T$  (transverse energy, with respect to the beam line) photon will be back-to-back to the  $\Upsilon$   
 392 particles being possible to apply an isolation selection to identify a photon in this kinematic topology.  
 393 Also, we can observe those transverse momenta of the leading/trailing  $p_T$  (transverse momentum,  
 394 with respect to the beam line) muon <sup>3</sup> and the photon and distances  $\Delta R = \sqrt{\Delta\eta^2 + \Delta\phi^2}$  between  
 395 the two muons and between the muons and the photon are a good variable that can be used to  
 396 discriminate the contribution between signal and background events. The leading muon transverse  
 397 momentum can be greater than 45(30) GeV and trailing muon is greater than 10(20) GeV in Higgs(Z)  
 398 decay.  $\Delta R$  distributions of the two muons and between the muons and the photon in the both cases  
 399 show that the two muons are very close and the photon is back-to-back in relation of dimuon system.  
 400 Another feature of this kinematic topology is that the production vertex between muons produced  
 401 in  $\Upsilon$  decaying events and the high- $E_T$  photon is very well defined.

---

<sup>3</sup>In this study we define leading muon and the muon, decaying from the  $\Upsilon$ , with highest  $p_T$ . Trailing muon is the one with the second hight  $p_T$ .

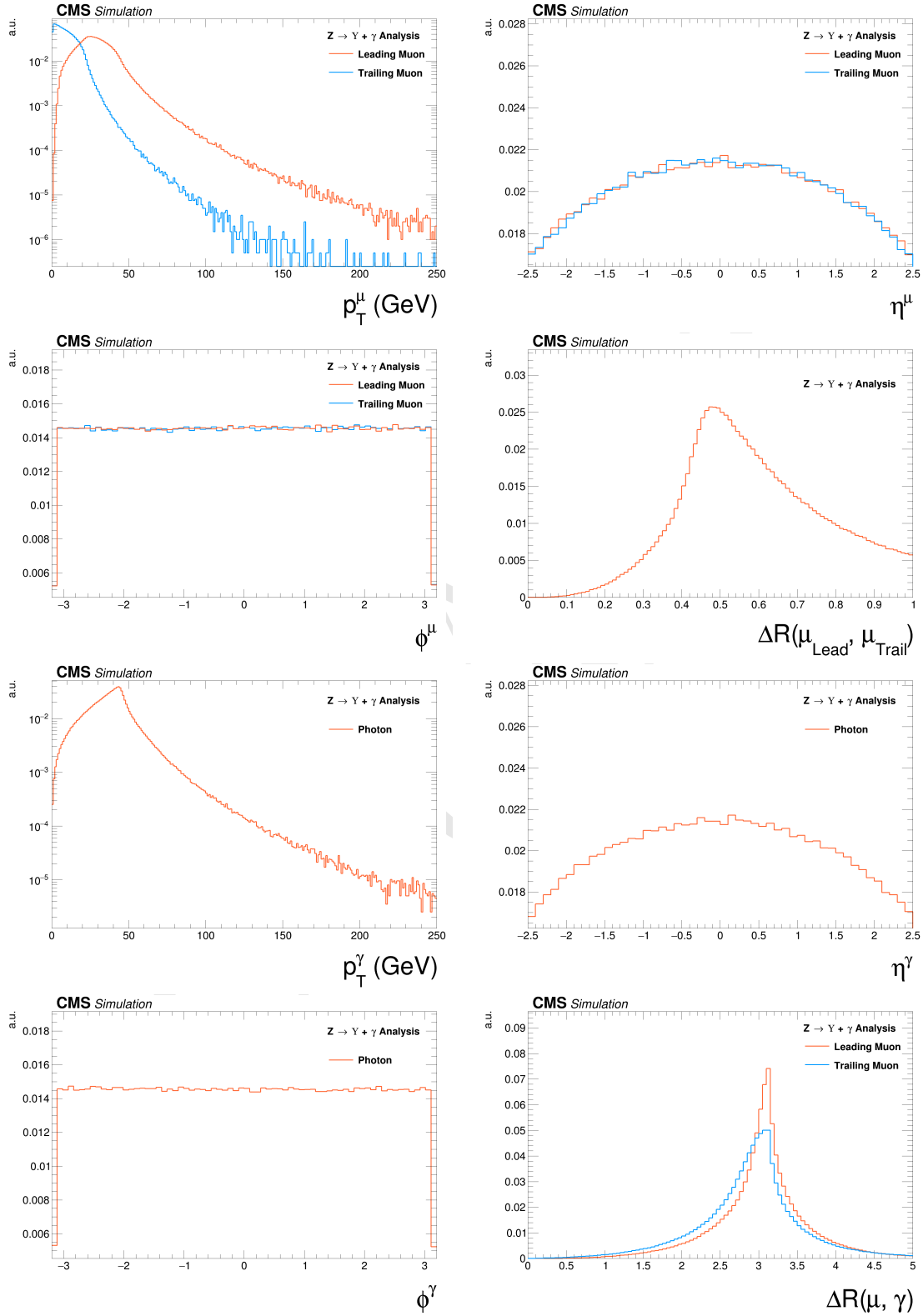


Figure 4.2: Generator level distributions of main variables for  $Z \rightarrow \Upsilon(1S, 2S, 3S) + \gamma$ : Transverse momenta of the leading/trailing  $p_T$  muon and the photon, pseudorapidity ( $\eta$ ) and  $\phi$  of the muons and the photon, distances  $\Delta R$  between the two muons and between the muons and the photon. All the distributions shown in the figure are normalized to the unity of area.

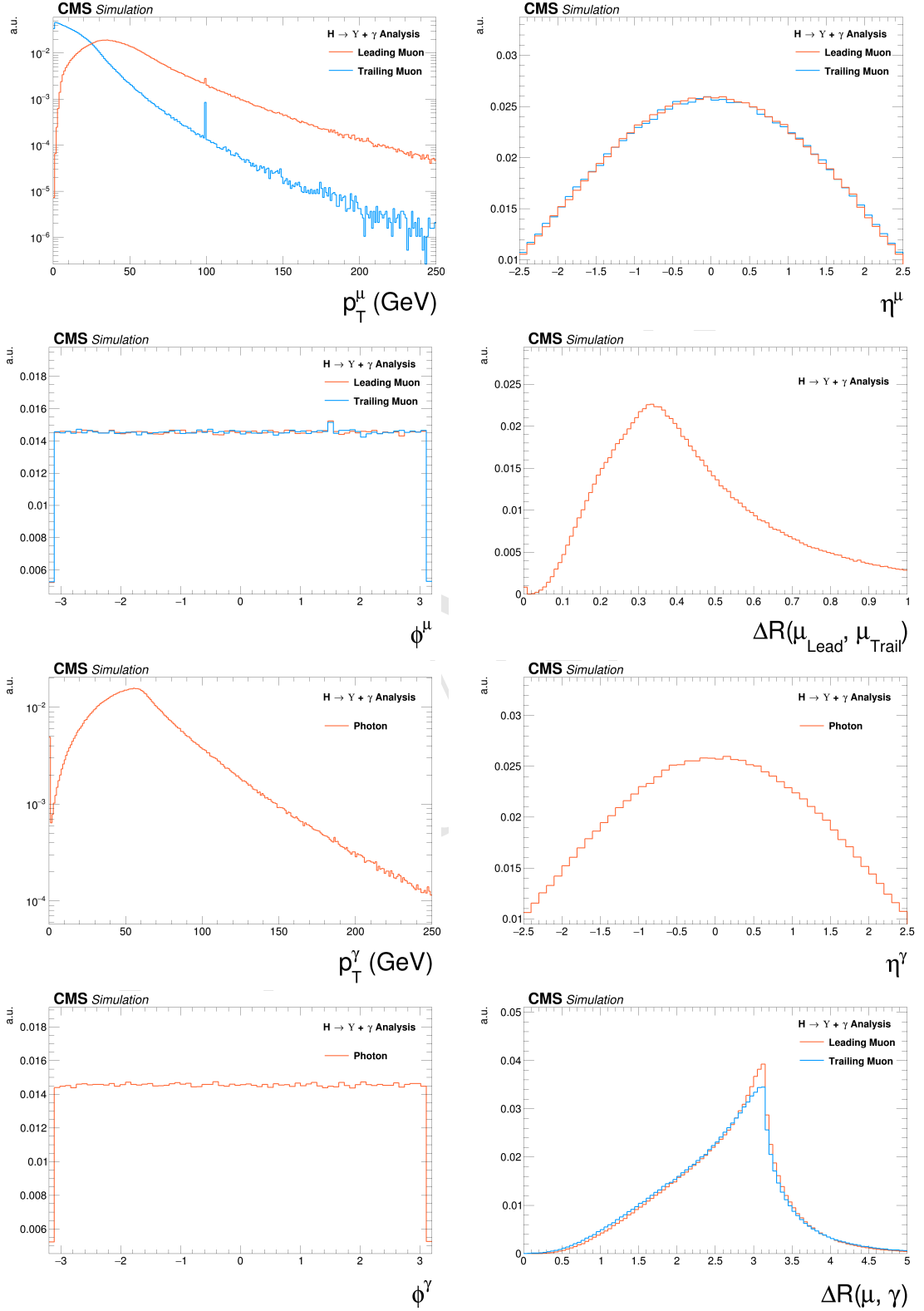


Figure 4.3: Generator level distributions of main variables for  $H \rightarrow \Upsilon(1S, 2S, 3S) + \gamma$  : Transverse momenta of the leading/trailing  $p_T$  muon and the photon, pseudorapidity ( $\eta$ ) and  $\phi$  of the muons and the photon, distances  $\Delta R$  between the two muons and between the muons and the photon. All the distributions shown in the figure are normalized to the unity of area.

## 402 4.4 Event selection

403 The event selection is divided in two steps. At first, a set of cuts related to trigger and physics  
 404 object (muons and photons) selection is applied. High level physics objects at CMS are reconstructed  
 405 based of the Particle Flow (PF) algorithm [50]. This selection is called, within this analysis, Group  
 406 I.

407 For the events that pass the Group I selection, another set of cuts is applied, this time focusing  
 408 on kinematical (phase space) event selection, in order to enhance the signal to background ratio.  
 409 This later set is called, within this analysis, Group II. After full selection, three exclusive categories  
 410 are defined, based on the photon's  $\eta$  region and its energy spread shape within the ECAL cells (R9).

411 After the full selection, a background and signal modeling process is applied, based on the  
 412 invariant mass distributions, which will be explained in the next section.

## 413 4.5 Trigger and physics object selection (Group I)

### 414 4.5.1 Trigger

415 In this study, the same trigger requirements are applied to both data and simulated samples.  
 416 For the first trigger level (L1), events are selected if they present at least one muon with transverse  
 417 momentum greater than 5 GeV and an isolated <sup>4</sup> photon or electron with transverse momentum  
 418 greater than 18 GeV (at L1, there is no differentiation between photons and electrons). At the  
 419 software level of the trigger system (HLT), the events are required to have at least one muon with  
 420 transverse momentum greater than 17 GeV and a photon with transverse momentum greater than  
 421 30 GeV.

422 In order to compensate any difference in the trigger performance between simulated and data  
 423 samples, for every selected MC a proper scale factor is applied, based on the the  $p_T$  of the recon-  
 424 structed muon and photon. Considering the similarity of this analysis with the  $H/Z \rightarrow J/\psi + \gamma$   
 425 analysis [23], not only in therm of data samples, but also for triggering and physics object selection,  
 426 the same scale factors were applied.

### 427 4.5.2 Muon Identification

428 Ahead of any selection, a standard CMS "Ghost Cleaning" procedure is applied to all recon-  
 429 structed muons in order to avoid that a single physical muon is reconstructed as two or more. For  
 430 this procedure, reconstructed muons sharing 50% or more segments in the system are arbitrated.

431 After the cleaning, a muon is chosen when it passes a a two step identification: the **Loose ID**  
 432 and the **Tight ID**. Below the muon identification procedure is summarized .

433 For the Loose ID, each muon is required to:

- 434 • have transverse momentum greater than 5 GeV, in order to cope with Particle Flow require-  
 435 ments;

---

<sup>4</sup>The concept of isolation will be detailed later, but in summary, it means a object which has very small activity (above a certain threshold of energy/momentun) around it. In hadron-hadron collider, isolation is a characteristics of hard interactions.

- 436 • be within the muon system acceptance:  $|\eta| < 2.4$ ;
- 437 • to have a three dimensional impact parameter uncertainty smaller than 4;
- 438 • to have transverse distance smaller than 0.5 cm ( $d_{xy} < 0.5$ ), with respect to the primary
- 439 vertex (PV);
- 440 • to have longitudinal distance greater than 1.0 cm ( $d_z < 1$ ), with respect to the primary vertex
- 441 (PV).

442 Muons reconstructed only in the muon system, without a correspondence with the tracker, are  
 443 rejected. The last three requirements of the Loose ID are imposed in order to suppress muons from  
 444 in-flight decays.

445 The primary vertex itself, is determined as the reconstructed vertex with the biggest sum of  $p_T^2$   
 446 in the event. This sum is performed, considering all the charged PF candidates clustered by the jet  
 447 finding algorithms [51, 52] and the MET, which is defined as the  $p_T$  vector sum of all the charged  
 448 and neutral PF candidates associated to that vertex.

449 For the Tight ID, muons with transverse momentum  $p_T < 200$  GeV, are required to have  
 450 been reconstructed with the Particle Flow (PF) algorithm. If they have  $p_T > 200$  GeV, they  
 451 should be reconstructed with the Particle Flow (PF) algorithm or satisfy the strict tracker requirements  
 452 (defined in table 4.3).

Requirement	Technical definition
Muon station matching	Muon is matched to segments in at least two stations in the muon system
Good $p_T$ measurement	$\frac{p_T}{\sigma_{p_T}} < 0.3$
Vertex compatibility ( $x - y$ )	$d_{xy} < 2$ mm
Vertex compatibility ( $z$ )	$d_z < 5$ mm
Pixel hits	At least one pixel hit
Tracker hits	Hits in at least six tracker layers

Table 4.3: Conditions for a muon to pass the strict tracker requirements.

453 To mitigate spurious signal in the detector that would mimic a muon, the leading muon (the  
 454 one with highest  $p_T$ ) is required to be isolated within a cone of radius  $\Delta R = \sqrt{\Delta\eta^2 + \Delta\phi^2} < 0.3$   
 455 in the  $\eta - \phi$  plane. The isolation is evaluated in terms of  $\mathcal{I}^\mu < 0.35$ , defined as:

$$\mathcal{I}^\mu \equiv \left( \sum p_T^{\text{charged}} + \max \left[ 0, \sum p_T^{\text{neutral}} + \sum p_T^\gamma - p_T^{\text{PU}}(\mu) \right] \right) / p_T^\mu. \quad (4.3)$$

456 The  $\sum p_T^{\text{charged}}$  is the scalar sum of the transverse momenta of charged hadrons originating from  
 457 the chosen primary vertex of the event. The  $\sum p_T^{\text{neutral}}$  and  $\sum p_T^\gamma$  are the scalar sums of the transverse  
 458 momenta for neutral hadrons and photons, respectively. Since the isolation variable is particularly  
 459 sensitive to energy deposits from pileup interactions, a  $p_T^{\text{PU}}(\mu)$  contribution is subtracted, where  
 460  $p_T^{\text{PU}}(\mu) \equiv 0.5 \times \sum_i p_T^{\text{PU},i}$ , where  $i$  runs over the momenta of the charged hadron PF candidates  
 461 not originating from the primary vertex, and the factor of 0.5 corrects for the different fraction of  
 462 charged and neutral particles in the cone.

463 One should keep in mind that this muon identification is the same as the one used by the  
 464  $H \rightarrow ZZ^* \rightarrow 4l$  [53]. This was done in order to keep in phase with other Higgs analysis inside  
 465 the collaboration. After the muon identification, an appropriate scale factor is applied to the MC  
 466 events based on the leading muon  $p_T$  and  $\eta$ , in order to correct any possible discrepancy between  
 467 data and simulated samples. The scale factors were taken from the  $H \rightarrow ZZ^* \rightarrow 4l$  analysis.

468 In order to cope with trigger requirements, the leading muon should have  $p_T > 20$  GeV and the  
 469 trailing muon  $p_T > 4$  GeV.

#### 470 4.5.3 Photon Identification

471 For the photon identification and selection, standard CMS . The Multivariate (MVA) Photon  
 472 identification is used with a working point of 90%, together with a electron veto procedure, to  
 473 avoid misidentification of electrons as photons. Kinematically, the photons are requested to have  
 474 transverse energy, with respect to the beam line,  $E_T > 33$  GeV and reconstructed within the CMS  
 475 acceptance for photons  $|\eta_{SC}| < 2.5^5$ , excluding the Electromagnetic Calorimeter (ECAL) Barrel-  
 476 Endcap intersections.

477 The threshold of 33 GeV for the photon transverse energy is driven by the trigger requirements.  
 478 The selecte photon, per event, is the one with highest  $E_T$ .

#### 479 4.5.4 Kinematical distributions

480 The selection described so far, is called Group I. The plots shown below are related to selected  
 481 events after this set.

482 Figures 4.4 to 4.9 presents the  $p_T$ ,  $\eta$  and  $\phi$  distributions for the leading muon, trailing muon  
 483 and the photon, for the Z decaying in  $\Upsilon(1S, 2S, 3S) + \gamma$ .

484 Figures 4.10 to 4.12 presents the  $p_T$ ,  $\eta$  and  $\phi$  distributions for reconstructed  $\Upsilon(nS)$  ( $\mu\mu$  system)  
 485 and the reconstructed boson ( $\mu\mu\gamma$  system).

486 Figures 4.13 to 4.16 presents the  $\Delta R = \sqrt{\Delta\eta^2 + \Delta\phi^2}$  between the photon and the muons, the  
 487  $\Delta R$  distributions between reconstructed dimuon ( $\mu\mu$ ) system and the photon, the absolute value  
 488 of the  $\Delta\phi$  between the leading muon and the photon, the ratio for the transverse momentum of  
 489 the reconstructed Upsilon and the reconstructed Z mass ( $p_T^{\mu\mu}/M_{\mu\mu\gamma}$ ), the ratio for the transverse  
 490 energy of the reconstructed Photon and the reconstructed Z mass ( $E_T^{\mu\mu}/M_{\mu\mu\gamma}$ ) and dimuon mass  
 491 distribution of the reconstructed  $\Upsilon(nS)$ .

492 Figures 4.17 to 4.29 present the same variables, but for the Higgs decaying in  $\Upsilon(1S, 2S, 3S) +$   
 493  $\gamma$  channel.

---

<sup>5</sup>SC stands for Super Cluster of the reconstructed photon. It is the set of cell in the Electromagnetic Calorimeter used for the photon observation.

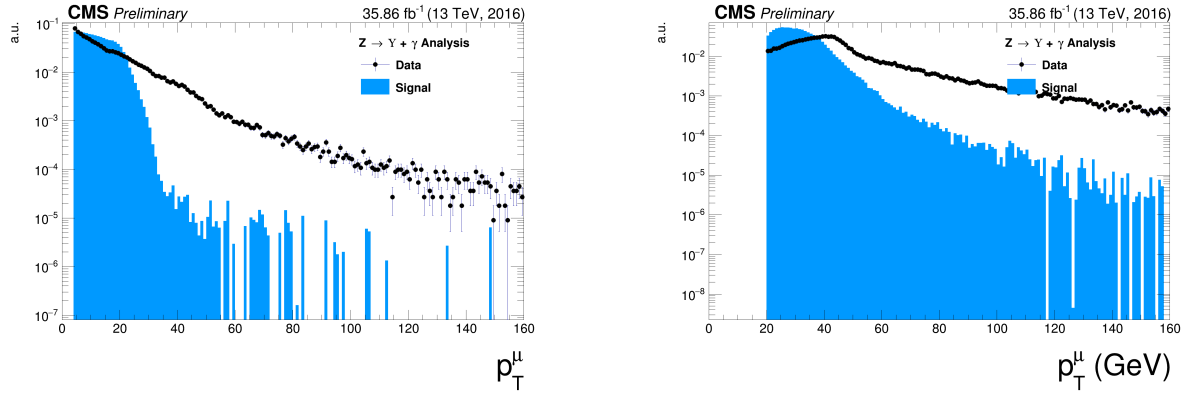


Figure 4.4: The  $p_T$  muon distributions from data and signal events for  $Z$  decaying in  $\Upsilon(1S, 2S, 3S) + \gamma$  after Group I of selection cuts, where on left are presenting the trailing muons and on right are the leading muons. The plots are normalized to the unit of area.

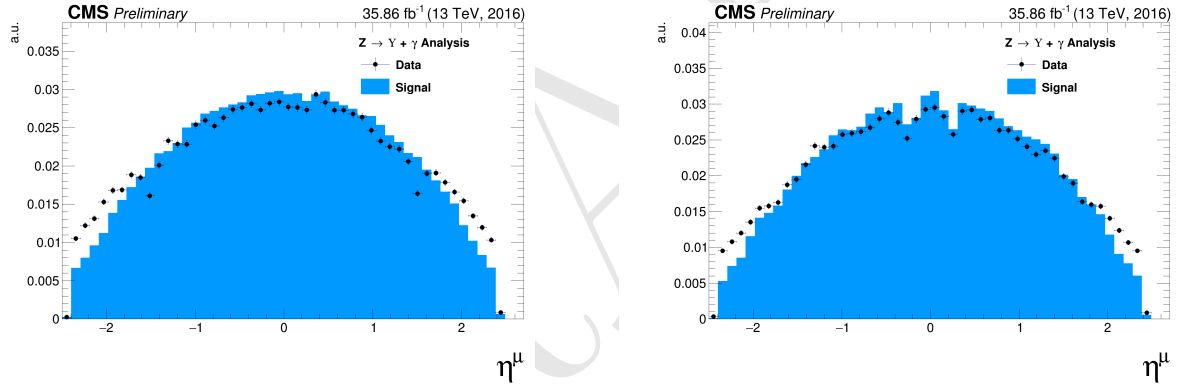


Figure 4.5: The  $\eta$  muon distributions from data and signal events of  $Z$  decaying in  $\Upsilon(1S, 2S, 3S) + \gamma$  after Group I of selection cuts, where on left are presenting the trailing muons and on right are the leading muons. The plots are normalized to the unit of area.

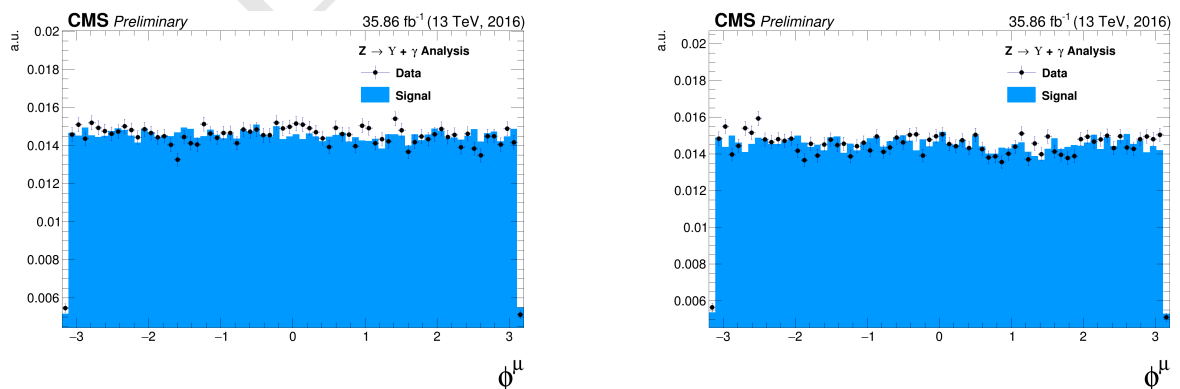


Figure 4.6: The  $\phi$  muon distributions from data and signal events of  $Z$  decaying in  $\Upsilon(1S, 2S, 3S) + \gamma$  after Group I of selection cuts, where on left are presenting the trailing muons and on right are the leading muons. The plots are normalized to the unit of area.

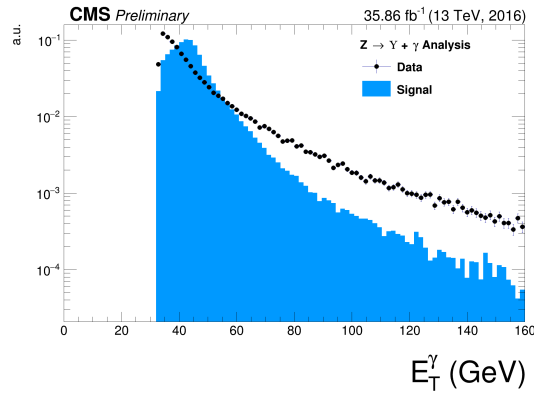


Figure 4.7: The  $p_T$  photon distributions from data and signal events for Z decaying in  $\Upsilon(1S, 2S, 3S) + \gamma$  Group I of selection cuts. The plots normalized to the unit of area.

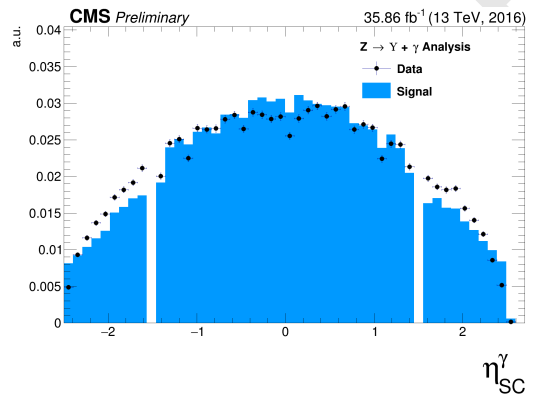


Figure 4.8: The  $\eta$  photon distributions from data and signal events of Z decaying in  $\Upsilon(1S, 2S, 3S) + \gamma$  after Group I of selection cuts. The plot is normalized to the unit of area.

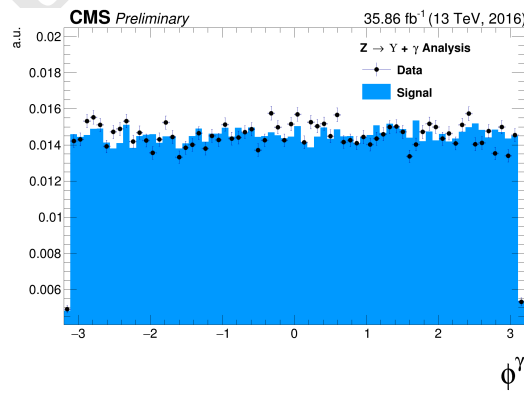


Figure 4.9: The  $\phi$  photon distributions from data and signal events of Z decaying in  $\Upsilon(1S, 2S, 3S) + \gamma$  after Group I of selection cuts. The plot is normalized to the unit of area.

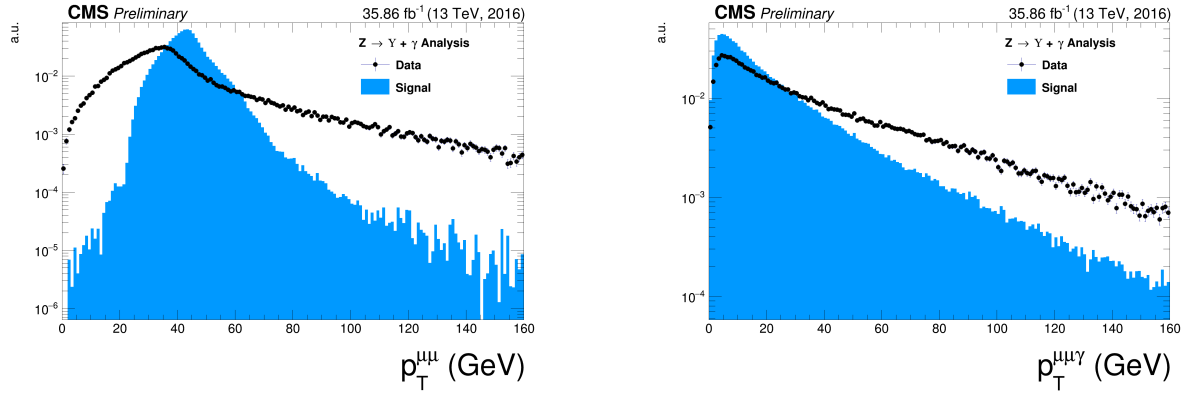


Figure 4.10: The  $p_T$  distributions for the reconstructed  $\Upsilon(1S, 2S, 3S)$  in the left and for  $Z$  in the right from data and signal events for  $Z$  decaying in  $\Upsilon(1S, 2S, 3S) + \gamma$  after Group I of selection cuts. The plots are normalized to the unit of area.

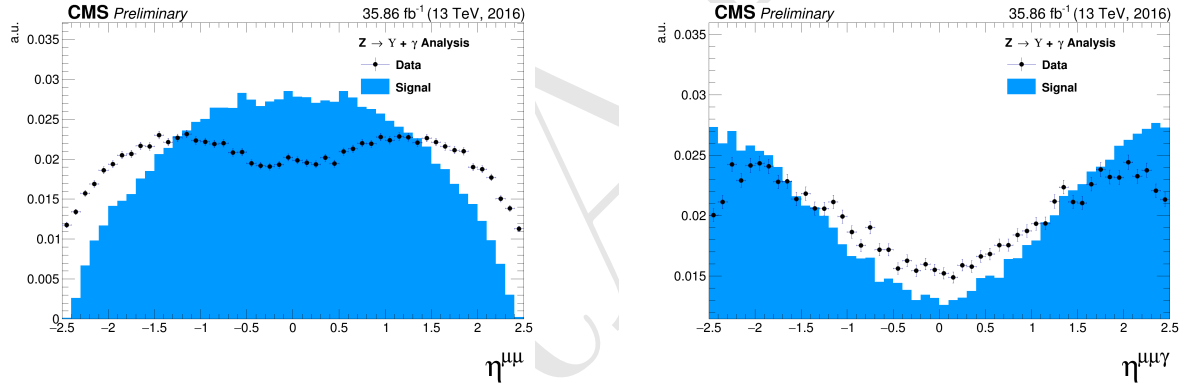


Figure 4.11: The  $\eta$  distributions for  $\Upsilon(1S, 2S, 3S)$  in the left and for  $Z$  in the right from data and signal events for  $Z$  decaying in  $\Upsilon(1S, 2S, 3S) + \gamma$  after Group I of selection cuts. The plots are normalized to the unit of area.

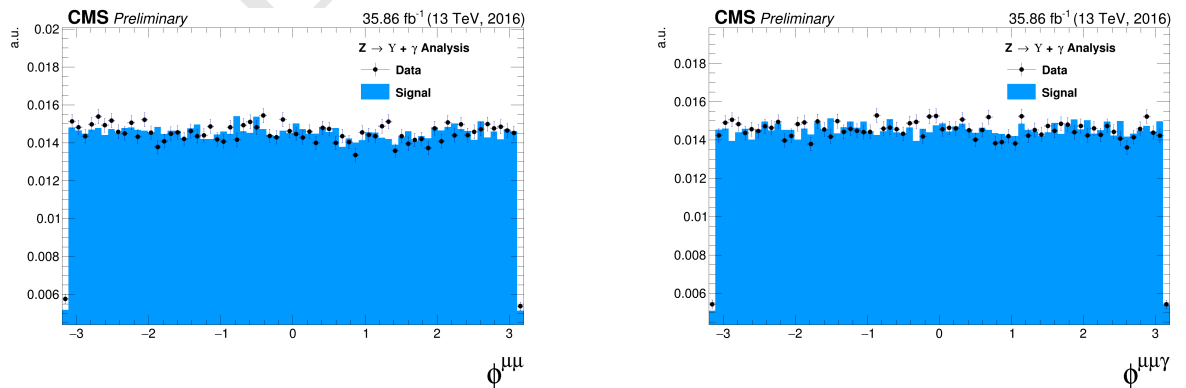


Figure 4.12: The  $\phi$  distributions for  $\Upsilon(1S, 2S, 3S)$  in the left and for  $Z$  in the right from data and signal events for  $Z$  decaying in  $\Upsilon(1S, 2S, 3S) + \gamma$  after Group I of selection cuts. The plots are normalized to the unit of area.

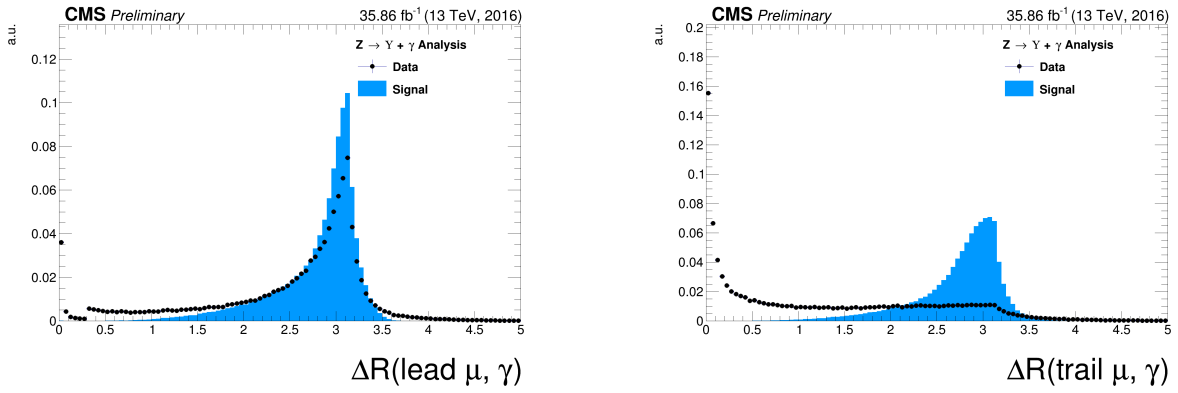


Figure 4.13: The  $\Delta R$  distributions between the photon and the leading muon (left) and the trailing muon (right) for for Z decaying in  $\Upsilon(1S, 2S, 3S) + \gamma$  from data and signal events after Group I of selection cuts. The plots are normalized to the unit of area.

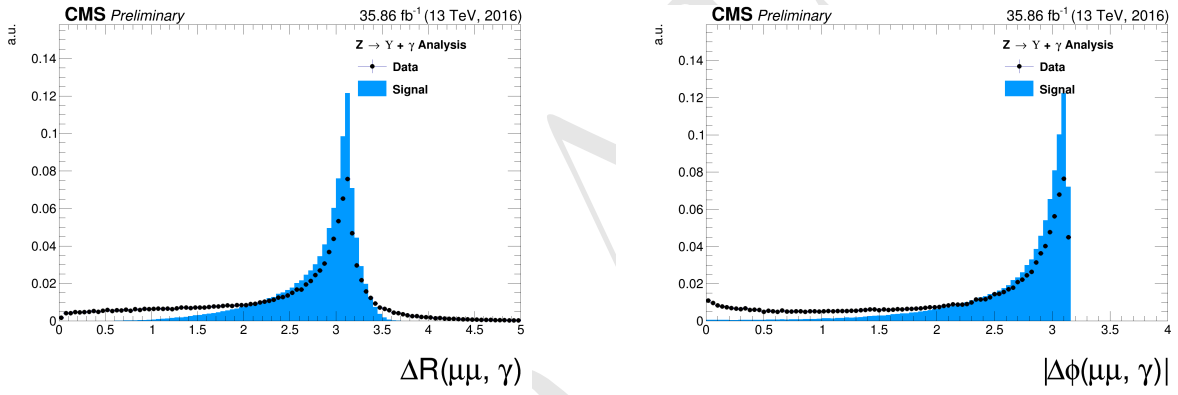


Figure 4.14: Left: The  $\Delta R$  distributions between reconstructed dimuon ( $\mu\mu$ ) system and the photon. Right: absolute value of the  $\Delta\phi$  between the leading muon and the photon for for Z decaying in  $\Upsilon(1S, 2S, 3S) + \gamma$  from data and signal events after Group I of selection cuts. The plots are normalized to the unit of area.

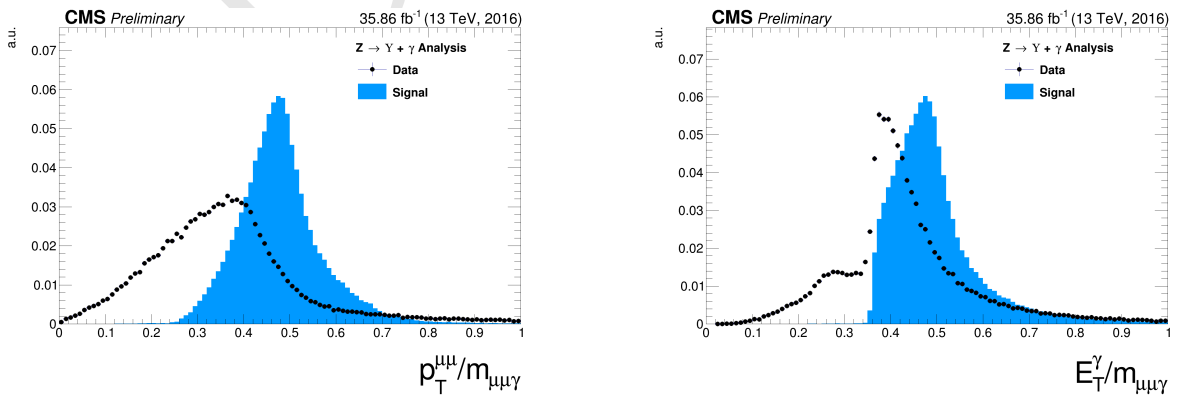


Figure 4.15: The ratio for the transverse momentum of the reconstructed Upsilon and the reconstructed Z mass ( $p_T^{\mu\mu}/m_{\mu\mu\gamma}$  - left) and the ratio for the transverse energy of the reconstructed Photon and the reconstructed Z mass ( $E_T^\gamma/m_{\mu\mu\gamma}$  - right) distribution for Z decaying in  $\Upsilon(1S, 2S, 3S) + \gamma$  from data and signal events after Group I of selection cuts. The plots are normalized to the unit of area.

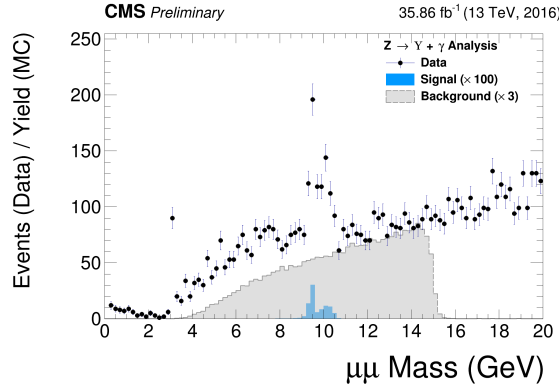


Figure 4.16: The dimuon mass distribution of the reconstructed  $\Upsilon(1S, 2S, 3S)$  from data and signal events for  $Z$  decaying after Group I of selection cuts. The plot is normalized to the number of events. "Signal" stands for the  $Z \rightarrow \Upsilon(1S, 2S, 3S) + \gamma$  sample (scaled by a factor of  $\times 100$ ) and "Background" corresponds to the peaking background ( $Z \rightarrow \mu\mu\gamma_{FSR}$ ) sample (scaled by a factor of  $\times 3$ ).

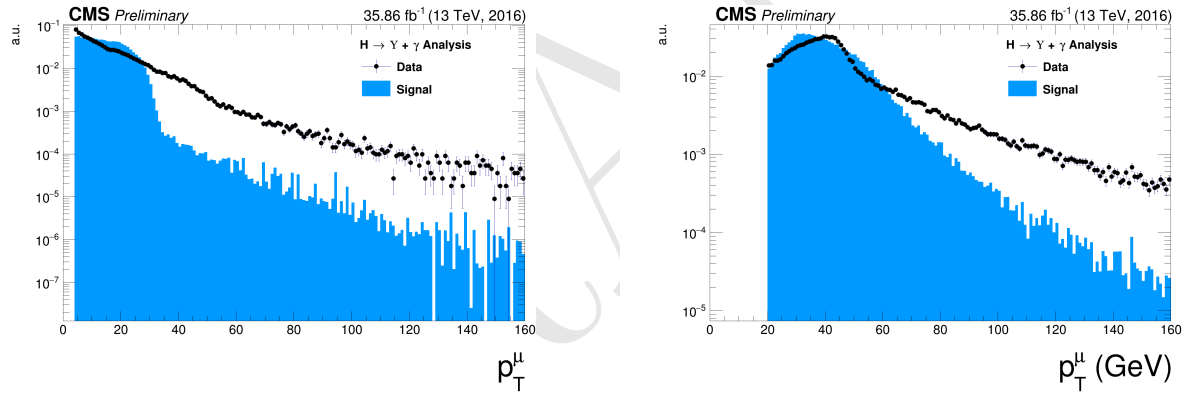


Figure 4.17: The  $p_T$  muon distributions from data and signal events for Higgs decaying in  $\Upsilon(1S, 2S, 3S) + \gamma$  after Group I of selection cuts, where on left are presenting the trailing muons and on right are the leading muons. The plots are normalized to the unit of area.

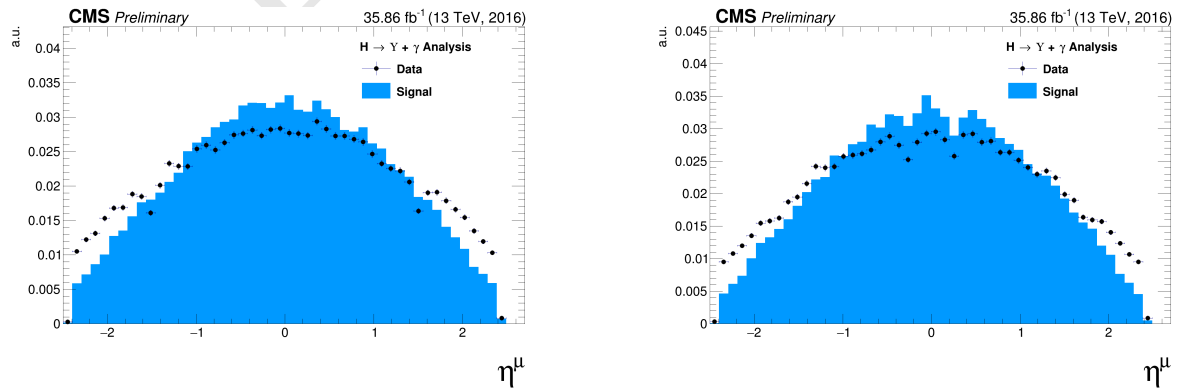


Figure 4.18: The  $\eta$  muon distributions from data and signal events of Higgs decaying in  $\Upsilon(1S, 2S, 3S) + \gamma$  after Group I of selection cuts, where on left are presenting the trailing muons and on right are the leading muons. The plots are normalized to the unit of area.

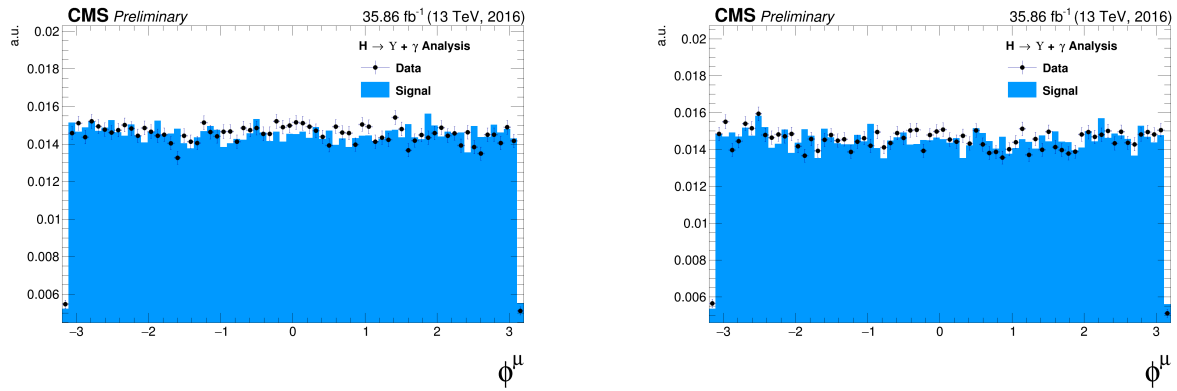


Figure 4.19: The  $\phi$  muon distributions from data and signal events of Higgs decaying in  $\Upsilon(1S, 2S, 3S) + \gamma$  after Group I of selection cuts, where on left are presenting the trailing muons and on right are the leading muons. The plots are normalized to the unit of area.

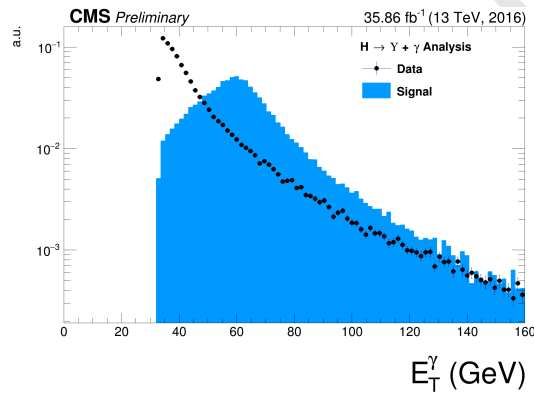


Figure 4.20: The  $p_T$  photon distributions from data and signal events for Higgs decaying in  $\Upsilon(1S, 2S, 3S) + \gamma$  Group I of selection cuts. The plot is normalized to the unit of area.

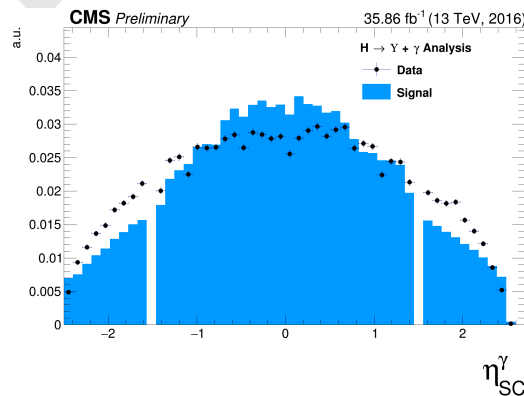


Figure 4.21: The  $\eta$  photon distributions from data and signal events of Higgs decaying in  $\Upsilon(1S, 2S, 3S) + \gamma$  after Group I of selection cuts. The plot is normalized to the unit of area.

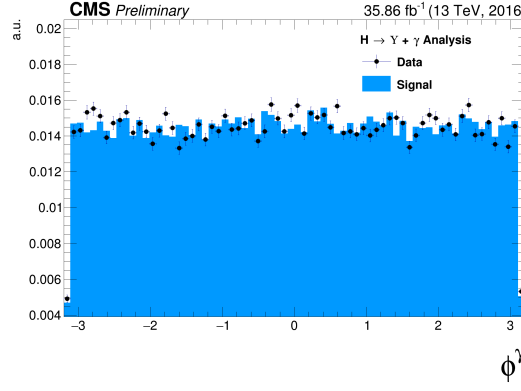


Figure 4.22: The  $\phi$  photon distributions from data and signal events of Higgs decaying in  $\Upsilon(1S, 2S, 3S) + \gamma$  after Group I of selection cuts. The plot is normalized to the unit of area.

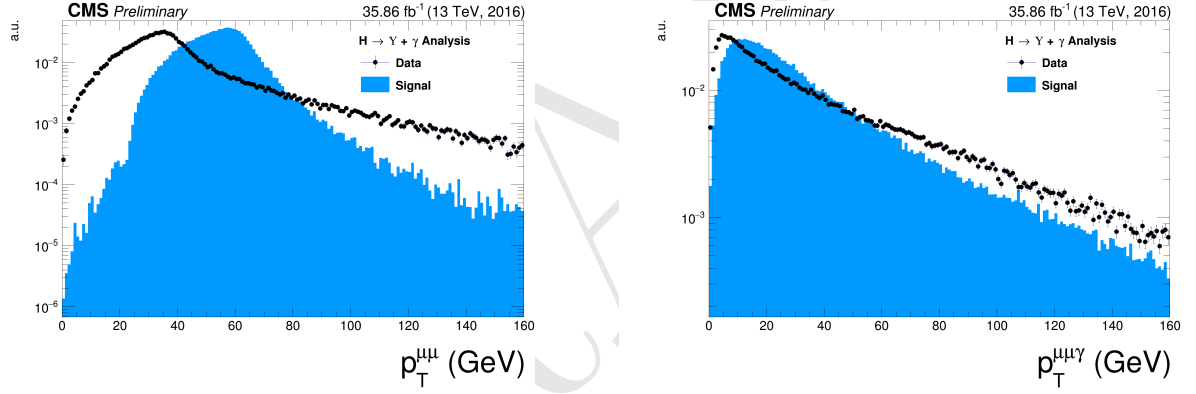


Figure 4.23: The  $p_T$  distributions for  $\Upsilon(1S, 2S, 3S)$  in the left and for Higgs in the right from data and signal events for Higgs decaying in  $\Upsilon(1S, 2S, 3S) + \gamma$  after Group I of selection cuts. The plots are normalized to the unit of area.

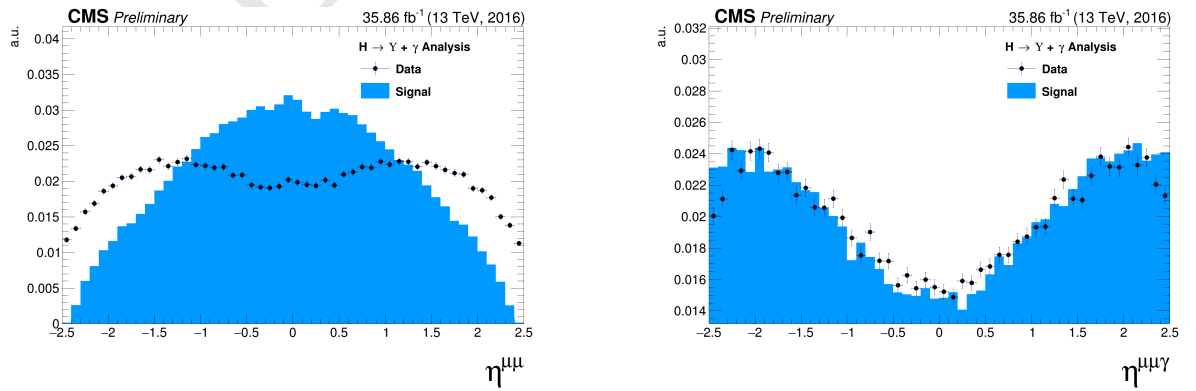


Figure 4.24: The  $\eta$  distributions for  $\Upsilon(1S, 2S, 3S)$  in the left and for Higgs in the right from data and signal events for Higgs decaying in  $\Upsilon(1S, 2S, 3S) + \gamma$  after Group I of selection cuts. The plots are normalized to the unit of area.

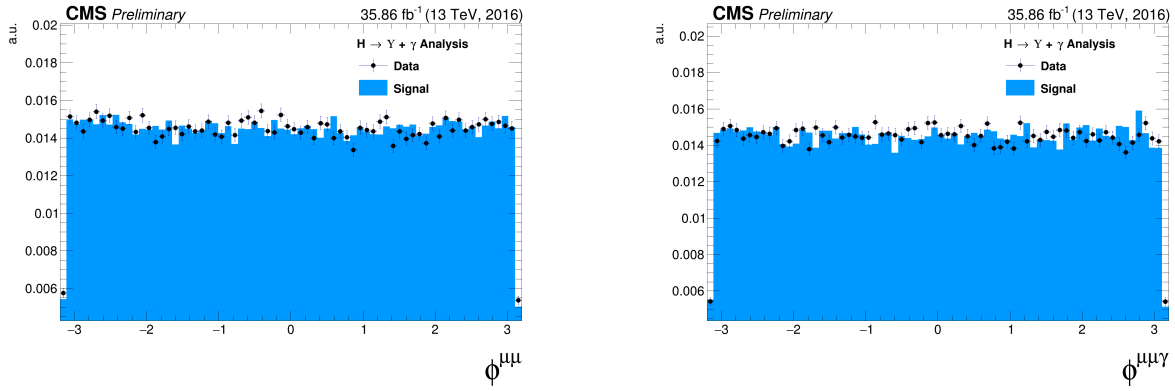


Figure 4.25: The  $\phi$  distributions for  $\Upsilon(1S, 2S, 3S)$  in the left and for Higgs in the right from data and signal events for Higgs decaying in  $\Upsilon(1S, 2S, 3S) + \gamma$  after Group I of selection cuts. The plots are normalized to the unit of area.

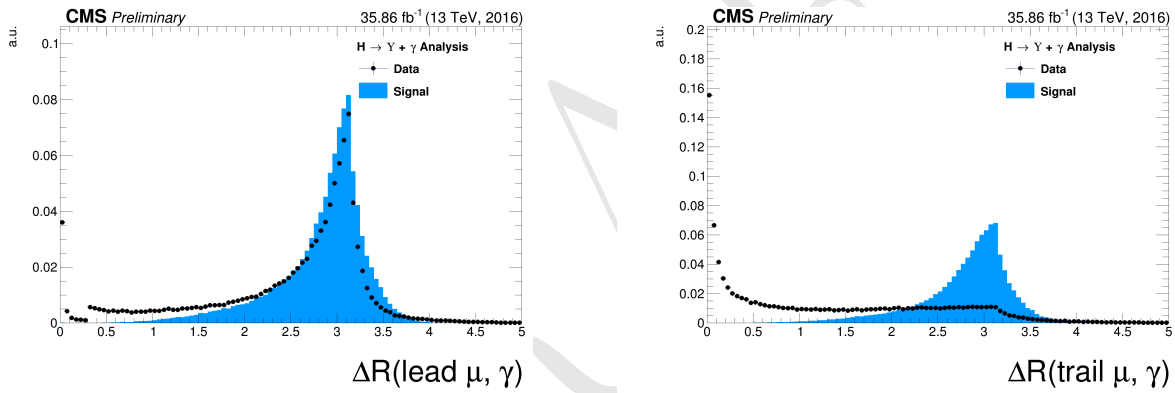


Figure 4.26: The  $\Delta R$  distributions between the photon and the leading muon (left) and the trailing muon (right) for Higgs decaying in  $\Upsilon(1S, 2S, 3S) + \gamma$  from data and signal events after Group I of selection cuts. The plots are normalized to the unit of area.

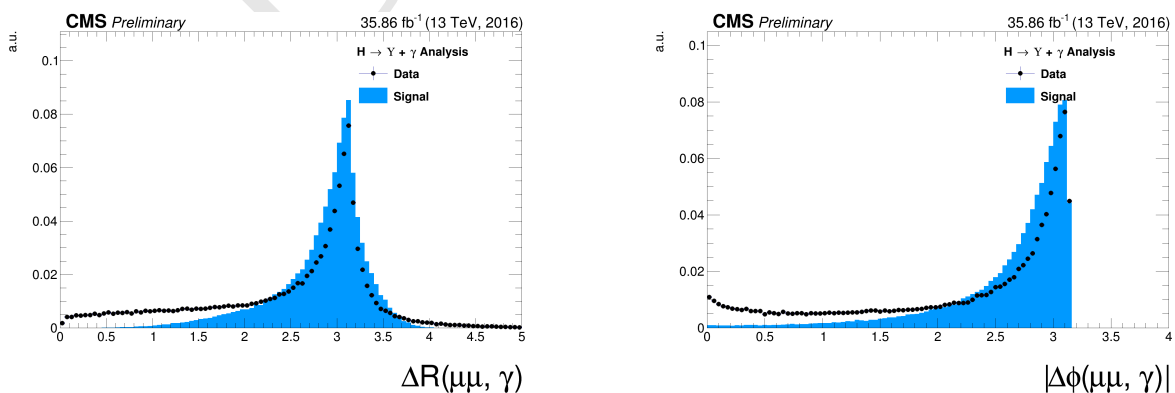


Figure 4.27: Left: The  $\Delta R$  distributions between reconstructed dimuon ( $\mu\mu$ ) system and the photon. Right: absolute value of the  $\Delta\phi$  between the leading muon and the photon for Higgs decaying in  $\Upsilon(1S, 2S, 3S) + \gamma$  from data and signal events after Group I of selection cuts. The plots are normalized to the unit of area.

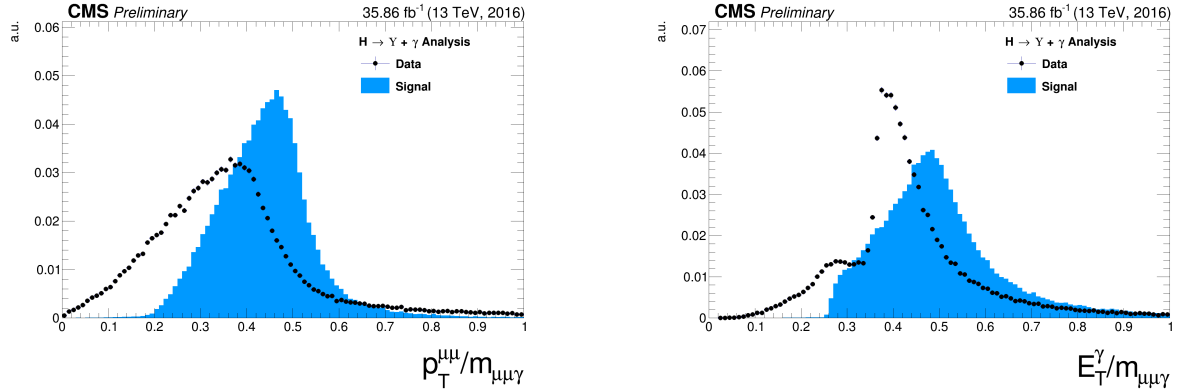


Figure 4.28: The ratio for the transverse momentum of the reconstructed Upsilon and the reconstructed Higgs mass ( $p_T^{\mu\mu}/M_{\mu\mu\gamma}$  - left) and the ratio for the transverse energy of the reconstructed Photon and the reconstructed Higgs mass ( $E_T^\gamma/M_{\mu\mu\gamma}$  - right) distribution for Higgs decaying in  $\Upsilon(1S, 2S, 3S) + \gamma$  from data and signal events after Group I of selection cuts. The plots are normalized to the unit of area.

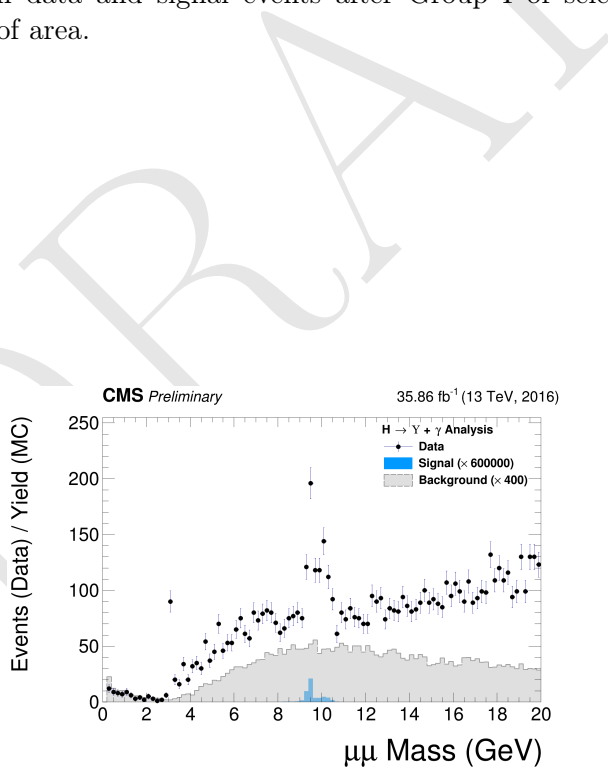


Figure 4.29: The dimuon mass distribution of the reconstructed  $\Upsilon(1S, 2S, 3S)$  from data and signal events for Higgs decaying after Group I of selection cuts. This plot is normalized the expected number of events. The plot is normalized to the number of events. "Signal" stands for the  $H \rightarrow \Upsilon(1S, 2S, 3S) + \gamma$  sample (scaled by a factor of  $\times 60000$ ) and "Background" corresponds to the peaking background (Higgs Dalitz Decay) sample (scaled by a factor of  $\times 400$ ).

## 4.6 Kinematical selection (Group II)

After all Trigger and Object Identification cuts, described in before (**Group I**), a set of kinematical cuts are applied in order to improve the signal to background relation. They are

- $\Delta R(\text{leading } \mu, \gamma) > 1;$
- $\Delta R(\text{trailing } \mu, \gamma) > 1;$
- $\Delta R(\mu\mu, \gamma) > 2;$
- $|\Delta\phi(\text{leading } \mu, \gamma)| > 1.5;$
- $8.4 \text{ GeV} < M_{\mu\mu} < 11.1 \text{ GeV};$
- $E_T^\gamma/M_{\mu\mu\gamma} > 35/91.2 \text{ for the Z decay or } 35/125 \text{ for the Higgs decay};$
- $p_T^{\mu\mu}/M_{\mu\mu\gamma} > 35/91.2 \text{ for the Z decay or } 35/125 \text{ for the Higgs decay.}$

The choice of these thresholds were based on the visual inspection of the distributions (besides the invariant mass distribution of the dimuon system  $M_{\mu\mu}$ , which needs to be defined around the  $v(1S, 2S, 3S)$  mass) and to keep this analysis in phase with other similar analysis within CMS.

Below it is shown the same set of plot shown before, but this time, taking into account the full selection (**Group I+II**).

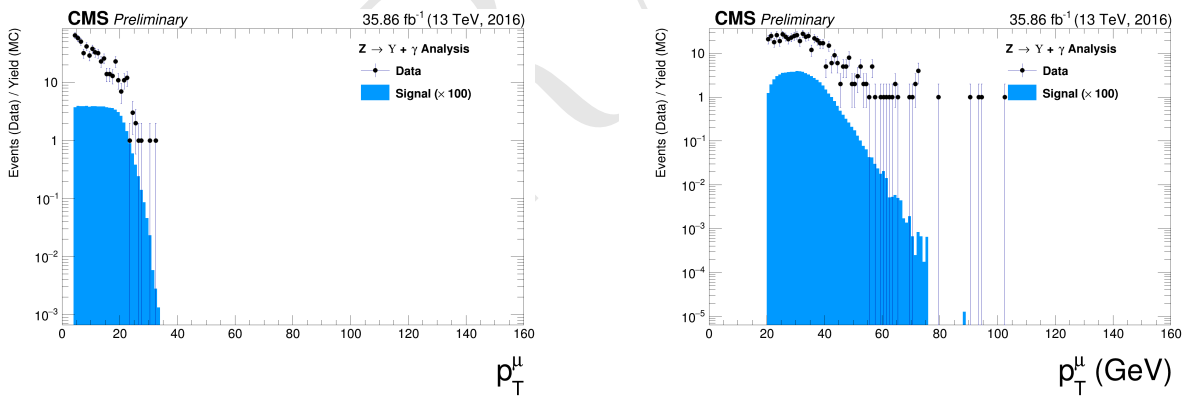


Figure 4.30: The  $p_T$  muon distributions from data and signal events for Z decaying in  $\Upsilon(1S, 2S, 3S) + \gamma$  after Group I of selection cuts, where on left are presenting the trailing muons and on right are the leading muons. The plots are normalized to the number of events. Signal sample is scaled by a factor of  $\times 100$ .

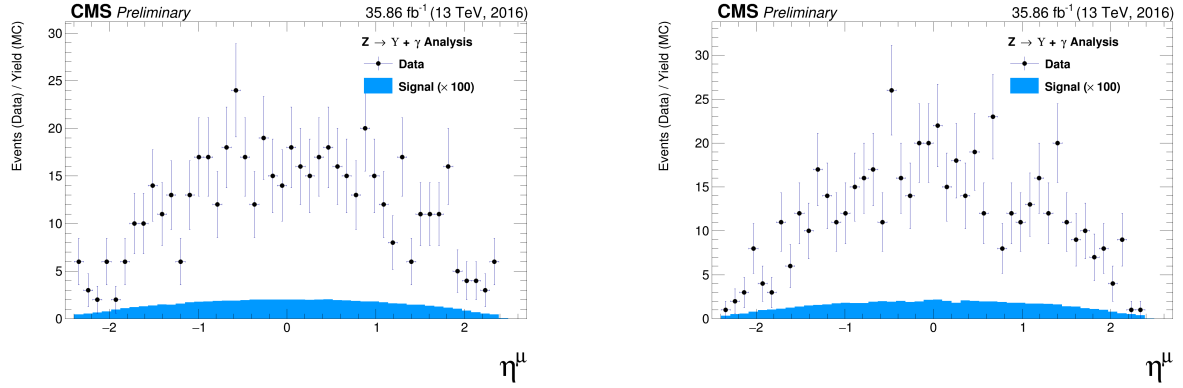


Figure 4.31: The  $\eta$  muon distributions from data and signal events of  $Z$  decaying in  $\Upsilon(1S, 2S, 3S) + \gamma$  after Group I of selection cuts, where on left are presenting the trailing muons and on right are the leading muons. The plots are normalized to the number of events. Signal sample is scaled by a factor of  $\times 100$ .

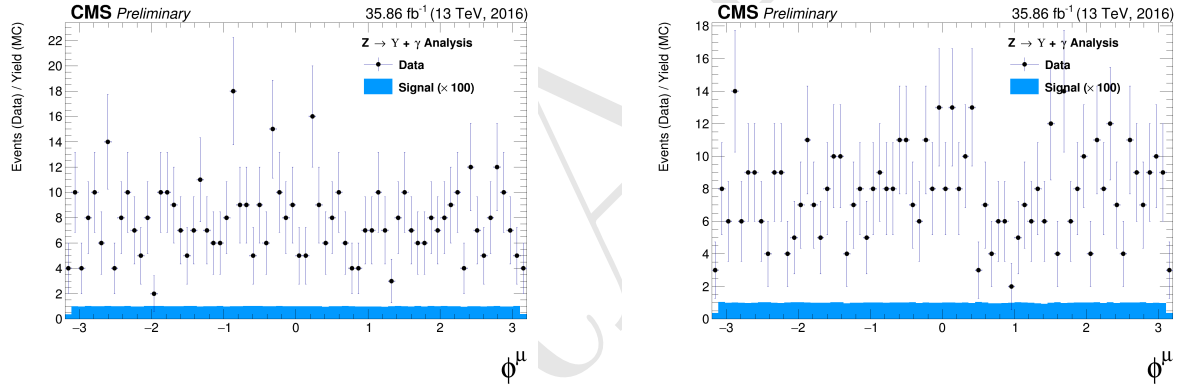


Figure 4.32: The  $\phi$  muon distributions from data and signal events of  $Z$  decaying in  $\Upsilon(1S, 2S, 3S) + \gamma$  after Group I of selection cuts, where on left are presenting the trailing muons and on right are the leading muons. The plots are normalized to the number of events. Signal sample is scaled by a factor of  $\times 100$ .

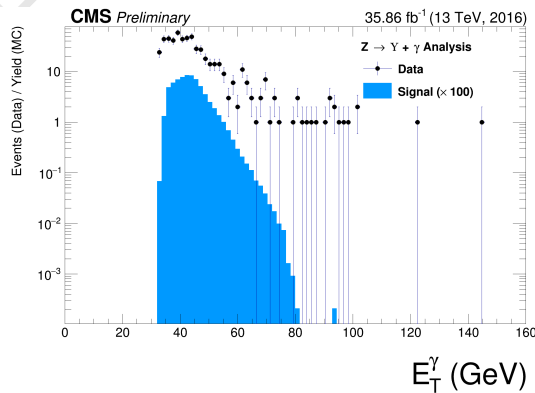


Figure 4.33: The  $p_T$  photon distributions from data and signal events for  $Z$  decaying in  $\Upsilon(1S, 2S, 3S) + \gamma$  all (Group I+II) selection cuts. The plot is normalized to the number of events. Signal sample is scaled by a factor of  $\times 100$ .

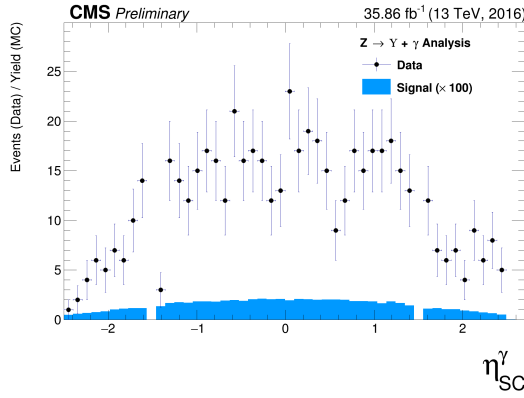


Figure 4.34: The  $\eta$  photon distributions from data and signal events of  $Z$  decaying in  $\Upsilon(1S, 2S, 3S) + \gamma$  after all (Group I+II) selection cuts. The plot is normalized to the number of events. Signal sample is scaled by a factor of  $\times 100$ .

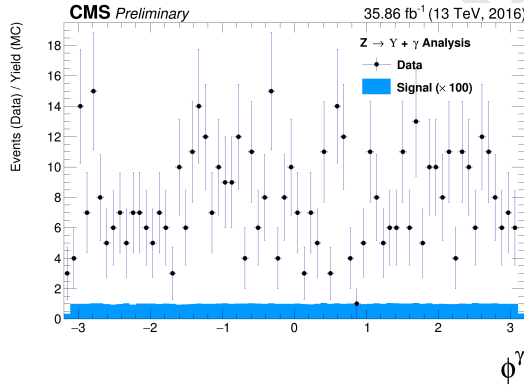


Figure 4.35: The  $\phi$  photon distributions from data and signal events of  $Z$  decaying in  $\Upsilon(1S, 2S, 3S) + \gamma$  after all (Group I+II) selection cuts. The plot is normalized to the number of events. Signal sample is scaled by a factor of  $\times 100$ .

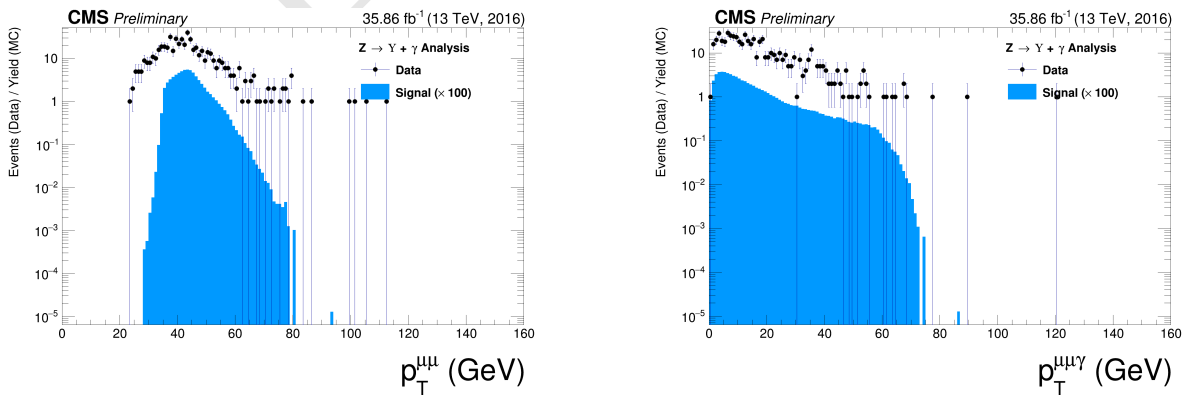


Figure 4.36: The  $p_T$  distributions for  $\Upsilon(1S, 2S, 3S)$  in the left and for  $Z$  in the right from data and signal events for  $Z$  decaying in  $\Upsilon(1S, 2S, 3S) + \gamma$  after all (Group I+II) selection cuts. The plots are normalized to the number of events. Signal sample is scaled by a factor of  $\times 100$ .

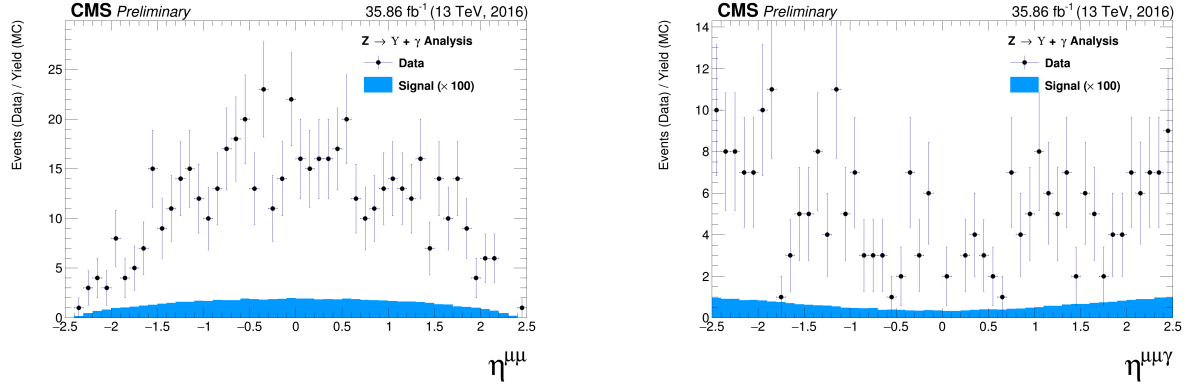


Figure 4.37: The  $\eta$  distributions for  $\Upsilon(1S, 2S, 3S)$  in the left and for  $Z$  in the right from data and signal events for  $Z$  decaying in  $\Upsilon(1S, 2S, 3S) + \gamma$  after all (Group I+II) selection cuts. The plots are normalized to the number of events. Signal sample is scaled by a factor of  $\times 100$ .

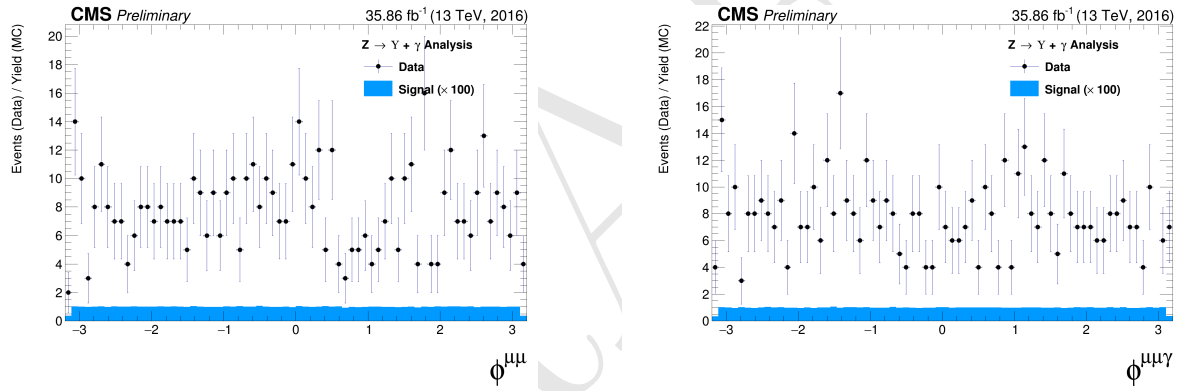


Figure 4.38: The  $\phi$  distributions for  $\Upsilon(1S, 2S, 3S)$  in the left and for  $Z$  in the right from data and signal events for  $Z$  decaying in  $\Upsilon(1S, 2S, 3S) + \gamma$  after all (Group I+II) selection cuts. The plots are normalized to the number of events. Signal sample is scaled by a factor of  $\times 100$ .

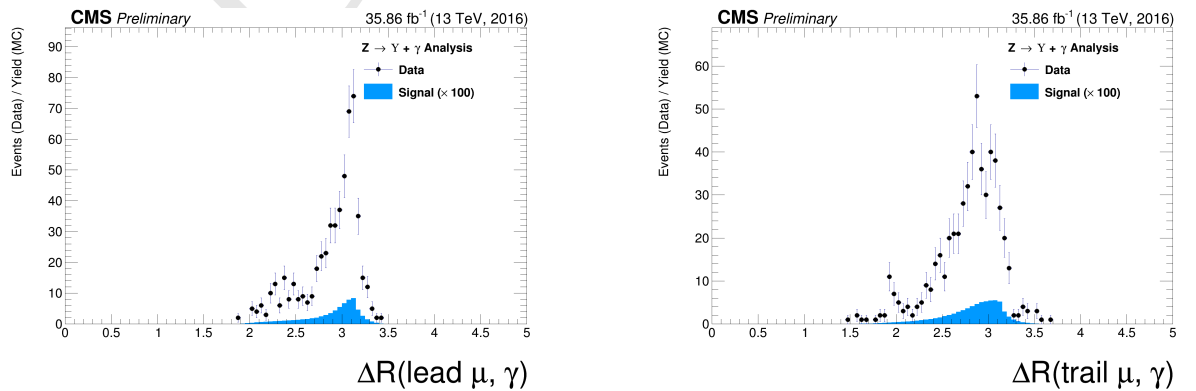


Figure 4.39: The  $\Delta R$  distributions between the photon and the leading muon (left) and the trailing muon (right) for  $\Upsilon(1S, 2S, 3S)$  from data and signal events for  $Z$  decaying after all (Group I+II) selection cuts. The plots are normalized to the number of events. Signal sample is scaled by a factor of  $\times 100$ .

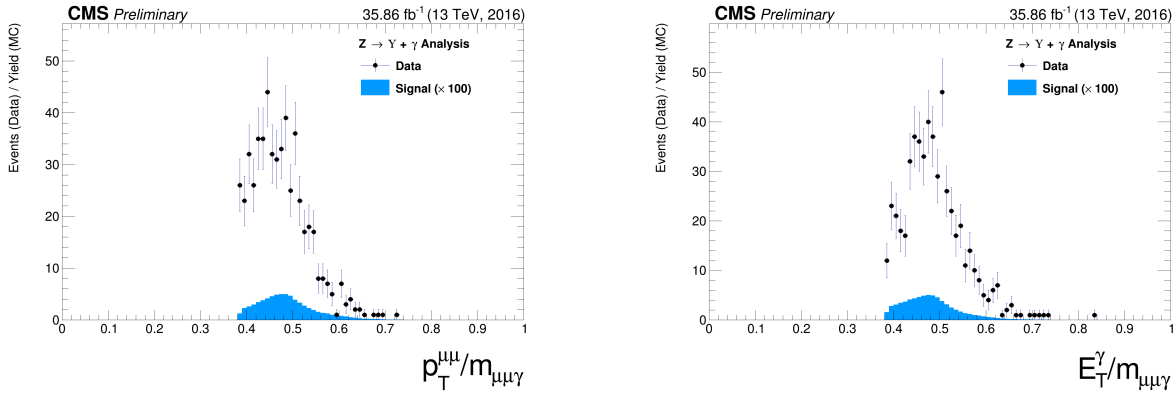


Figure 4.40: The ratio for the transverse momentum of the reconstructed Upsilon and the reconstructed Z mass ( $p_T^{\mu\mu}/M_{\mu\mu\gamma}$  - left) and the ratio for the transverse energy of the reconstructed Photon and the reconstructed Z mass ( $E_T^\gamma/M_{\mu\mu\gamma}$  - right) distribution for  $\Upsilon(1S, 2S, 3S)$  from data and signal events for Z decaying after all (Group I+II) selection cuts. The plots are normalized to the number of events. Signal sample is scaled by a factor of  $\times 100$ .

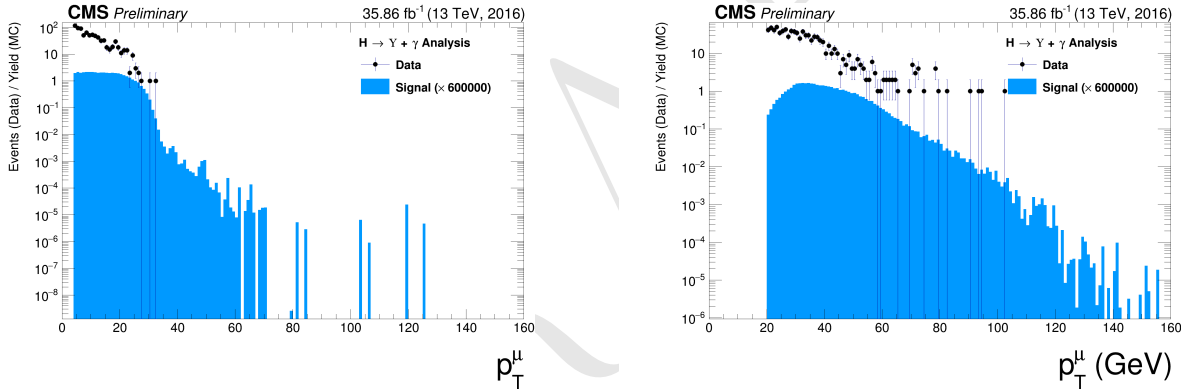


Figure 4.41: The  $p_T$  muon distributions from data and signal events for Higgs decaying in  $\Upsilon(1S, 2S, 3S) + \gamma$  after Group I of selection cuts, where on left are presenting the trailing muons and on right are the leading muons. The plots are normalized to the number of events. Signal sample is scaled by a factor of  $\times 600000$ .

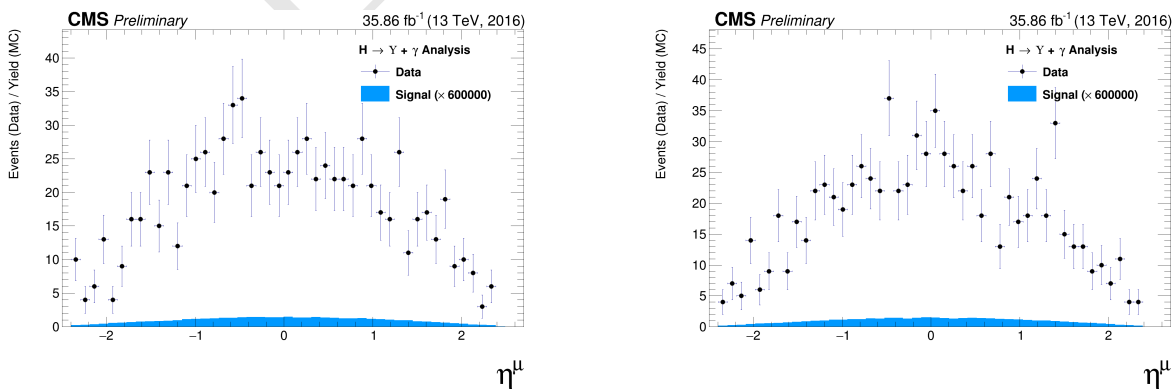


Figure 4.42: The  $\eta$  muon distributions from data and signal events of Higgs decaying in  $\Upsilon(1S, 2S, 3S) + \gamma$  after Group I of selection cuts, where on left are presenting the trailing muons and on right are the leading muons. The plots are normalized to the number of events. Signal sample is scaled by a factor of  $\times 600000$ .

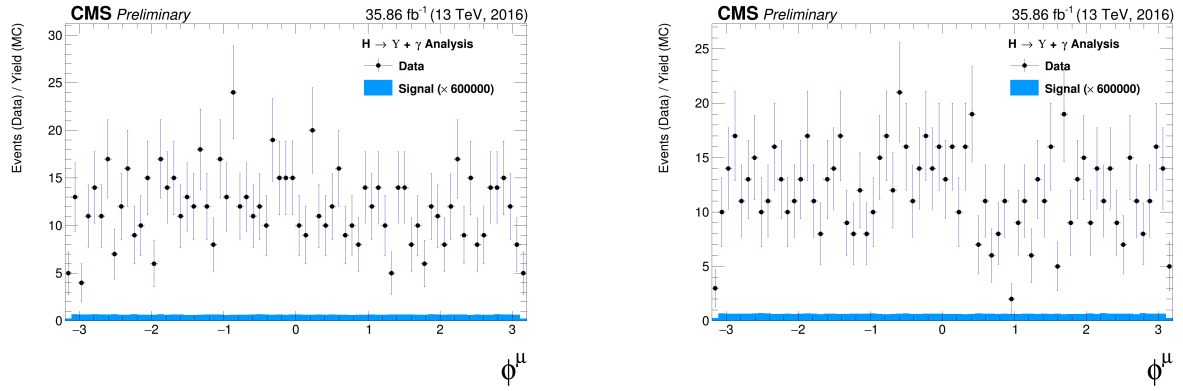


Figure 4.43: The  $\phi$  muon distributions from data and signal events of Higgs decaying in  $\Upsilon(1S, 2S, 3S) + \gamma$  after Group I of selection cuts, where on left are presenting the trailing muons and on right are the leading muons. The plots are normalized to the number of events. Signal sample is scaled by a factor of  $\times 600000$ .

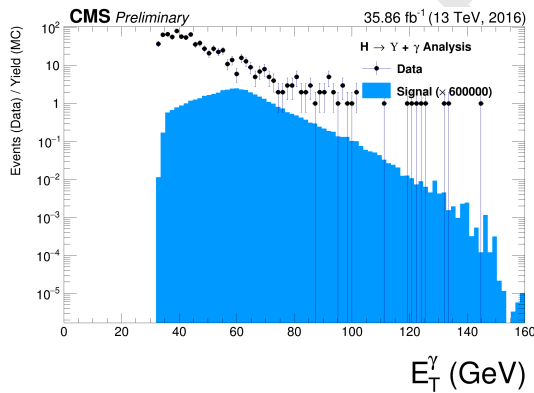


Figure 4.44: The  $p_T$  photon distributions from data and signal events for Higgs decaying in  $\Upsilon(1S, 2S, 3S) + \gamma$  all (Group I+II) selection cuts. The plot is normalized to the number of events. Signal sample is scaled by a factor of  $\times 600000$ .

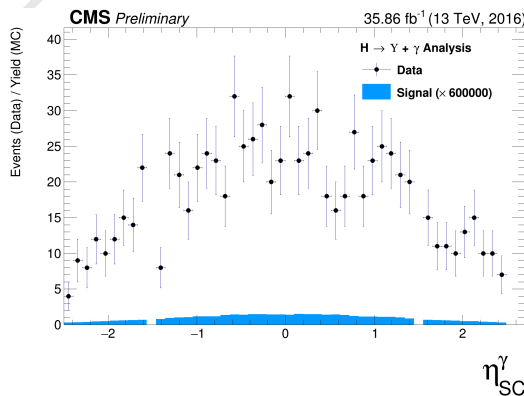


Figure 4.45: The  $\eta$  photon distributions from data and signal events of Higgs decaying in  $\Upsilon(1S, 2S, 3S) + \gamma$  after all (Group I+II) selection cuts. The plot is normalized to the number of events. Signal sample is scaled by a factor of  $\times 600000$ .

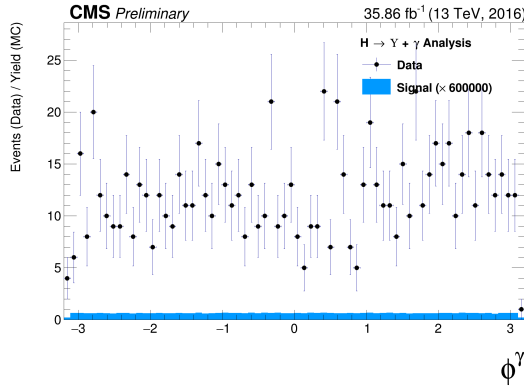


Figure 4.46: The  $\phi$  photon distributions from data and signal events of Higgs decaying in  $\Upsilon(1S, 2S, 3S) + \gamma$  after all (Group I+II) selection cuts. The plot is normalized to the number of events. Signal sample is scaled by a factor of  $c$ .

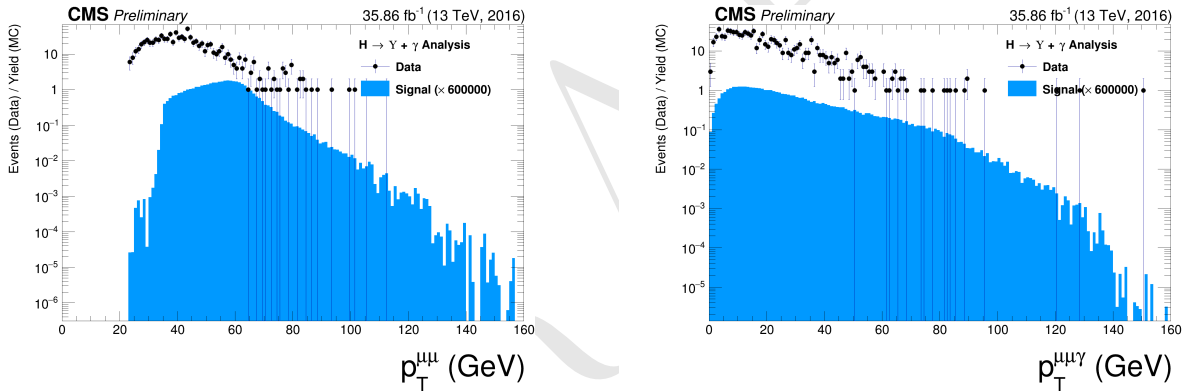


Figure 4.47: The  $p_T$  distributions for  $\Upsilon(1S, 2S, 3S)$  in the left and for Higgs in the right from data and signal events for Higgs decaying in  $\Upsilon(1S, 2S, 3S) + \gamma$  after all (Group I+II) selection cuts. The plots are normalized to the number of events. Signal sample is scaled by a factor of  $\times 600000$ .

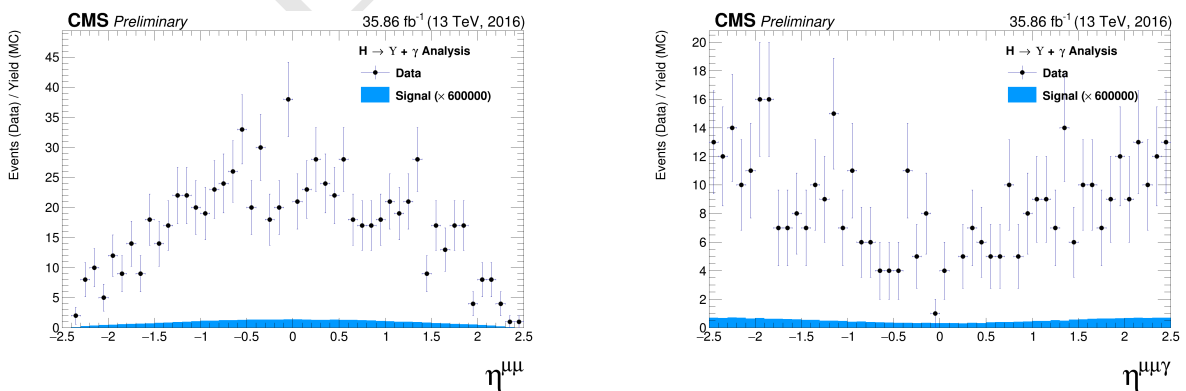


Figure 4.48: The  $\eta$  distributions for  $\Upsilon(1S, 2S, 3S)$  in the left and for Higgs in the right from data and signal events for Higgs decaying in  $\Upsilon(1S, 2S, 3S) + \gamma$  after all (Group I+II) selection cuts. The plots are normalized to the number of events. Signal sample is scaled by a factor of  $\times 600000$ .

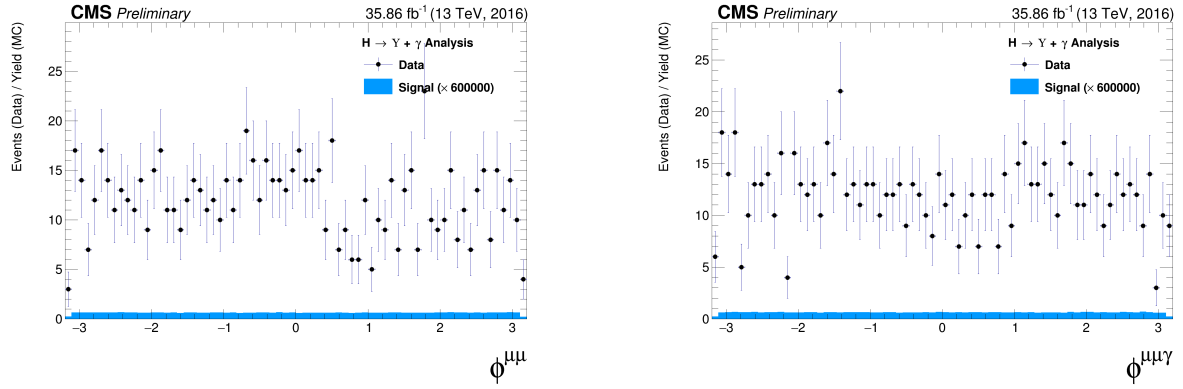


Figure 4.49: The  $\phi$  distributions for  $\Upsilon(1S, 2S, 3S)$  in the left and for Higgs in the right from data and signal events for Higgs decaying in  $\Upsilon(1S, 2S, 3S) + \gamma$  after all (Group I+II) selection cuts. The plots are normalized to the number of events. Signal sample is scaled by a factor of  $\times 600000$ .

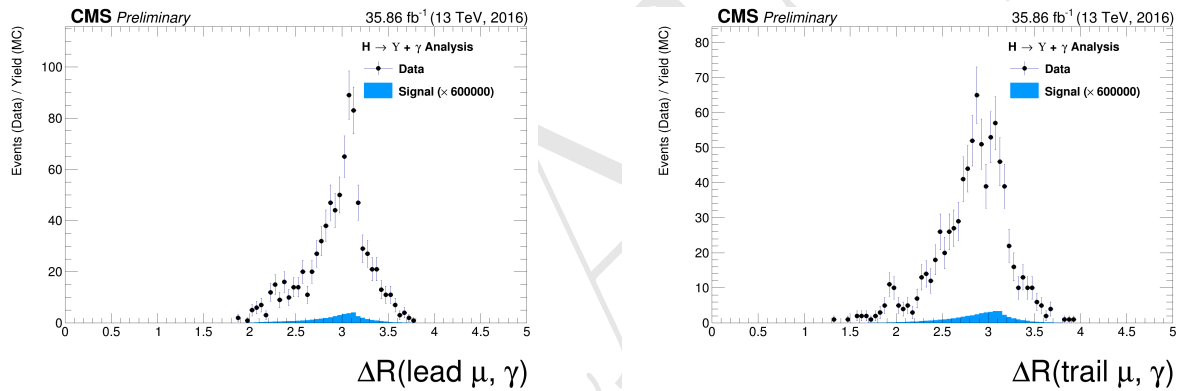


Figure 4.50: The  $\Delta R$  distributions between the photon and the leading muon (left) and the trailing muon (right) for  $\Upsilon(1S, 2S, 3S)$  from data and signal events for Higgs decaying after all (Group I+II) selection cuts. The plots are normalized to the number of events. Signal sample is scaled by a factor of  $\times 600000$ .

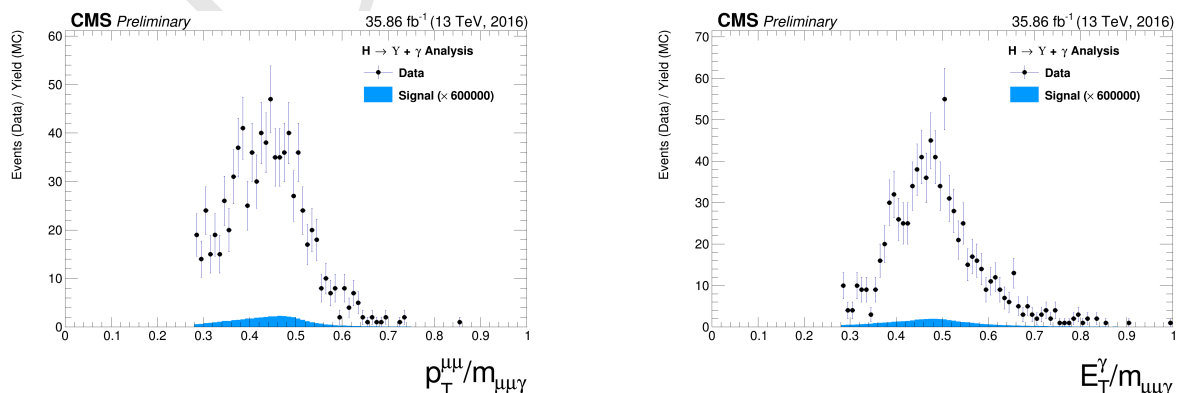


Figure 4.51: The ratio for the transverse momentum of the reconstructed Upsilon and the reconstructed Higgs mass ( $p_T^{\mu\mu}/M_{\mu\mu\gamma}$  - left) and the ratio for the transverse energy of the reconstructed Photon and the reconstructed Higgs mass ( $E_T^\gamma/M_{\mu\mu\gamma}$  - right) distribution for  $\Upsilon(1S, 2S, 3S)$  from data and signal events for Higgs decaying after all (Group I+II) selection cuts. The plots are normalized to the number of events. Signal sample is scaled by a factor of  $\times 600000$ .

## 509 4.7 Event categorization and yields

510 In order to increase the sensibility of the analysis, a categorization procedure was applied. They  
 511 are based on the  $\eta$  and R9 distribution of the reconstructed photon.

512 The photon R9 is a shower shape variable defined as the fraction of energy deposited in the  
 513 5x5 square surrounding the Super Cluster seed of the reconstructed photon. A photon that convert  
 514 before reaching the ECAL tend to have lower values of R9, in comparison with unconverted photons.  
 515 Converted photons have wider energy resolution and are more likely to be misidentified.

516 Selected events with the photon reconstructed inside the barrel and with  $R9 > 0.94$  are cat-  
 517 egorized as "EB High R9"<sup>6</sup>, selected events with the photon reconstructed inside the barrel and  
 518 with  $R9 < 0.94$  are categorized as "EB Low R9" and selected events with the photon reconstructed  
 519 inside the endcap, regardless of its R9 value, categorized as "EE". This categorization is done in  
 520 view of increase the analysis sensitivity.

521 This categorization is implemented only for the Z decay. The Higgs does not present enough  
 522 statistics to make it profitable, so only the inclusive one is used.

### 523 4.7.1 R9 reweighting

524 As spotted by the  $H \rightarrow \gamma\gamma$  at  $\sqrt{13}$  TeV analysis [54], there is a disagreement in the R9 distri-  
 525 bution of photons in Data and MC. In order to mitigate this difference, a transformation factor is  
 526 extracted and applied to the reconstructed photons before the categorization.

527 The same approach of the  $H \rightarrow \gamma\gamma$  analysis is applied, in which the nominal photon selection of  
 528 this analysis (see section 4.5.3) is used to select photons on Data and MC. Then the two distributions  
 529 are remapped and the transformation factors are extracted.

530 Figure 4.52 show the R9 distribution before and after the reweighting, for the Barrel and the  
 531 Endcap.

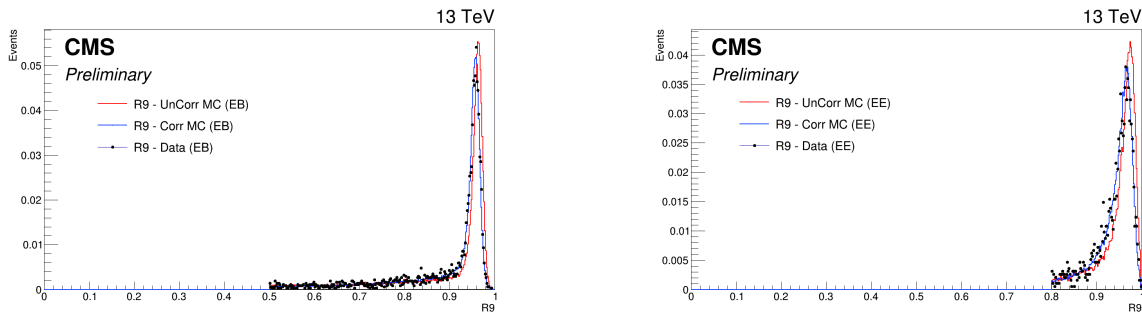


Figure 4.52: Data and MC of the R9 variable, before and after the reweighting. Barrel (left) and Endcap (right).

### 532 4.7.2 Event counting and yields

533 Tables 4.4 and 4.5 show the total number of events before and after the full selection. Two  
 534 things are important to notice.

535 The signal selection efficiency is between 20% and 21% for all  $\Upsilon$  states and categories.

<sup>6</sup>EB stands for Electromagnetic Barrel

	Data	Signal			$Z \rightarrow \mu\mu\gamma_{FSR}$
		$Z \rightarrow \Upsilon(1S) + \gamma$	$Z \rightarrow \Upsilon(2S) + \gamma$	$Z \rightarrow \Upsilon(3S) + \gamma$	
Total (before selection)	169.84 M	3.54	1.4	1.22	$3.33 \times 10^3$
Inclusive	447	0.393	0.157	0.136	176
EB High R9	197	0.172	0.0682	0.0597	78
EB Low R9	146	0.129	0.0519	0.0448	58.5
EE	104	0.0916	0.0365	0.032	39.8

Table 4.4: Number of events for the Z decay, before and after the full selection, per categorization scenarios.

	Data	Signal			$H \rightarrow \gamma\gamma^*$
		$H \rightarrow \Upsilon(1S) + \gamma$	$H \rightarrow \Upsilon(2S) + \gamma$	$H \rightarrow \Upsilon(3S) + \gamma$	
Total (before selection)	169.84 M	0.000257	$5.43 \times 10^{-5}$	$3.93 \times 10^{-5}$	136
Inclusive	231	$5.23 \times 10^{-5}$	$1.2 \times 10^{-5}$	$8.96 \times 10^{-6}$	1.22

Table 4.5: Number of events for the H decay, before and after the full selection.

When one compares the fraction of selected peaking background, with respect to the selected data events for the Higgs decay ( $1.22/231$ ), the fraction obtained ( $\sim 0.3\%$ ) is irrelevant. On the other hand, the same fraction for the Z decay ( $176/447$ ) is far from irrelevant ( $\sim 39\%$ )<sup>7</sup>. The same relation is not found in the  $H/Z \rightarrow J/\psi + \gamma$  analysis [23], where both decays (Higgs and Z) show neglectable estimations of peaking background contribution to data. The very same behavior was found by ATLAS [20]. It can be explained by the relatively larger cross-section of the Z peaking background ( $Z \rightarrow \mu\mu\gamma_{FSR}$ ), with respect to the Higgs peaking background (Higgs Dalitz Decay). For the  $J/\psi$  channel, it is not an issue since its cross-section is way larger than the peaking background. The figures 4.16 and 4.29 help to clarify these affirmations, for the Z and Higgs decay, respectively. One can easily see how clear the  $J/\psi$  peak is in both decays and how minor the Higgs Dalitz Decay contributions is to the  $\Upsilon$  peak, with respect to the  $Z \rightarrow \mu\mu\gamma_{FSR}$  contribution. It is important to keep in mind the different scaling of the peaking background distributions, x3 for the Z and  $\times 100$  for the Higgs. The peaking background to the data due to  $Z \rightarrow \Upsilon(1S, 2S, 3S) + \gamma$  channel is the main motivation to use a 2-dimensional modeling fitting of the signal and background events, in order to add one more layer of differentiation between many backgrounds contributions which will be detailed in the next section.

<sup>7</sup>It is worth to keep in mind that this is a estimation based on MC

## 552 4.8 Background modeling

553 The background modeling proposed for this analysis is a two dimensional unbinned maximum  
 554 likelihood fit on the  $\mu\mu$  and the  $\mu\mu\gamma$  invariant mass distributions. It is considered and modeled, as  
 555 briefly discussed in 4.1.2, three kinds of backgrounds:

- 556 • **Full Combinatorial:** any combination of two muon and one photon that pass all the object  
 557 reconstruction and event selection criteria.
- 558 •  **$\Upsilon$  Combinatorial:** a  $\Upsilon(1S, 2S, 3S)$ , that decays to a dimuon system, combined with a  
 559 misidentified photon (misreconstructed, Pile-up photon, etc.), that pass all the object re-  
 560 construction, identification and event selection criteria.
- 561 • **Peaking background:** a Z (or Higgs) that decays straight to a  $\mu\mu\gamma$ , that pass all the object  
 562 reconstruction and event selection criteria, without passing through any intermediate state.  
 563 The main contributions considered for this background are  $Z \rightarrow \mu\mu\gamma_{FSR}$  (a Z decaying to a  
 564 dimuon system with one of the muons irradiating a photon) or a Higgs Dalitz Decay.

565 All of them will be modeled from data, with some inputs from the MC (simulated) samples, as  
 566 explained below. For both invariant mass spectra ( $\mu\mu$  and  $\mu\mu\gamma$ ) the full combinatorial background is  
 567 expected to behave like a non-peaking distribution. The same behavior is expected for the  $\mu\mu\gamma$  mass  
 568 distribution of the  $\Upsilon$  Combinatorial background and for the  $\mu\mu$  mass distribution of the peaking  
 569 background.

570 On the other hand, the  $\mu\mu$  distribution of the  $\Upsilon$  Combinatorial background and the  $\mu\mu\gamma$  mass  
 571 distribution for the peaking background are expected to behave like a peaking distribution, centered  
 572 around the  $\Upsilon(1S, 2S, 3S)$  invariant mass (9.46 GeV, 10.02 GeV and 10.35 GeV) [2] and the Z  
 573 boson invariant mass (91.2 GeV) [2], respectively . Table 4.6 summarizes the background modeling  
 574 proposed for this analysis.

	$m_{\mu\mu}$	$m_{\mu\mu\gamma}$
Peaking background	Bernstein 1 <sup>st</sup> order	Crystal Ball (Higgs decay) Double Crystal Ball (Z decay)
$\Upsilon$ Combinatorial	3 Gaussians (one for each $\Upsilon$ state)	
Full Combinatorial	Chebychev 1 <sup>st</sup> order	Polynomial

574 Table 4.6: Modeling for each background source and mass component.

575 For the  $Z \rightarrow \Upsilon(1S, 2S, 3S) + \gamma$  analysis, the peaking background model parameters are extracted  
 576 by performing a simultaneous 2-dimensional fit over the invariant masses,  $m_{\mu\mu}$  and  $m_{\mu\mu\gamma}$ , of the  
 577 simulated  $Z \rightarrow \mu\mu\gamma_{FSR}$  MC sample of events that passes the selection described in Section 4.4, as in  
 578 figure 4.53. Once the parameters are extracted, they are fixed and the *pdf* (Probability Distributions  
 579 Function) of the 2-Dimensional modeling is stored, leaving only the normalization of the *pdf* as a  
 580 parameter free to float (this will be determined from data).

581 In order to describe the 2-dimensional invariant mass distribution of the Peaking Background,  
 582 as stated in Table 4.6, the  $m_{\mu\mu}$  component is described by a Bernstein polynomial of 1<sup>st</sup> order [55],

which is used here just a representation of a linear function. The  $m_{\mu\mu\gamma}$  component is described by Double Crystal Ball function [56]. A Crystal Ball function is a *pdf* composed by a gaussian distribution and a power-law tail to the left, before certain threshold. The Crystal Ball function was named after the Crystal Ball Collaboration (first to use this *pdf*) and it is widely used in high-energy physics to describe mass distributions that incorporate FSR (final state radiation) effects, via the power-law tail. A Double Crystal Ball is a Crystal Ball function with the power-law tail on both sides.

A Crystal Ball function is define as:

$$CB(x; \alpha, n, \bar{x}, \sigma) = N \cdot \begin{cases} \exp\left(-\frac{(x-\bar{x})^2}{2\sigma^2}\right), & \text{for } \frac{x-\bar{x}}{\sigma} > -\alpha \\ A \cdot (B - \frac{x-\bar{x}}{\sigma})^{-n}, & \text{for } \frac{x-\bar{x}}{\sigma} \leq -\alpha \end{cases}, \quad (4.4)$$

where,

$$A = \left(\frac{n}{|\alpha|}\right)^n \cdot \exp\left(-\frac{|\alpha|^2}{2}\right),$$

$$B = \frac{n}{|\alpha|} - |\alpha|,$$

$$N = \frac{1}{\sigma(C+D)},$$

$$C = \frac{n}{|\alpha|} \cdot \frac{1}{n-1} \cdot \exp\left(-\frac{|\alpha|^2}{2}\right),$$

$$D = \sqrt{\frac{\pi}{2}} \left(1 + \text{erf}\left(\frac{|\alpha|}{\sqrt{2}}\right)\right),$$

and *erf* is the error function.

For the three gaussian functions fits, which represent the three  $\Upsilon$  states (1S, 2S and 3S) from the  $\Upsilon$  Combinatorial background in the  $m_{\mu\mu}$  component, we use a  $\Upsilon$  control sample in order to extract the fit parameters, including the relative normalization between each  $\Upsilon$  state. This sample is composed by dimuon candidates obtained from data, by selecting the events that passes the same trigger and dimuon selection of the nominal selection and with  $p_T^{\mu\mu} > 35$  GeV (this cut is done in order to keep this selected dimuon candidates compatibles with the  $p_T^{\mu\mu}/M_{\mu\mu\gamma}$  cut applied in the nominal selection). No selection or cuts in the photon are required.

This control sample is fitted with a Chebychev 1<sup>st</sup> order (linear polynomial) for the background support and 3 gaussian with the following constraints:

- the mean of each state should be the ones in the PDG [2], but allowed to shift by a float and common (the same for all states) value.
- the sigma should be based on the 1S fit of the MC. All other sigma should be the result of the 1S sigma times the state mass over the 1S mass ( $\sigma_{2S,3S} = \frac{m_{2S,3S}}{m_{1S}} \sigma_{1S}$ ).

The idea behind this fit is that scale and resolution (mean and sigma, respectively, of the gaussians) over a sample without a photon selection should be the same as over a sample with photon selection, since these are detector only dependent effects. The fact that we exclude the photon from this control sample, improves the statistics and gives a better measurement of these variables.

The fit of the  $\Upsilon$  control sample if shown in figure 4.54.

Once determined, the fit parameters are fixed, they are used to compose the 2-Dimensional *pdf*. The  $m_{\mu\mu}$  component of the full combinatorial background is derived fully from the data fit

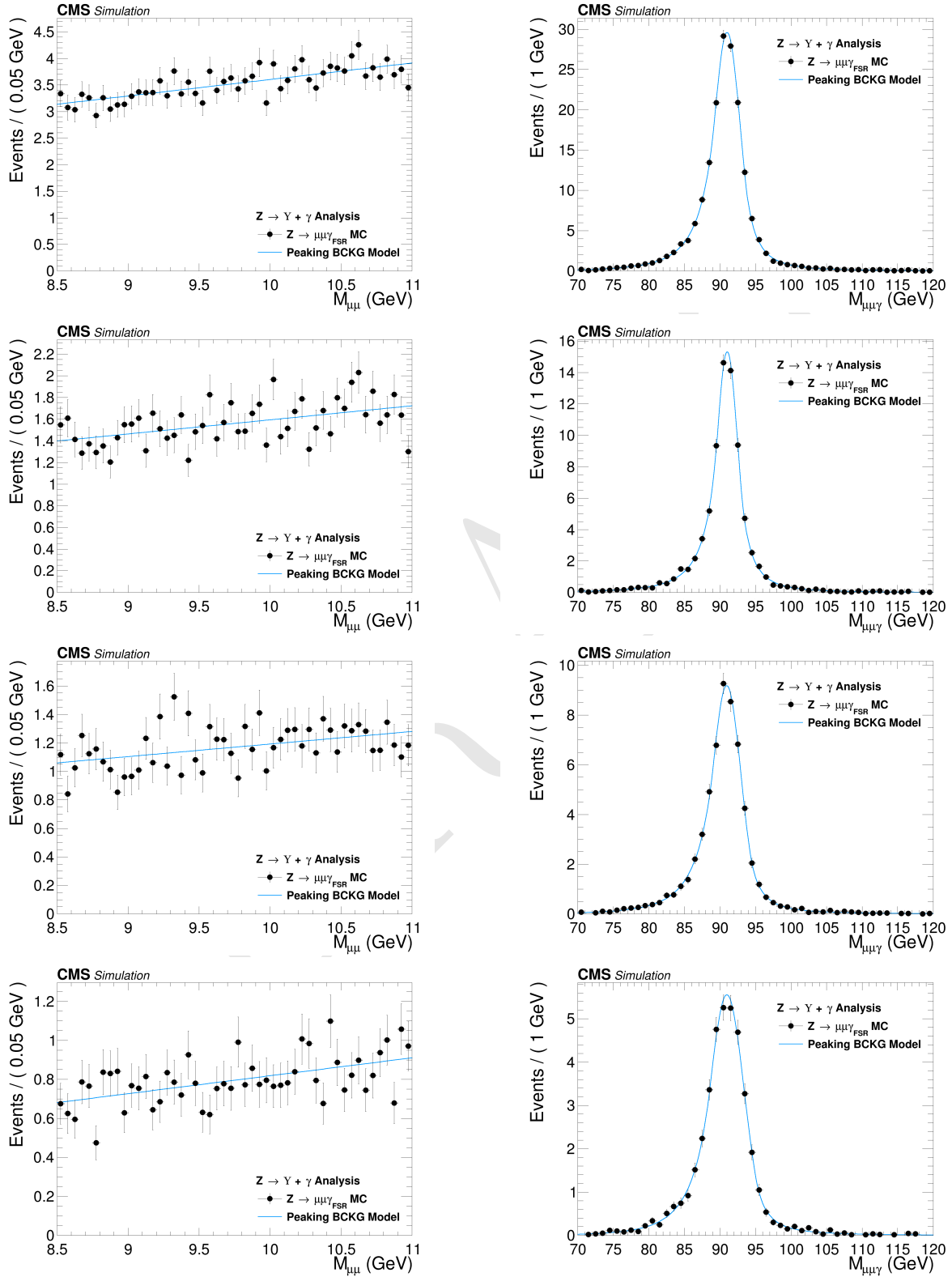


Figure 4.53: Peaking background for the  $Z \rightarrow \Upsilon(1S, 2S, 3S) + \gamma$  analysis.  $\mu\mu$  mass distribution (left) and  $\mu\mu\gamma$  invariant mass distribution (right). From top to bottom categories: Inclusive, EB High R9, EB Low R9, EE.

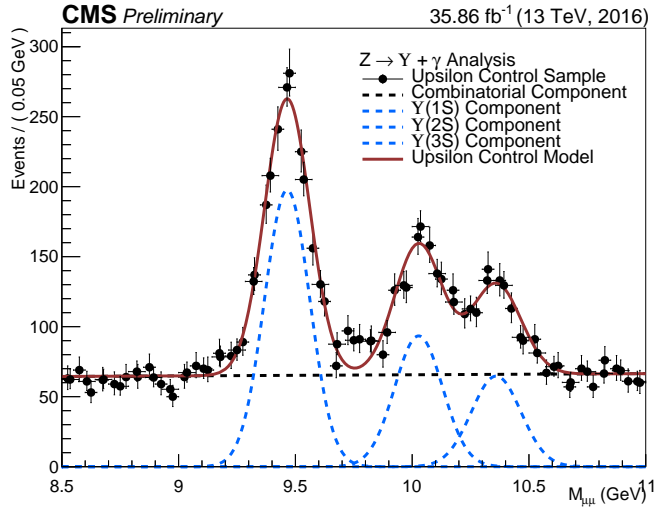


Figure 4.54:  $\Upsilon$  control sample fit with Chebychev 1<sup>st</sup> order for the background support and 3 gaussian for the three  $\Upsilon(1S, 2S, 3S)$  peaks.

(described below). In the same sense, the  $m_{\mu\mu\gamma}$  component of the full combinatorial and the  $\Upsilon(nS)$  Combinatorial backgrounds are also fully derived from the data, but following a more complex procedure: a composition with the *pdf* components described above, plus a statistical test, to avoid overfitting within a Discrete Profiling (or "Envelope Method"), as described in [57] and also implemented in [54].

The statistical test consists of, for each category, different orders of a set of polynomial *pdfs* families are tested: a sums of exponentials, sum of polynomials (in the Bernstein basis), a Laurent series and a sums of power-law functions.

- Sums of exponentials:

$$f_N(x) = \sum_{i=1}^N p_{2i} e^{p_{2i+1}x},$$

- Sums of polynomials (in the Bernstein basis):

$$f_N(x) = \sum_{i=0}^N p_i b_{(i,N)}, \text{ where } b_{(i,N)} := \binom{N}{i} x^i (1-x)^{N-i},$$

- Laurent series:

$$f_N(x) = \sum_{i=1}^N p_i x^{-4+\sum_{j=1}^i (-1)^j(j-1)},$$

- Sums of power-law functions:

$$f_N(x) = \sum_{i=1}^N p_{2i} x^{-p_{2i+1}},$$

where for all  $k$ , the  $p_k$  are a set of floating parameters in the fit.

Twice difference in the negative log-likelihood ( $NLL$ ) between the  $N^{th}$  and the  $(N+1)^{th}$  order of the same polynomial ( $\Delta NLL = 2 \times (NLL_N - NLL_{N+1})$ ) is expected to follow a  $\chi^2$  distribution

with  $M$  degrees of freedom, where  $M$  is the increase in degrees of freedom when going from  $N^{th}$  to  $(N + 1)^{th}$ . This can be shown with the help of the Wilks' theorem [58].

Starting from the lowest order possible, the best choice of order, for each family, is determined when a increase in the order of the polynomial, does not brings a significant improvement in the quality of the fit. Since a model with more fit parameters (higher order polynomials) will always perform, if not the same, better than a simpler one, an optimal choice of the polynomial order, will be the one right before the model becomes too flexible for the data.

Consider a  $p$ -value defined as:

$$\begin{aligned} p\text{-value} &= \int_{\Delta NLL}^{\infty} \chi_M^2(\Delta) d\Delta \\ &= P(\chi_M^2 > \Delta NLL), \end{aligned} \quad (4.5)$$

In the same spirit as the Wilks' theorem, this is the  $p$ -value for a likelihood ratio test between a null hypotheses and an alternative model, where the null hypotheses is the  $N^{th}$  order and  $(N + 1)^{th}$  order is the alternative one.

$$\begin{aligned} \Delta NLL &= 2 \times (NLL_N - NLL_{N+1}) \\ &= -2 \times \log\left(\frac{\mathcal{L}_N}{\mathcal{L}_{N+1}}\right), \end{aligned} \quad (4.6)$$

where  $\mathcal{L}_N$  is the likelihood for the  $N^{th}$  polynomial order.

The alternative will present a statistically significant improvement, with respect to the null hypotheses, if the  $p$ -value is smaller than 0.05, since the probability of obtaining, by chance, considering the null hypotheses is true, a even higher  $\Delta NLL$  is less than 5%. This will give support to chose  $(N + 1)^{th}$  over  $N^{th}$ .

If the  $p$ -value is greater than 0.05 a higher order is not supported, since the probability of obtaining a  $\Delta NLL$  greater than the one observed is statistically significant (more than 5%). A higher  $\Delta NLL$  means that another data sample, collected and analyzed with strictly the same conditions, would have a probability of more than 5% of giving a better fit improvement than the one observed, again assuming that the null hypotheses is true. This is an indication of overfitting, since the improvements are likely to come from just statistical fluctuations. When testing the  $(N + 1)^{th}$  order and this condition is reached, the optimal order should be the  $N^{th}$ .

At first, before any fit to data, the 2-Dimensional model is composed by the five components, as described in Table 4.6 (in which the  $m_{\mu\mu\gamma}$  modeling for the Full Combinatorial Background and the  $\Upsilon$  combinatorial are shared), then, the statistical test described before is ran for each family. It is important to stress that before the statistical test all the other fitting parameters have been fixed. This leaves only the normalizations of the model components and the polynomial coefficients free to float.

Once the optimal order for each  $pdf$  family is obtained, the composed  $pdf$  with each choice from statistical test is save in the same model, providing a discrete variable that indexes the different polynomial  $pdf$  families. This method is called Discrete Profiling (or "Envelope Method") and it

allows the analysis algorithm to treat the choice of the *pdf* as a systematics and incorporate its effect in the extracted upper limits. This model, with different choices of polynomial families is called envelope.

The implementation, used in the analysis, of the F-Test and the Discrete Profiling is based on the same algorithm used by the  $H \rightarrow \gamma\gamma$  Run II analysis. An extensive documentation on these methods can be found in  $H \rightarrow \gamma\gamma$  analysis note and physics analysis summary [59, 60] and in the specific reference of the Discrete Profiling [57]. The figures 4.55 and 4.56 show the projection for the  $\mu\mu$  and  $\mu\mu\gamma$  distribution after the F-Test.

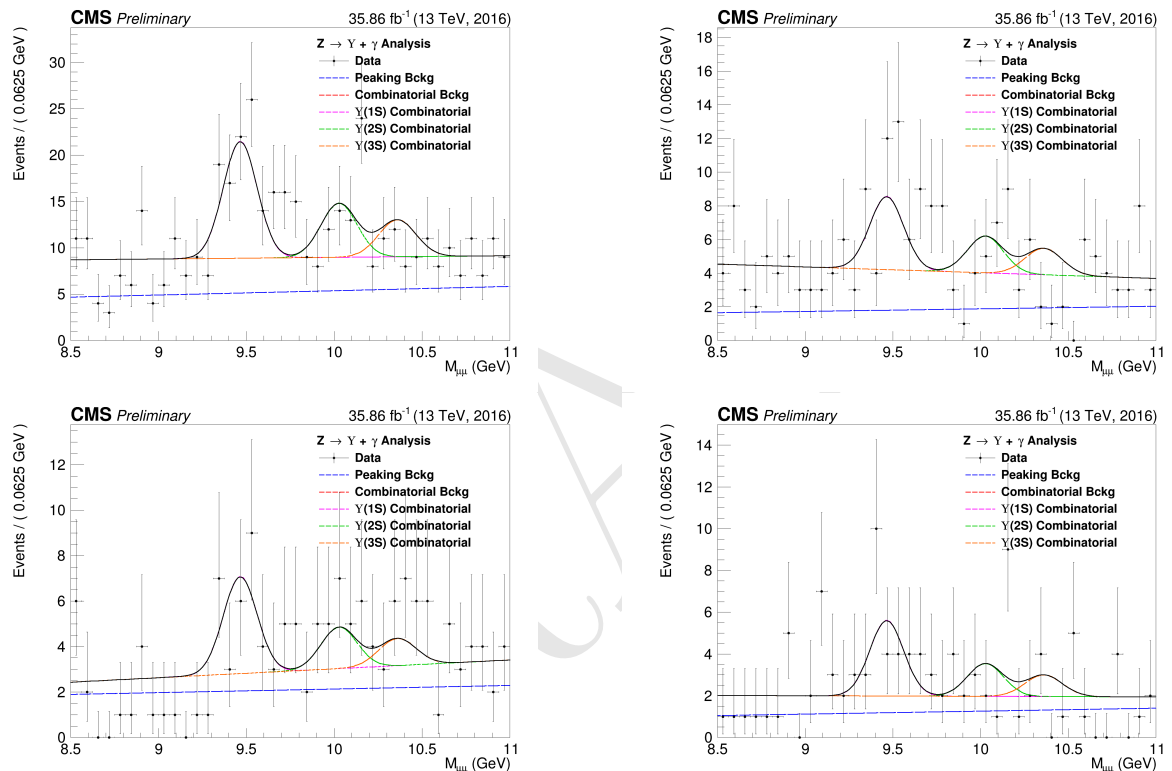


Figure 4.55:  $Z \rightarrow \Upsilon(1S, 2S, 3S) + \gamma$  Background Modeling:  $\mu\mu$  distribution. Inclusive (top left); EB High R9 (top right), EB Low R9 (bottom left), EE (bottom right). The pdfs projections are plotted with respect to the overall best choice of the statistica test.

For the  $H \rightarrow \Upsilon(1S, 2S, 3S) + \gamma$  analysis, the same procedure is implemented, except for the peaking background modeling. Since the MC prediction for the contribution of the background is too small, according to the comparison between the final selected events for data and the Higgs Dalitz Decay sample, in order to avoid fitting over statistical fluctuations of the data sample, the Peaking Background, for the Higgs channel, is fully modeled from the MC sample, including its normalization, as shown in figure 4.57, hence it is not included the the statistical test, neither in the final background modeling envelope.

The results of the background modeling for the Full Combinatorial and  $\Upsilon$  Combinatorial, can be found at Figures 4.58 and 4.59, for the  $\mu\mu$  and  $\mu\mu\gamma$  distribution, respectively. It is worth to remember that, for the Higgs channel, we are not implementing any categorization.

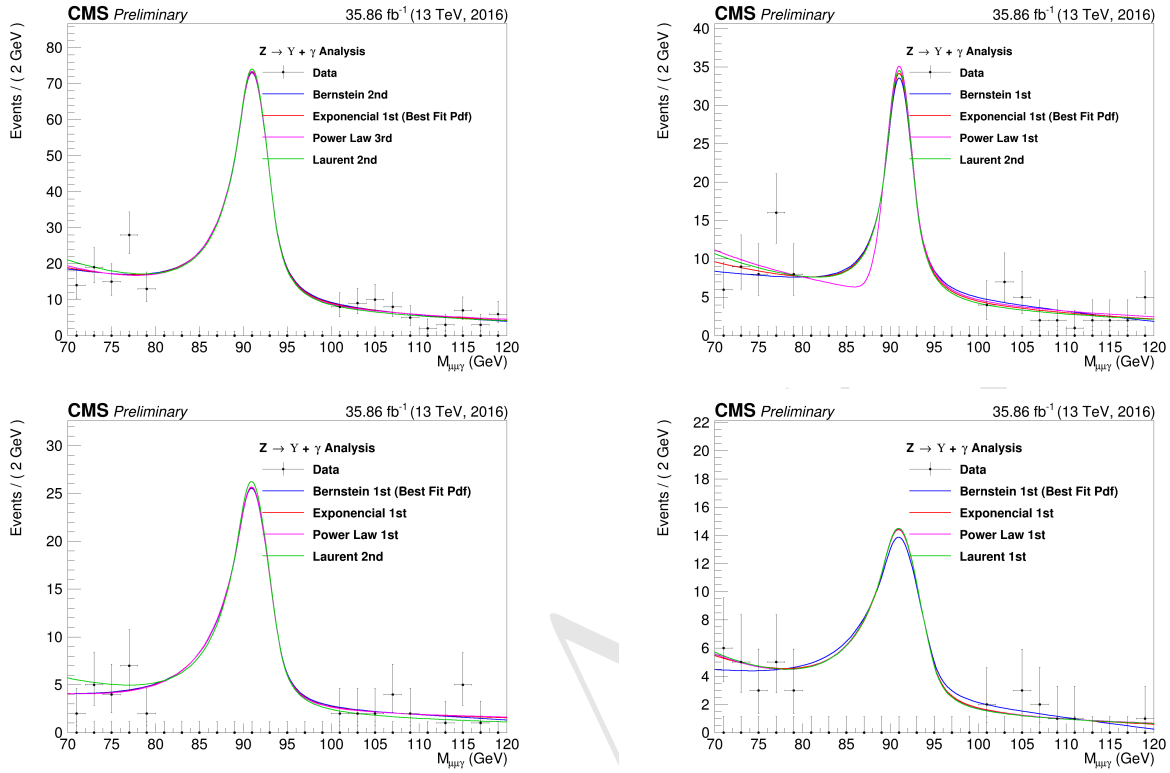


Figure 4.56:  $Z \rightarrow \Upsilon(1S, 2S, 3S) + \gamma$  Background Modeling:  $\mu\mu\gamma$  distribution. Inclusive (top left); EB High R9 (top right), EB Low R9 (bottom left), EE (bottom right). The plotted *pdfs* corresponds to the best choice by the statistical test for each family. The signal region, from 80 GeV to 100 GeV was blinded.

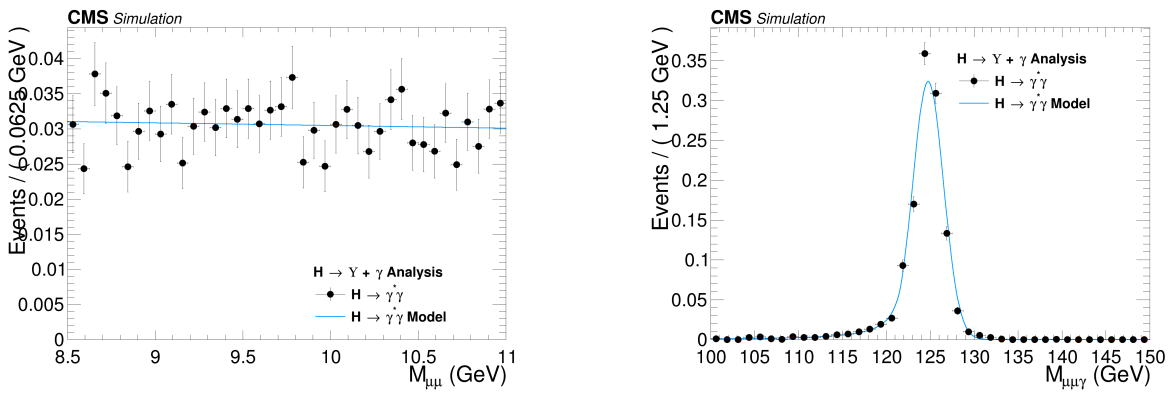


Figure 4.57: Peaking Background for the  $H \rightarrow \Upsilon(1S, 2S, 3S) + \gamma$  analysis.  $m_{\mu\mu}$  invariant mass distribution (left) and  $m_{\mu\mu\gamma}$  invariant mass distribution (right).

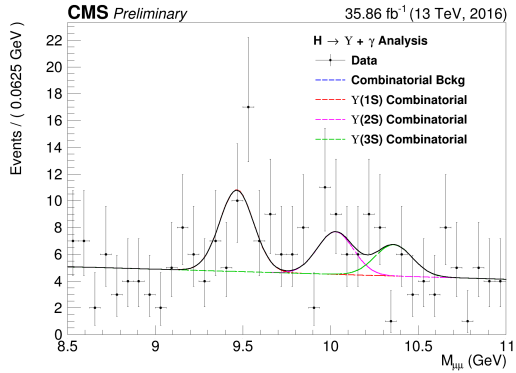


Figure 4.58:  $H \rightarrow \Upsilon(1S, 2S, 3S) + \gamma$  Background Modeling:  $m_{\mu\mu}$  distribution. The *pdfs* are plotted with respect to the overall best choice of the statistical test.

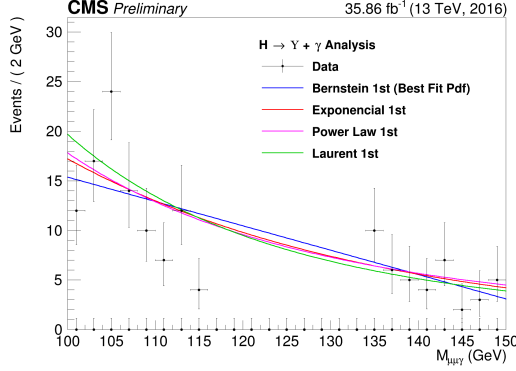


Figure 4.59:  $H \rightarrow \Upsilon(1S, 2S, 3S) + \gamma$  Background Modeling:  $\mu\mu\gamma$  distribution. The plotted *pdfs* corresponds to the best choice by the statistical test for each family. The signal region, from 115 GeV to 135 GeV was blinded.

## 680 4.9 Signal modeling

681 Along the same lines as the background modeling (Section 4.8), the signal modeling is imple-  
 682 mented as a two dimensional unbinned maximum likelihood fit on the  $m_{\mu\mu}$  and the  $m_{\mu\mu\gamma}$  invariant  
 683 masses distributions, but this time, only using the signal simulated MC samples 4.1.2. Since, for  
 684 the two spectra, it is expected a peak-like distribution, one centered in the Z (or Higgs) boson mass  
 685 and the other centered in the  $\Upsilon$  mass, two also peak-like analytics *pdfs* were chosen to compose the  
 686 signal model. The modeling is summarized in table 4.7.

	$m_{\mu\mu}$	$m_{\mu\mu\gamma}$
$Z \rightarrow \Upsilon(1S, 2S, 3S) + \gamma$	Double Crystal Ball	Double Crystal Ball
$H \rightarrow \Upsilon(1S, 2S, 3S) + \gamma$	Double Crystal Ball	Crystal Ball + Gaussian with the same mean

Table 4.7: Modeling for each signal source and mass component.

687 The projections of the modeling for the Z boson decay channel analysis can be found at figures  
 688 4.60, 4.61, 4.62 and 4.63, for Inclusive, EB High R9, EB Low R9 and EE, respectively. The projection  
 689 on the modeling for the Higgs boson signal can be found at Figure 4.64. A deeper discussion on the  
 690 systematics uncertainties associated to them, will be presented in the next section.

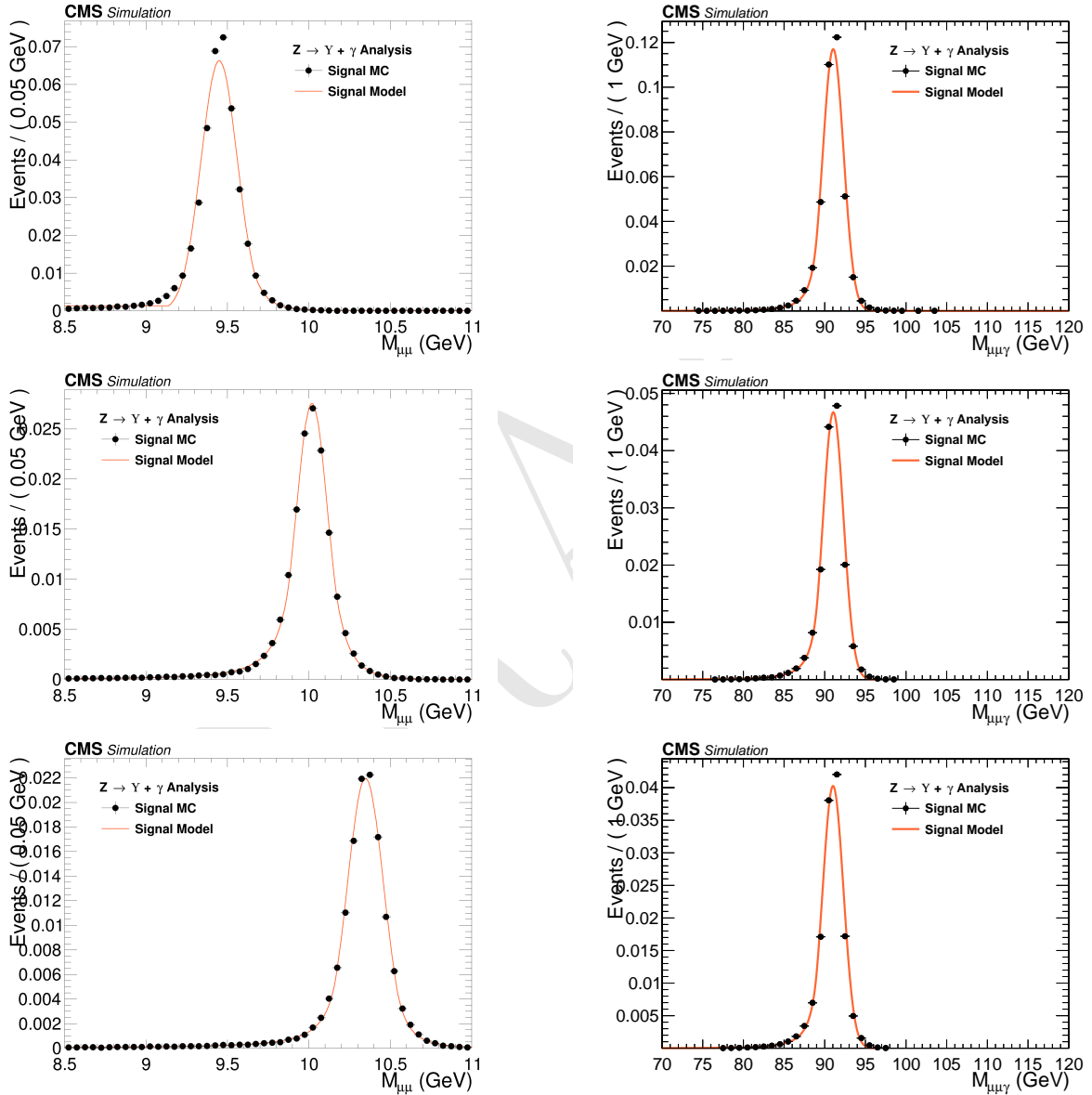


Figure 4.60: Signal Modeling for the  $Z \rightarrow \Upsilon(1S, 2S, 3S) + \gamma$  analysis for Inclusive category.  $m_{\mu\mu}$  mass distribution (left) and  $m_{\mu\mu\gamma}$  mass distribution (right). From top to bottom:  $\Upsilon(1S)$ ,  $\Upsilon(2S)$ ,  $\Upsilon(3S)$ .

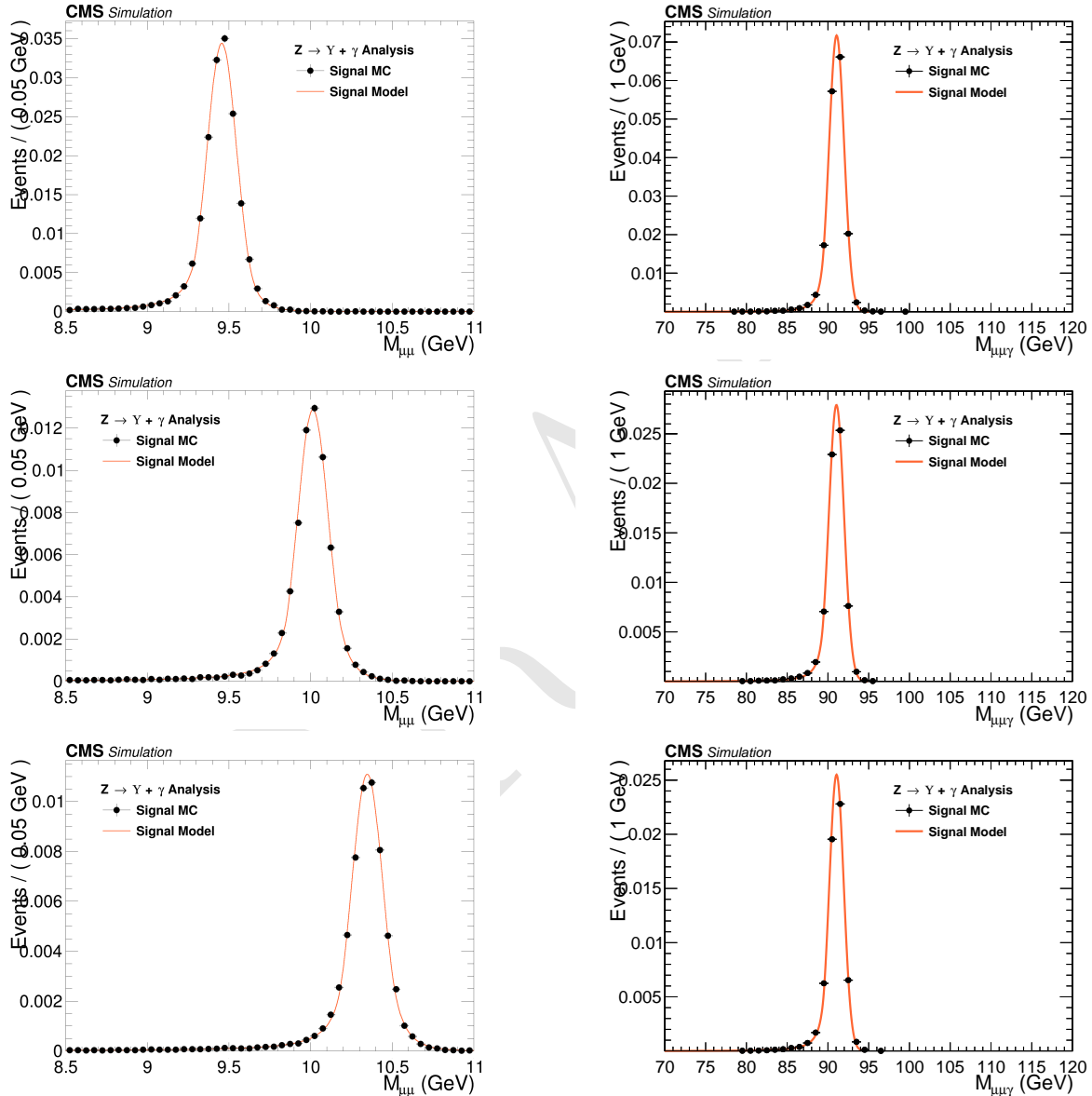


Figure 4.61: Signal Modeling for the  $Z \rightarrow \Upsilon(1S, 2S, 3S) + \gamma$  analysis for EB High R9 category.  $m_{\mu\mu}$  mass distribution (left) and  $m_{\mu\mu\gamma}$  mass distribution (right). From top to bottom:  $\Upsilon(1S)$ ,  $\Upsilon(2S)$ ,  $\Upsilon(3S)$ .

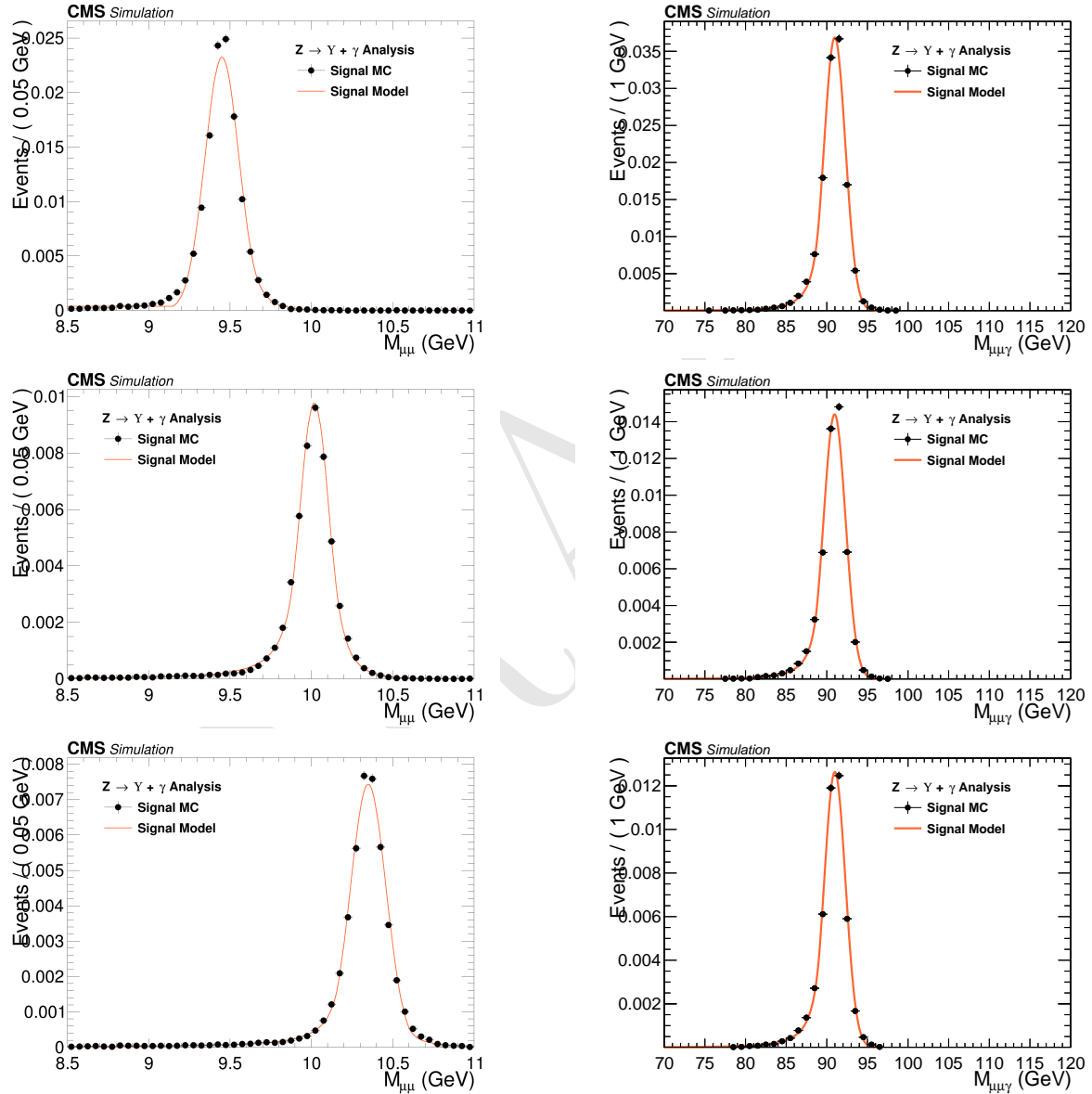


Figure 4.62: Signal Modeling for the  $Z \rightarrow \Upsilon(1S, 2S, 3S) + \gamma$  analysis for EB Low R9 category.  $m_{\mu\mu}$  mass distribution (left) and  $m_{\mu\mu\gamma}$  mass distribution (right). From top to bottom:  $\Upsilon(1S)$ ,  $\Upsilon(2S)$ ,  $\Upsilon(3S)$ .

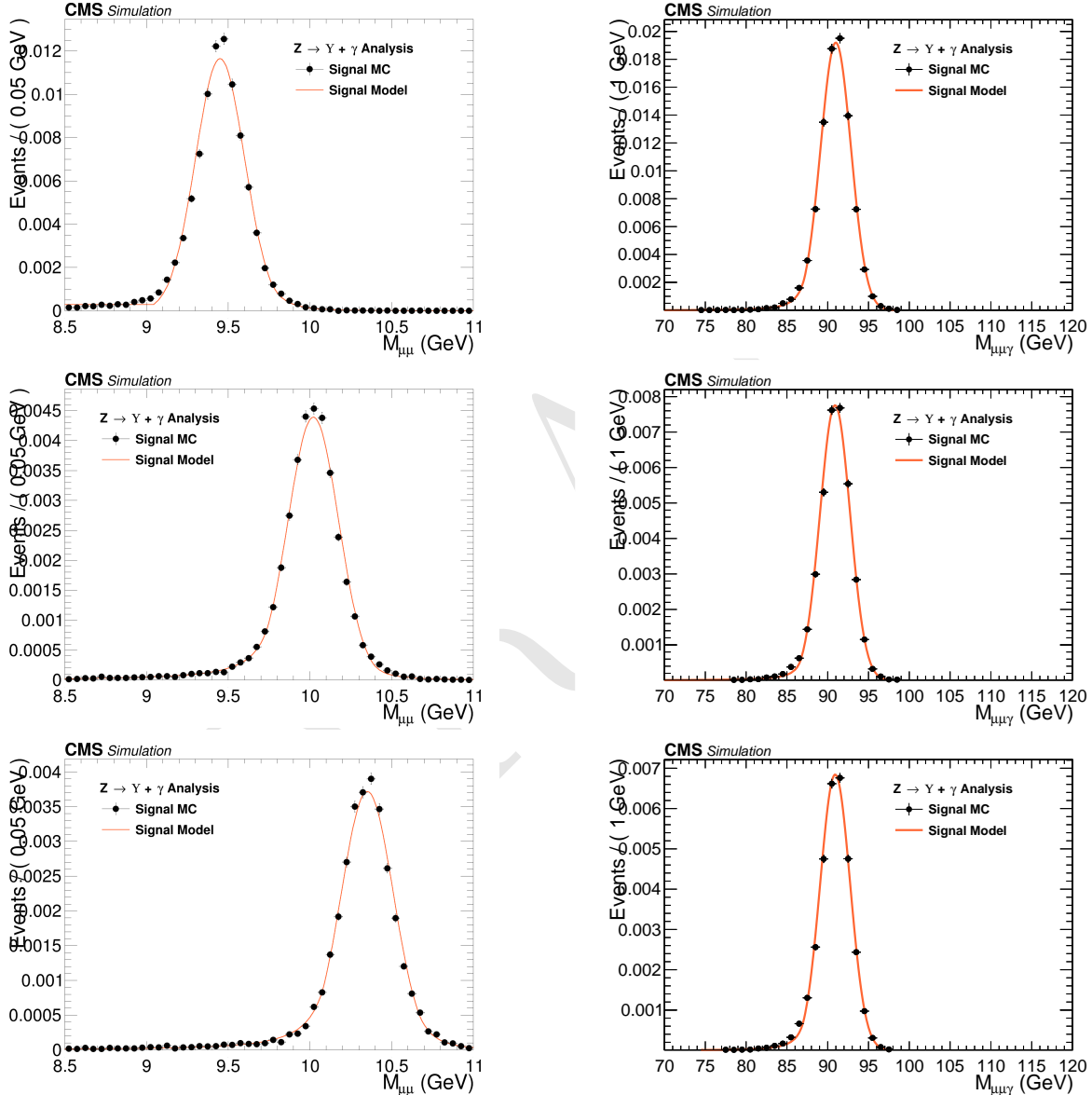


Figure 4.63: Signal Modeling for the  $Z \rightarrow \Upsilon(1S, 2S, 3S) + \gamma$  analysis for EE category.  $m_{\mu\mu}$  mass distribution (left) and  $m_{\mu\mu\gamma}$  mass distribution (right). From top to bottom:  $\Upsilon(1S)$ ,  $\Upsilon(2S)$ ,  $\Upsilon(3S)$ .

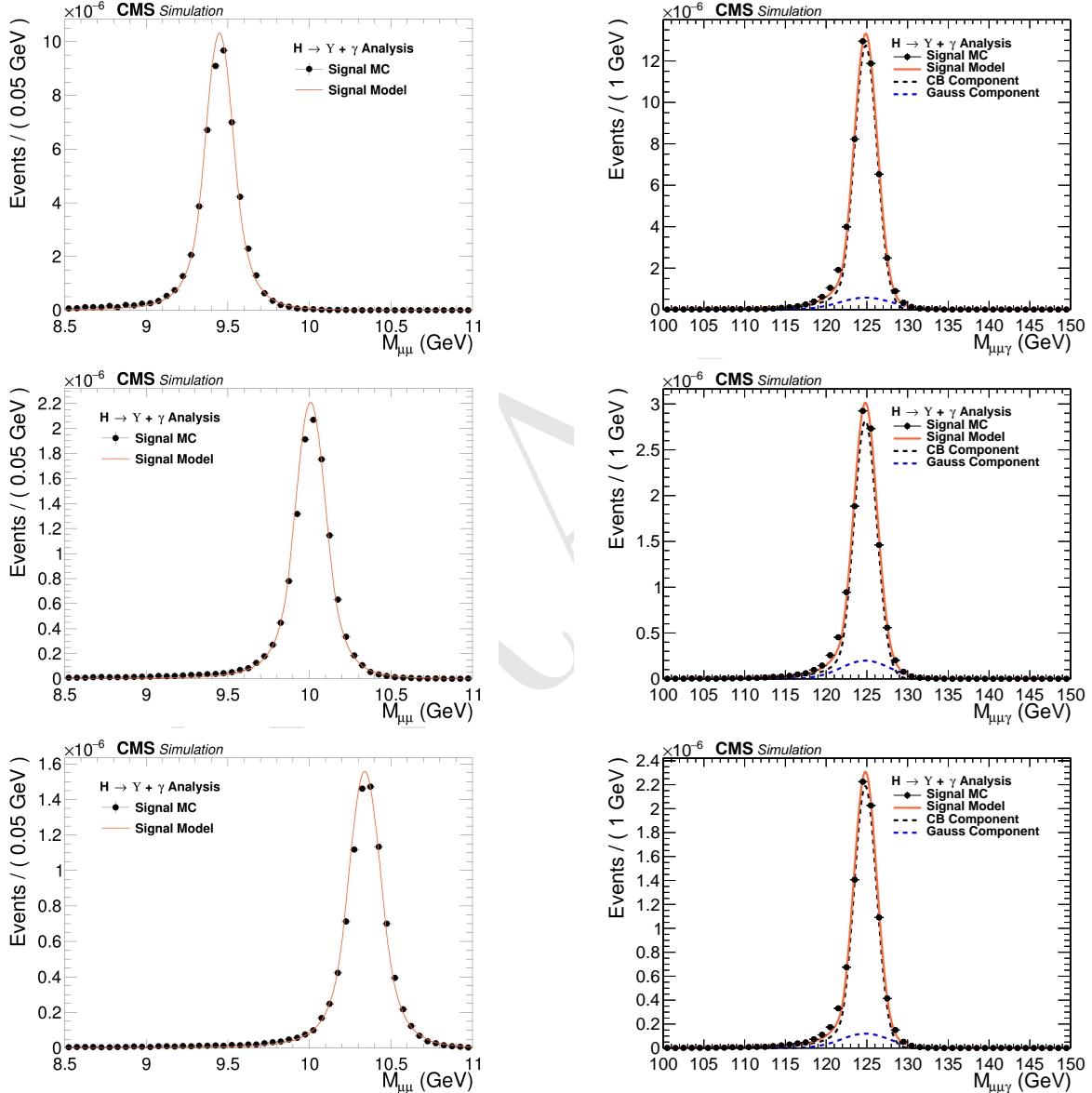


Figure 4.64: Signal Modeling for the  $H \rightarrow \Upsilon(1S, 2S, 3S) + \gamma$ .  $m_{\mu\mu}$  mass distribution (left) and  $m_{\mu\mu\gamma}$  mass distribution (right). From top to bottom:  $\Upsilon(1S)$ ,  $\Upsilon(2S)$ ,  $\Upsilon(3S)$ .

## 691 4.10 Systematic uncertainties

692 The sources of systematic uncertainties considered are those affect the predicted yields, as shown  
 693 in Section 4.7.2, such as, luminosity measurement [32], the pile-up description in the simulations,  
 694 the corrections applied to the simulated events in order to compensate for the differences in per-  
 695 formance of the some selection criteria as the trigger, object reconstruction and identification, the  
 696  $\Upsilon$  polarization and the theoretical uncertainties, such as the effects of the *parton density functions*  
 697 (PDF) to the signal cross section [41, 61, 62], the variations of the renormalization and factorization  
 698 scales [63–67], and the prediction of the decay branching ratios.

699 The other kind uncertainties affect the shape of the signal model. Those are related with possible  
 700 imprecisions of the momentum scale and resolution and they are measured as how they affect the  
 701 the mean and sigma of the signal model. For the background modeling, since it is derived from  
 702 data, the choice of the *pdf* (Probability distribution function) is the only systematic uncertainties  
 703 considered. It is treated by the Discrete Profiling method, as described in section 4.8. The two  
 704 kinds of systematics uncertainties are described in details below.

### 705 4.10.1 Uncertainties on the predicted signal yields

- 706 • **Theoretical uncertainties:** the theoretical sources of uncertainties includes: PDF uncer-  
 707 tainties,  $\alpha_s$  uncertainty, QCD scale uncertainty and uncertainty on the  $H \rightarrow \gamma\gamma$  branching  
 708 fraction (used to derive the Higgs Dalitz Decays cross-section). The values for these theoretical  
 709 uncertainties are taken from the Higgs Combination Group [44] and also from [68].
- 710 • **Luminosity:** an uncertainty value of 2.5% is used on the integrated luminosity of the data  
 711 samples, as recommended by CMS [32].
- 712 • **Pileup:** the total inelastic cross section of 69.2 *mb* for minimum bias is varied by  $\pm 4.6\%$   
 713 and the analysis is ran with the extreme values. The systematic uncertainty quoted is the  
 714 maximum difference in the yields with respect to nominal value, as recommended by CMS.
- 715 • **Trigger efficiency:** the analysis is ran applying  $\pm 1\sigma$  on the Trigger Efficiency Scale factors  
 716 (ref. section 4.5.1). The systematic uncertainty quoted is the maximum difference in the  
 717 yields with respect to nominal value.
- 718 • **Photon Identification:** the analysis is ran applying  $\pm 1\sigma$  on the scale factors (ref. section  
 719 4.5.3) for the Photon MVA ID and the Electron Veto. The systematic uncertainty quoted is  
 720 the maximum difference in the yields with respect to nominal value.
- 721 • **Muon Identification/Isolation:** the analysis is ran applying  $\pm 1\sigma$  on the scale factors (ref.  
 722 section 4.5.2). The systematic uncertainty quoted is the maximum difference in the yields  
 723 with respect to nominal value.
- 724 •  **$\Upsilon$  Polarization:** the analysis is ran applying with the extremes scenarios of the  $\Upsilon$  polariza-  
 725 tion (Transverse and Longitudinal Polarization), applying different reweightings to the signal  
 726 samples (ref. section 4.2). The systematic uncertainty quoted is the maximum difference in

727 the yields with respect to nominal (Unpolarized) yield. This procedure is applied only for the  
 728 Z decay. For the Higgs decay, the only polarization considered is the transverse polarization.

729 The effect of all systematic uncertainties in the signal and peaking background yields are summa-  
 730 rized on table 4.8, for the Z decay and table 4.9, for the Higgs decay. Clearly, the main contribution  
 731 to the systematics uncertainties on the yields is Polarization of the  $\Upsilon(nS)$  (only for the Z decay),  
 732 around 15%.

### 733 4.10.2 Uncertainties that affect the signal fits

734 Smearing and scaling corrections are applied on simulated events since the resolution of Monte  
 735 Carlo is better than that on data and the detector might not catch all the possible differences in  
 736 the detector performance, with respecto the real data observation. They need to be estimated and  
 737 included on the systematics. The corrections are:

- 738 • **Muon Momentum Scale and Resolution:** extracted by running the analysis with different  
 739 setups of the official CMS Muon scaling and smearing package [69]. The deviations, with  
 740 respect to the default correction are summed in quadrature. Once the nominal parameters  
 741 (mean or sigma) are obtained, the default corrections are shifted by  $\pm 1\sigma$  and the fits are  
 742 re-done, with the parameters of interest free to float and all others fixed. The systematic  
 743 uncertainty quoted is the maximum difference of the parameter with respect to nominal value.

- 744 • **Photon Energy Scale and Resolution:** extracted by running the analysis with different  
 745 sets of corrections, provided by the CMS <sup>8</sup>. Once the nominal mean is obtained, the sets  
 746 are changed and the fits are re-done, with the mean free to float and all others parameters  
 747 fixed. The corrections are shifted by  $\pm 1\sigma$  on each source of systematics (following standard  
 748 CMS recommendations). The quoted as systematic uncertainty is the quadrature sum of the  
 749 maximum deviation within each set.

750 The effective systematic uncertainty associated with the scale and resolution are the quadrature  
 751 sum of the muon and photon contributions. The effect of all systematic uncertainties in the Signal  
 752 fits are summarized on table 4.10, for the Z and Higgs decay.

---

<sup>8</sup>CMS has not published, yet, a paper on the Run2 performance of the Photon reconstruction (This document is under internal review process.). Just as a reference, we cite the Run1 paper [70].

Source	Uncertainty			
	Signal		Peaking Background	
	$Z \rightarrow \Upsilon(1S)\gamma$	$Z \rightarrow \Upsilon(2S)\gamma$	$Z \rightarrow \Upsilon(3S)\gamma$	$Z \rightarrow \mu\mu\gamma_{FSR}$
Integrated luminosity				
All Categories	2.5%			
SM Z boson $\sigma$ (scale)				
All Categories	3.5%		5.0%	
SM Z boson $\sigma$ (PDF + $\alpha_s$ )				
All Categories	1.73%		5.0%	
Pileup Reweighting				
Inclusive	0.65%	0.68%	0.71%	0.62%
EB High R9	1.01%	1.1%	1.04%	1.06%
EB Low R9	0.17%	0.08%	0.13%	0.11%
EE 1.07%	0.98%	1.26%	0.78%	
Trigger				
Inclusive	4.45%	4.46%	4.49%	4.71%
EB High R9	3.5%	3.5%	3.52%	3.71%
EB Low R9	3.55%	3.54%	3.58%	3.72%
EE 7.52%	7.58%	7.56%	8.13%	
Muon Identification				
Inclusive	4.82%	4.81%	4.8%	4.52%
EB High R9	4.45%	4.45%	4.44%	4.2%
EB Low R9	4.65%	4.62%	4.63%	4.32%
EE 5.75%	5.75%	5.74%	5.44%	
Photon Identification				
Inclusive	1.1%	1.1%	1.09%	1.09%
EB High R9	1.1%	1.09%	1.09%	1.11%
EB Low R9	1.1%	1.1%	1.09%	1.08%
EE 1.1%	1.1%	1.1%	1.09%	
Electron Veto				
Inclusive	1.02%	1.02%	1.02%	1.03%
EB High R9	1.2%	1.2%	1.2%	1.2%
EB Low R9	1.2%	1.2%	1.2%	1.2%
EE 0.45%	0.45%	0.45%	0.45%	
Polarization				
Inclusive	15.36%	14.78%	14.84%	-
EB High R9	15.6%	14.88%	14.87%	-
EB Low R9	15.01%	14.31%	14.4%	-
EE 15.39%	15.27%	15.39%	-	

Table 4.8: A summary table of systematic uncertainties in the Z boson decaying in  $\Upsilon(1S, 2S, 3S) + \gamma$ , affecting the final yields of the MC samples.

Source	Uncertainty			
	Signal			Peaking Background
	$H \rightarrow \Upsilon(1S)\gamma$	$H \rightarrow \Upsilon(2S)\gamma$	$H \rightarrow \Upsilon(3S)\gamma$	$H \rightarrow \gamma\gamma^*$
Integrated luminosity	2.5%			
SM Higgs $\sigma$ (scale)	$+4.6\% / -6.7\%$			
SM Higgs $\sigma$ (PDF + $\alpha_s$ )	3.2%			
SM BR $H \rightarrow \gamma\gamma^*$	-			6.0%
Pileup Reweighting	0.61%	0.68%	0.56%	0.9%
Trigger	5.61%	5.47%	5.5%	6.12%
Muon Identification	4.39%	4.36%	4.34%	4.33%
Photon Identification	1.21%	1.22%	1.22%	1.2%
Electron Veto	1.04%	1.04%	1.04%	1.04%

Table 4.9: A summary table of systematic uncertainties in the Higgs boson decaying in  $\Upsilon(1S, 2S, 3S) + \gamma$ , affecting the final yields of the MC samples.

		Z $\rightarrow \Upsilon(nS) + \gamma$			H $\rightarrow \Upsilon(nS) + \gamma$	
		Inclusive	EB High R9	EB Low R9	EE	Inclusive
<b>Mean - Scale</b>						
$\Upsilon(1S)$	Muon Unc.	0.06%	0.05%	0.06%	0.11%	0.11%
	Photon Unc.	0.21%	0.13%	0.19%	0.26%	0.28%
	<b>Total Unc.</b>	0.22%	0.14%	0.2%	0.28%	0.3%
<b>Sigma - Resolution</b>						
$\Upsilon(1S)$	Muon Unc.	1.12%	0.84%	1.55%	1.14%	2.62%
	Photon Unc.	2.14%	2.48%	1.95%	2.79%	4.27%
	<b>Total Unc.</b>	2.42%	2.61%	2.49%	3.01%	5.01%
<b>Mean - Scale</b>						
$\Upsilon(2S)$	Muon Unc.	0.07%	0.05%	0.06%	0.13%	0.1%
	Photon Unc.	0.25%	0.11%	0.2%	0.19%	0.26%
	<b>Total Unc.</b>	0.26%	0.12%	0.21%	0.23%	0.28%
<b>Sigma - Resolution</b>						
$\Upsilon(2S)$	Muon Unc.	1.21%	1.54%	2.65%	1.66%	1.02%
	Photon Unc.	1.85%	2.67%	3.56%	3.6%	6.6%
	<b>Total Unc.</b>	2.21%	3.08%	4.44%	3.97%	6.68%
<b>Mean - Scale</b>						
$\Upsilon(3S)$	Muon Unc.	0.06%	0.06%	0.06%	0.09%	0.09%
	Photon Unc.	0.22%	0.14%	0.25%	0.17%	0.23%
	<b>Total Unc.</b>	0.23%	0.15%	0.26%	0.19%	0.25%
<b>Sigma - Resolution</b>						
$\Upsilon(3S)$	Muon Unc.	1.78%	2.38%	2.1%	2.25%	3.46%
	Photon Unc.	2.51%	4.14%	2.23%	4.08%	5.48%
	<b>Total Unc.</b>	3.08%	4.77%	3.07%	4.66%	6.48%

Table 4.10: A summary table of systematic uncertainties in the Z (H) decaying in  $\Upsilon(1S, 2S, 3S) + \gamma$ , affecting the signal fits.

## 753 4.11 Modeling Cross checks

754 In order to test the applicability of the statistical (signal and background) modeling proposed  
 755 in this study, a cross-check procedure is performed by generating a set of pseudo-experiments  
 756 (toys datasets) based on the signal plus background model, for each decay channel ( $H/Z \rightarrow$   
 757  $\Upsilon(1S, 2S, 3S, ) + \gamma$ ) with some signal injected.

758 The procedure consists of resample from the signal plus background a number of events, including  
 759 some extra (injected signal). The amount of injected signal is controlled by the  $\mu_{true}$  variable, where  
 760  $\mu_{true} = X$  means inject  $X$  times the expected signal.

761 Once generated, the toy dataset is refitted to the signal plus background model and the signal  
 762 strength ( $\mu_{fit}$ ) and its error  $\sigma_{fit}$  are extracted. This procedures is repeated 10000 times and only  
 763 for the inclusive category. Figures 4.66, 4.65, 4.68 and 4.67 show examples of those fits for the  
 764 Higgs and Z decay.

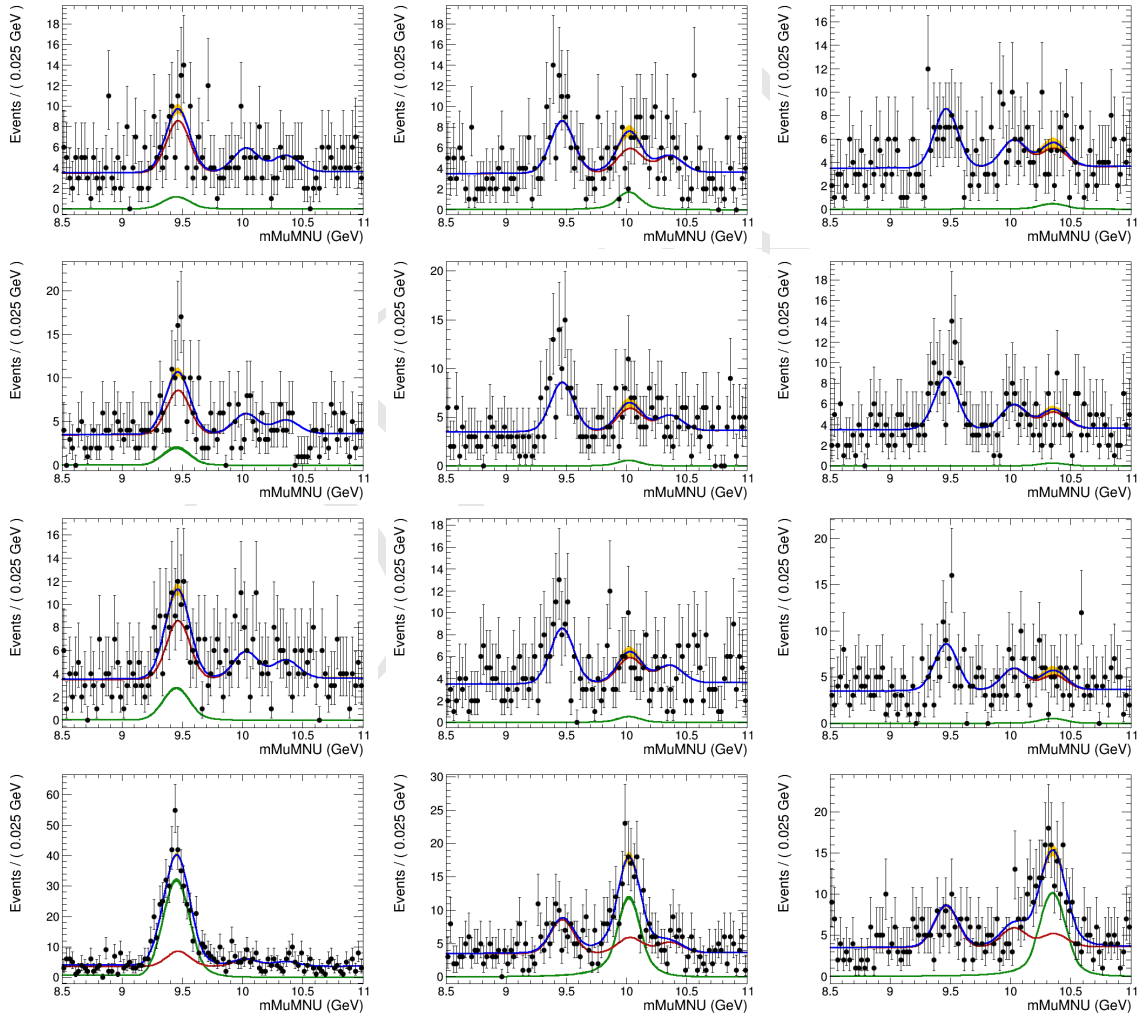


Figure 4.65: Examples of the toy datasets fit ( $M_{\mu\mu}$ ), for the Z decay analysis, after the toy dataset refit, for 1S, 2S and 3S (left to right), with  $\mu_{true}$  equals to 20, 50, 100, 1000 (top to bottom). The red lines corresponds to the background model (B), the green lines to signal model (S), the blue lines to the total (S+B) and the dots is the toy dataset.

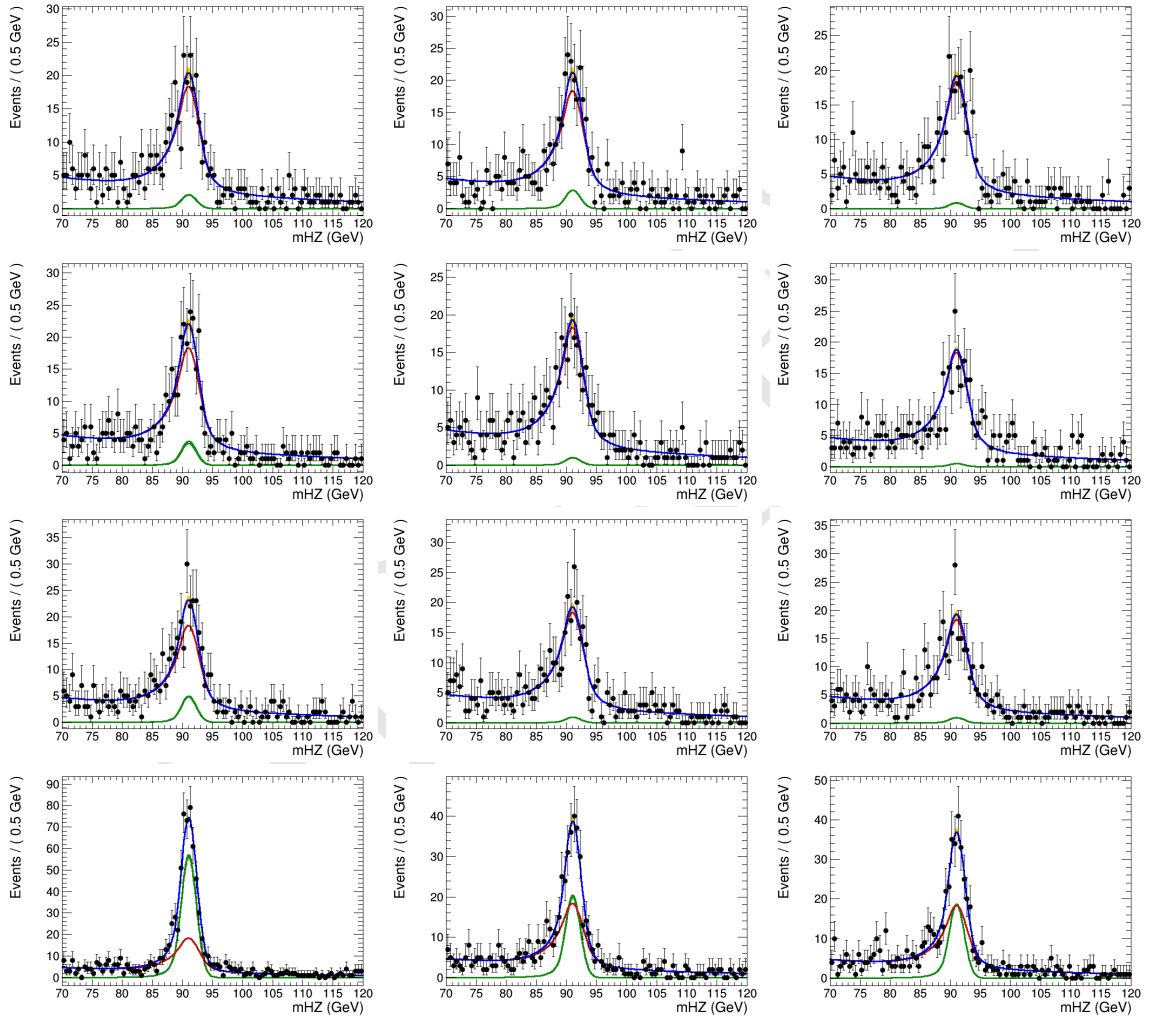


Figure 4.66: Examples of the toy datasets fit ( $M_{\mu\mu\gamma}$ ), for the Z decay analysis, after the toy dataset refit, for 1S, 2S and 3S (left to right), with  $\mu_{true}$  equals to 20, 50, 100, 1000 (top to bottom). The red lines corresponds to the background model (B), the green lines to signal model (S), the blue lines to the total (S+B) and the dots is the toy dataset.

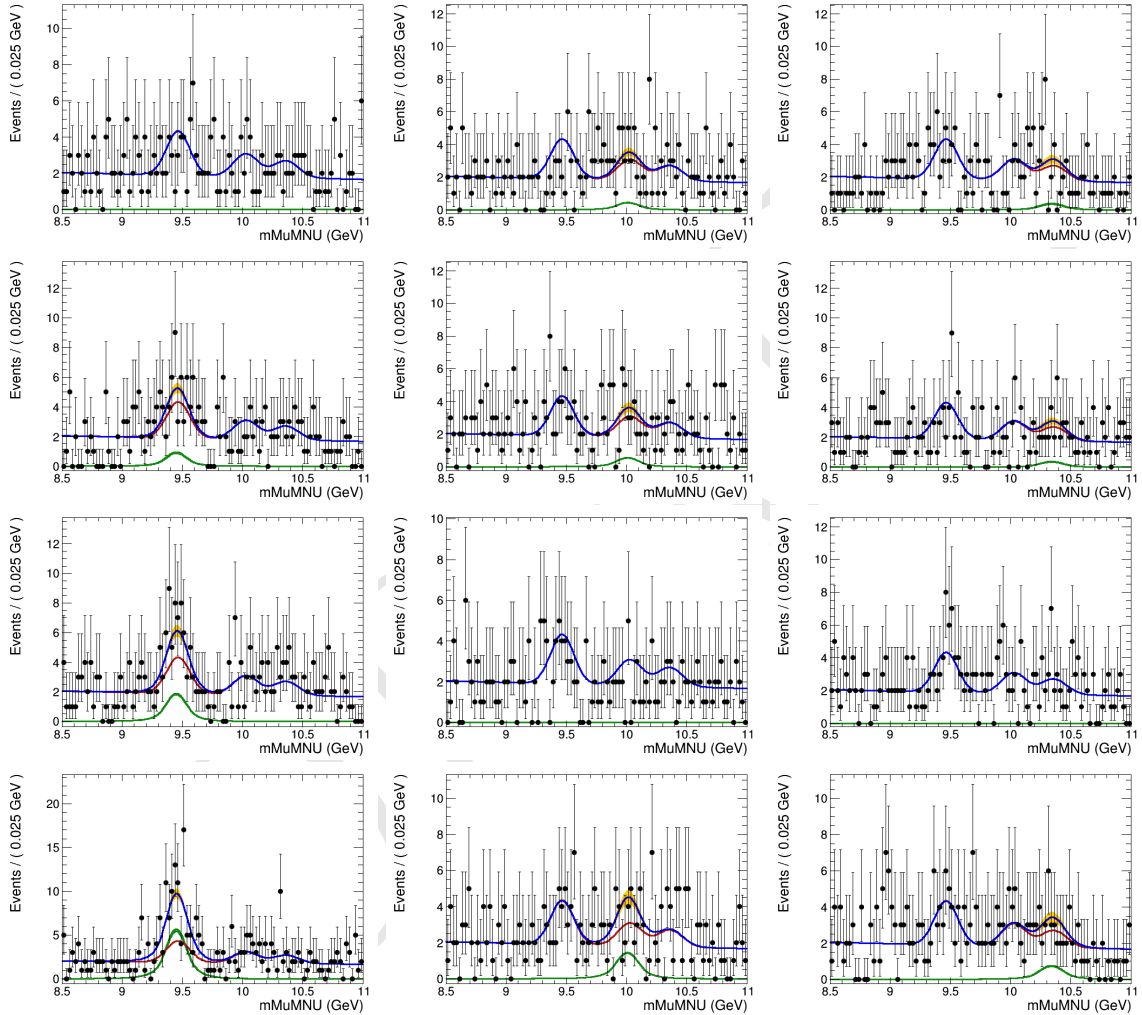


Figure 4.67: Examples of the toy datasets fit ( $M_{\mu\mu}$ ), for the Higgs decay analysis, after the toy dataset refit, for 1S, 2S and 3S (left to right), with  $\mu_{true}$  equals to 100000, 200000, 300000, 1000000 (top to bottom). The red lines corresponds to the background model (B), the green lines to signal model (S), the blue lines to the total (S+B) and the dots is the toy dataset.

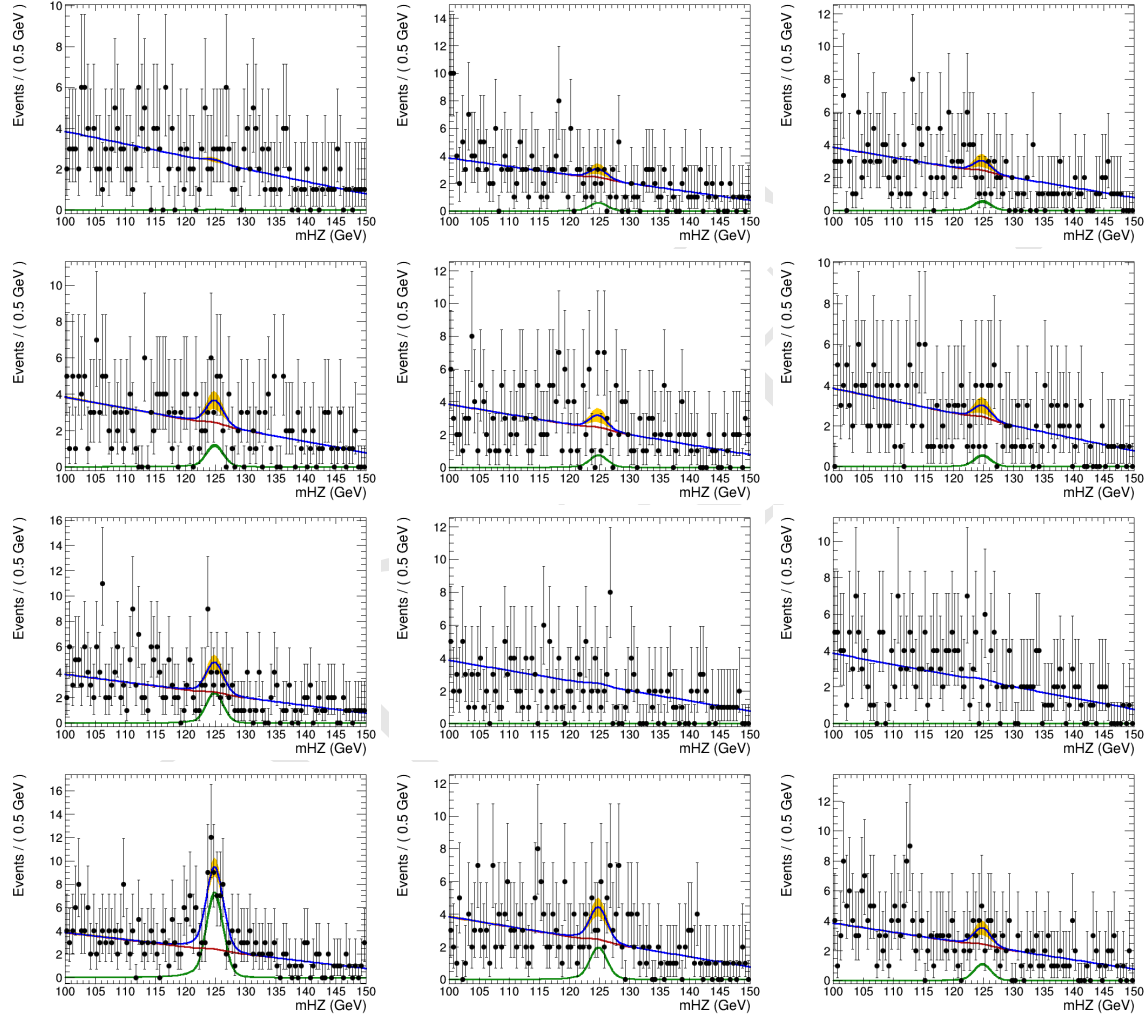


Figure 4.68: Examples of the toy datasets fit ( $M_{\mu\mu\gamma}$ ), for the Higgs decay analysis, after the toy dataset refit, for 1S, 2S and 3S (left to right), with  $\mu_{true}$  equals to 100000, 200000, 300000, 1000000 (top to bottom). The red lines corresponds to the background model (B), the green lines to signal model (S), the blue lines to the total (S+B) and the dots is the toy dataset.

It is expected that the pulls distribution for the fitted signal strength ( $\frac{\mu_{fit} - \mu_{true}}{\sigma_{fit}}$ ) should follow a Gaussian distribution centered in 0 and with  $\sigma$  around 1. Figures 4.69 and 4.70 present those pulls distributions for the Z and Higgs decays, respectively.

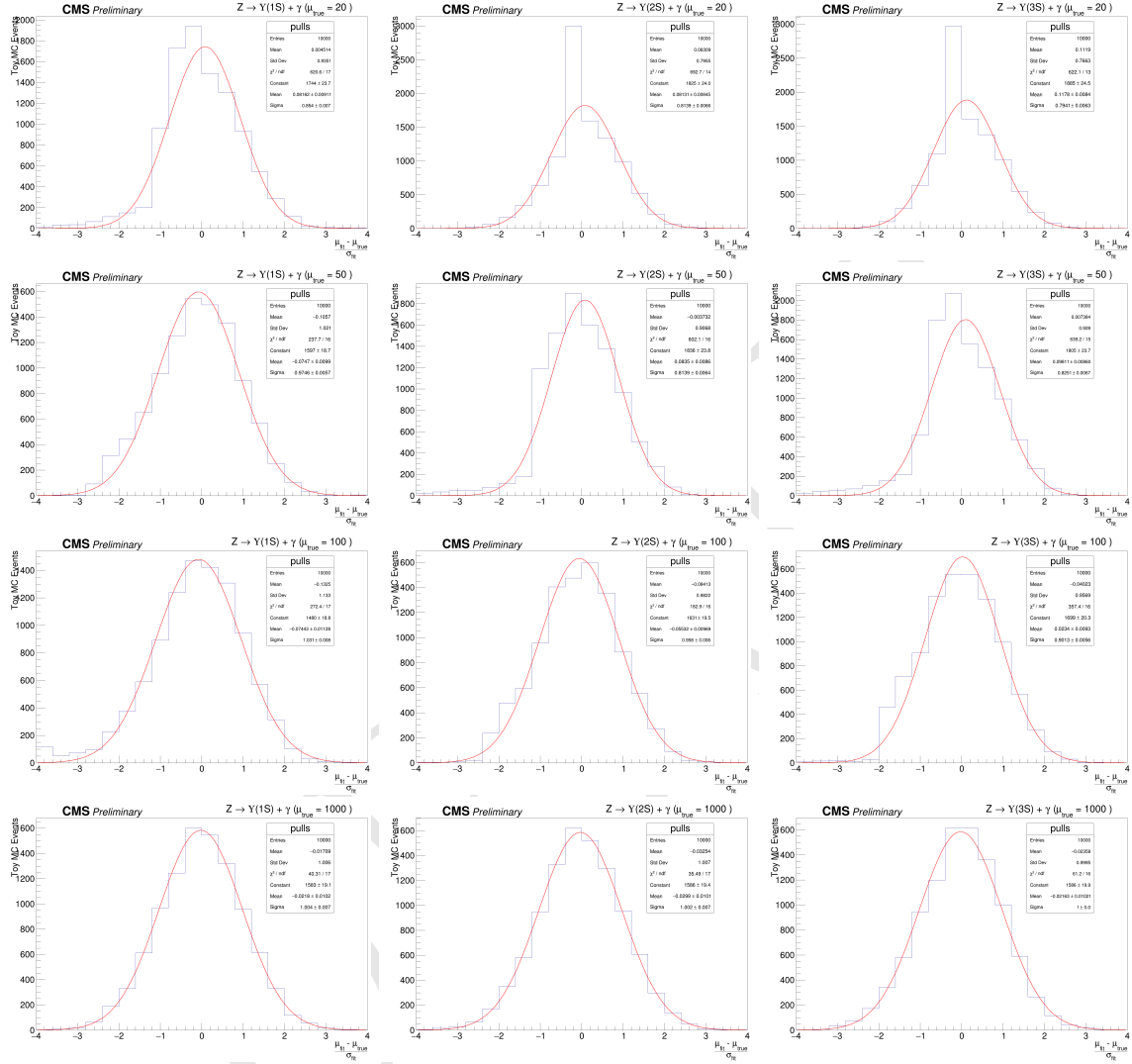


Figure 4.69: Distribution of pulls ( $\frac{\mu_{fit} - \mu_{true}}{\sigma_{fit}}$ ), for the Z decay analysis, after the toy dataset refit, for 1S, 2S and 3S (left to right), with  $\mu_{true}$  equals to 20, 50, 100, 1000 (top to bottom).

As a general conclusion on this cross check, as long as the toy MC generation is able to inject enough signal to be fit, the final modeling of this analysis is able to recover a Gaussian pulls distribution. This, of course, depends on the  $\Upsilon$  state to be considered. For the Z decay, between  $\mu_{true} = 50$  and  $\mu_{true} = 100$  (around a hundred of events passing full selection), while for the Higgs decay, it is needed only a few events after full selection, even though it means hundreds of thousands times the expected signal, since the very small cross sections for the decay, as shown in Table 4.1.

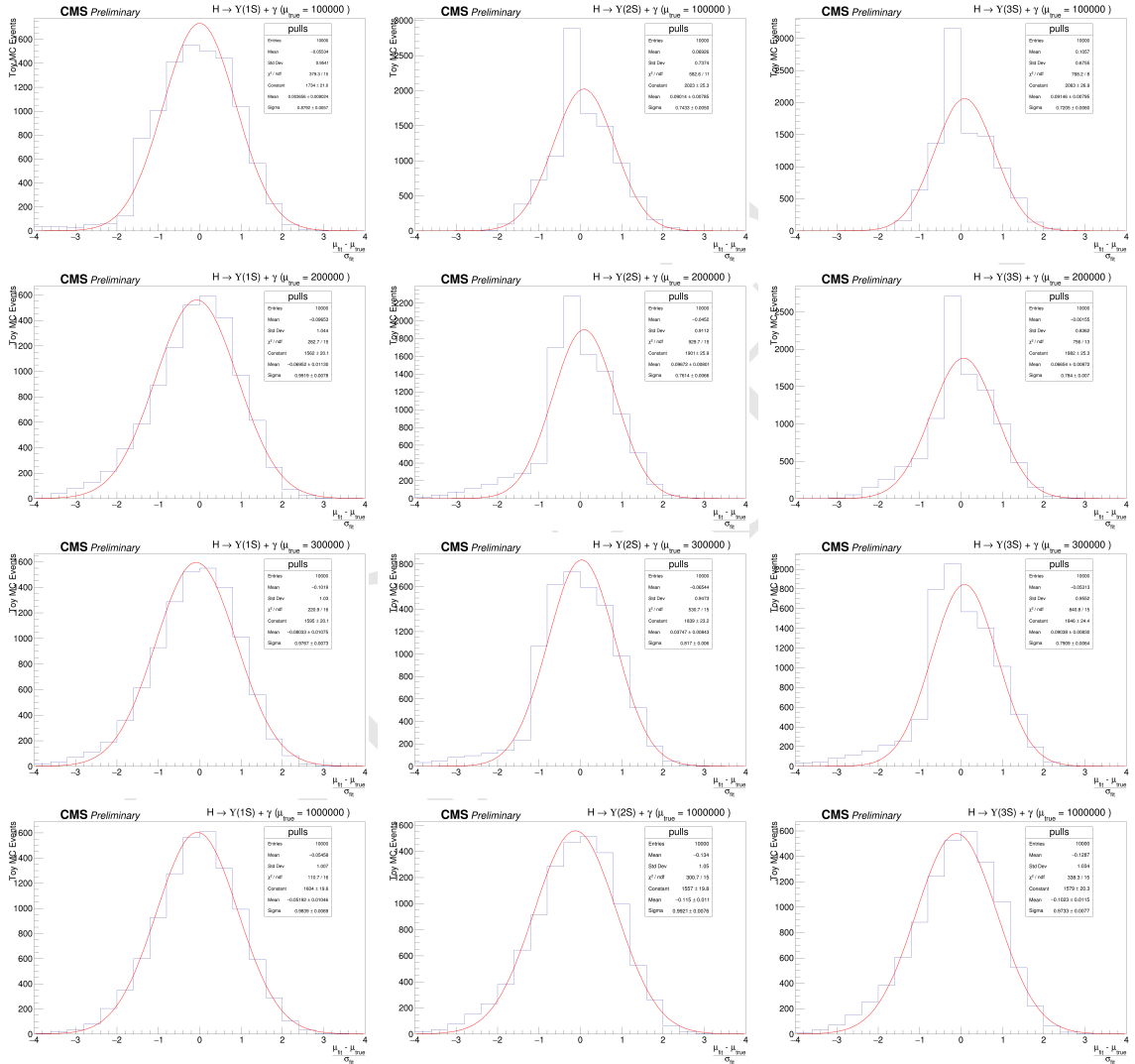


Figure 4.70: Distribution of pulls ( $\frac{\mu_{fit} - \mu_{true}}{\sigma_{fit}}$ ), for the Higgs decay analysis, after the toy dataset refit, for 1S, 2S and 3S (left to right), with  $\mu_{true}$  equals to 100000, 200000, 300000, 1000000 (top to bottom).

DRAFT

## 774 5 Results and conclusion

775 A two-dimensional (2D) unbinned maximum-likelihood fit to the  $m_{\mu^+\mu^-\gamma}$  and  $m_{\mu^+\mu^-}$  distri-  
 776 butions was used to compare the data with background and signal predictions. Search has been  
 777 performed for a SM Higgs and Z boson decaying into a  $\Upsilon(1S, 2S, 3S)\gamma$ , with  $\Upsilon(1S, 2S, 3S)$  subse-  
 778 quently decaying into  $\mu^+\mu^-$  using data obtained from  $35.9 \text{ fb}^{-1}$  of  $pp$  collisions at  $\sqrt{s} = 13 \text{ TeV}$ .

779 Since no excess has been observed above the background, the  $CL_s$  formalism is applied, in order  
 780 to establish an upper limit in the branching fractions for each channel.

### 781 5.1 The $CL_s$ formalism for upper limits setting at CMS

782 The  $CL_s$  formalism [71] consist in a modified frequentist approach to obtain an upper limit for a  
 783 certain parameter of a model, with respect to the data, when there is no significant excess that could  
 784 justify an observation. It is based on the profile-likelihood-ratio test statistic [72] and asymptotic  
 785 approximations [73]. It is a standard upper limit setting procedure for the LHC experiments [74].

786 When searching for non-observed phenomena, it is often usual to derive the results as a function  
 787 of the signal strength modifier  $\mu$ , which is a free parameter of the full model (signal + background).  
 788 It can be define such as, the expectation value for the number of events in a bin <sup>1</sup> is:

$$E[n] = \mu s + b, \quad (5.1)$$

789 where,  $s$  and  $b$  are the expected number of signal e background events, respectively.

790 The Neyman–Pearson lemma [72] states the likelihood ratio is the optimal test between a null  
 791 hypothesis and an alternative one (i.e. background-only and signal-plus-background models). On  
 792 top on this, one could build a likelihood ratio test as:

$$q(\mu) = -2\ln \left( \frac{\mathcal{L}(\text{data}|\mu s + b)}{\mathcal{L}(\text{data}|b)} \right), \quad (5.2)$$

793 where the denominator and numerator defines the likelihoods for the background-only and signal-  
 794 plus-background models, respectively. The was the hypothesis test used by LEP and Tevatron  
 795 experiments (the former one, with some modifications to include the nuisances effects).

796 With these two models, i.e. their *pdfs*, one can throw toy MC events in order to construct a  
 797 distribution of  $q(\mu)$ , namely  $f(q(\mu)|\mu)$ . The *p*-value of  $f(q(\mu)|\mu)$ , as below, can be used to chose  
 798 between each model.

$$p_\mu = \int_{q(\mu)_\text{data}}^{\infty} f(q(\mu)|\mu) dq(\mu), \quad (5.3)$$

---

<sup>1</sup>A set of common analysis criteria.

799 where  $q(\mu)_{\text{data}}$  is the observed value of  $q(\mu)$  on data, for a given  $\mu$ .

800 If  $p_\mu$  is less than  $\alpha$  (usually 0.05 or 0.1) the background-only model can be excluded in favor of  
 801 the signal-plus-background model. For the propose of a confidence interval estimation, the argument  
 802 can be reversed and one could look for all the values of  $\mu$  that would not be excluded with Confidence  
 803 Level (CL)  $1 - \alpha$ .

804 The problem with this definition is that, when the expected signal strength is very small, e.g.  
 805 a invariant mass distribution in the TeV scale, the null hypothesis and the alternative one are  
 806 almost indistinguishable. In this situation, a downward fluctuation of the background might lead  
 807 us to exclude the alternative hypothesis (signal) in a region of low experimental sensitivity region.  
 808 Putting in number, if we expect 50 background events and 2 signal events, but we observe 40 events,  
 809 the signal would be easily excluded.

810 In order to take this effect into account, a modified frequentist approach for upper limits setting,  
 811 the  $CL_s$  was proposed during the Higgs search era at LEP. Lets start by considering a profile  
 812 likelihood ratio [75] as below:

$$\lambda(\mu) = \frac{\mathcal{L}(\text{data}|\mu, \hat{\theta})}{\mathcal{L}(\text{data}|\hat{\mu}, \hat{\theta})}, \quad (5.4)$$

813 where,  $\mathcal{L}(\text{data}|\mu, \hat{\theta})$  is the profile likelihood function.

814 Defining  $\mu$  and the investigated signal strength,  $\hat{\theta}$  is the nuisances that maximizes the likelihood  
 815 for a given  $\mu$  (fixed) while  $\hat{\mu}$  and  $\hat{\theta}$  are the signal strength and nuisances that, overall, maximizes  
 816 the likelihood. The advantage of the

817 CMS and ATLAS have a common set of statistical guidelines [76] to ensure the compatibility of  
 818 the published results. Following these recommendations, the statistics test based on 5.4 is:

$$\tilde{q}_\mu = -2\ln[\lambda(\mu)], \text{ with } 0 \leq \hat{\mu} \leq \mu. \quad (5.5)$$

819 The left side restriction ( $0 \leq \hat{\mu}$ ) ensure us the proper physical interpretation of  $\mu$  as a positive  
 820 define signal strength, i.e., the observation a process would, for a given bin, increase the number  
 821 of events. The right side restriction  $\hat{\mu} \leq \mu$  secure the interpretation of  $\tilde{q}_\mu$ 's  $p$ -value as a one-sided  
 822 confidence interval. This is required for a upper limit definition.

823 The advantage of using the profile likelihood ratio is that, even though it takes into account the  
 824 effect of nuisances in the likelihood, it is possible to prove that, with the use of Wilk's Theorem [58],  
 825 that a statistic test defined as  $\tilde{q}_\mu$ , asymptotically follows a chi-square distribution with one degree  
 826 of freedom (the signal strength) [73]. Thus,  $\tilde{q}_\mu$  is said to be approximately independent of any  
 827 nuisance and allow a fast computation of its  $p$ -value without the need of toy MC strategies (which  
 828 can computationally demanding, depending on the complexity of the models), event though this is  
 829 not the standard CMS/ATLAS recommendation.

830 Based on  $\tilde{q}_\mu$ , defined at 5.5, one should compute the  $\tilde{q}_\mu^{\text{obs}}$ ,also the  $\hat{\theta}_\mu^{\text{obs}}$  and  $\hat{\theta}_{\mu=0}^{\text{obs}}$ , which cor-  
 831 responds to the observed value of  $\tilde{q}_\mu$  on data, the maximum likelihood estimator for the nuisances  
 832 assuming some signal strength  $\mu$  and assuming a background-only model, respectively. Then, the  
 833 distributions of  $f(\tilde{q}_\mu|\mu, \hat{\theta}_\mu^{\text{obs}})$  and  $f(\tilde{q}_\mu|\mu = 0, \hat{\theta}_{\mu=0}^{\text{obs}})$  are generated tossing pseudo-random toy MC.  
 834 Figure 5.1 presents an example of these two distributions.

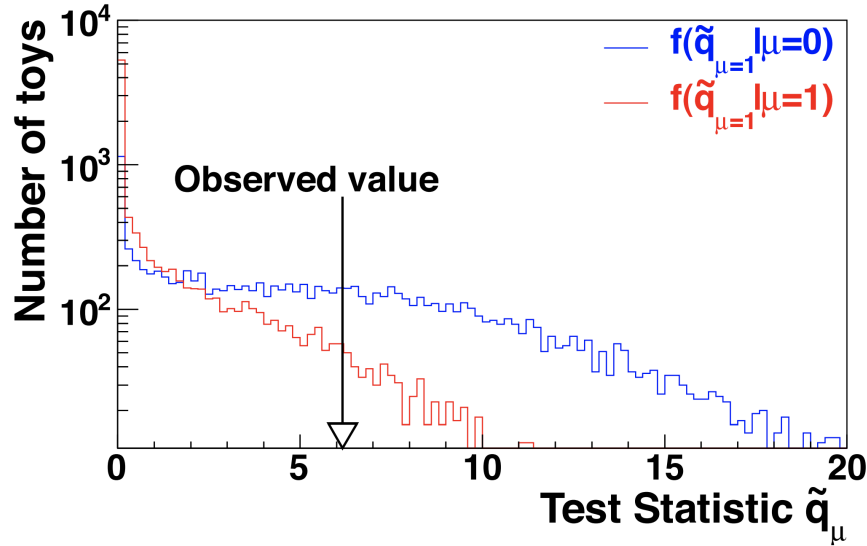


Figure 5.1: Example of  $f(\tilde{q}_\mu | \mu, \hat{\theta}_\mu^{\text{obs}})$   $f(\tilde{q}_\mu | \mu = 0, \hat{\theta}_{\mu=0}^{\text{obs}})$  distributions generated with toy MC.  
Source: [76].

835 The  $CL_s$  value is defined as:

$$CL_s = \frac{p_{s+b}(\mu)}{1 - p_b}, \quad (5.6)$$

836 where:

$$p_{s+b}(\mu) = \int_{\tilde{q}_\mu^{\text{obs}}}^{\infty} f(\tilde{q}_\mu | \mu, \hat{\theta}_\mu^{\text{obs}}) d\tilde{q}_\mu \quad (5.7)$$

and

$$p_b = \int_{-\infty}^{\tilde{q}_\mu^{\text{obs}}} f(\tilde{q}_\mu | \mu = 0, \hat{\theta}_{\mu=0}^{\text{obs}}) d\tilde{q}_\mu \quad (5.8)$$

837 Scanning different values of  $\mu$ , within  $0 \leq \hat{\mu} \leq \mu$ , one would exclude the ones which  $CL_s < \alpha$ .  
838 CMS and ATLAS recommends a CL level  $(1 - \alpha)$  of 95%.

839 The main advantage of the  $CL_s$  approach is that the presence of the denominator  $1 - p_b$  in 5.6  
840 penalizes the exclusion of regions in which the experiment is no sensitive. Figure 5.2 helps to  
841 illustrate this. One can notice that a small value of  $p_{s+b}$  (yellow area) is balanced by large value  
842 of  $p_b$  (green area). When the experimental sensitivity is higher, the two distributions tend to be  
843 far away from each other. Thus leading to a smaller compensation factor ( $p_b$ ) and enhancing the  
844 chance of a exclusive  $CL_s$  value.

## 845 5.2 Branching fraction upper limits

846 The result are summarized on table 5.1.

847 The observed(expected) exclusion limit at 95% confidence level on the  $\mathcal{B}(Z \rightarrow \Upsilon(1S, 2S, 3S)\gamma) =$   
848  $2.9, 2.7, 1.4 (1.6^{+0.8}, 2.0^{+1.0}, 1.8^{+1.0}) \times 10^{-6}$ , and on the  $\mathcal{B}(H \rightarrow \Upsilon(1S, 2S, 3S)\gamma) = 6.9, 7.4, 5.8$   
849  $(7.3^{+4.0}, 8.1^{+4.6}, 6.8^{+3.9}) \times 10^{-4}$ .

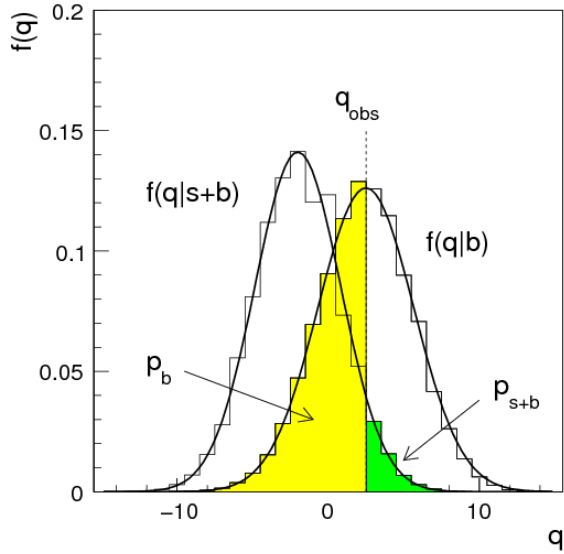


Figure 5.2: Example of  $f(\tilde{q}_\mu|\mu, \hat{\theta}_\mu^{\text{obs}})$   $f(\tilde{q}_\mu|\mu = 0, \hat{\theta}_{\mu=0}^{\text{obs}})$  distributions generated with toy MC. In the figure,  $q$  must be read as  $\tilde{q}$ . The green area shows the  $p_{s+b}$  defined in 5.7, while the yellow one shows  $p_b$  defined in 5.8. Source: [73].

As stated before, this analysis was done, for the Z decay, taking into account a mutually excludent categorization of events, based on the reconstructed photon properties ( $\eta_{SC}$  and R9 value), as described in section 4.7.

At table 5.2 we present the results obtained when there is no categorization of events (Inclusive category).

It is worth to remember that the categorization takes places only for the Z decay. For the Higgs decay, no categorization is imposed.

By taking, or not, into account any categorization, the numbers presented in both tables (5.1 and 5.2), are compatible within themselves and with the results published by the ATLAS collaboration [77].

95% C.L. Upper Limit			
	$\mathcal{B}(Z \rightarrow \Upsilon\gamma) [\times 10^{-6}]$		
	$\Upsilon(1S)$	$\Upsilon(2S)$	$\Upsilon(3S)$
Expected	$1.6^{+0.8}_{-0.5}$	$2.0^{+1.0}_{-0.6}$	$1.8^{+1.0}_{-0.6}$
Observed	2.9	2.7	1.4
SM Prediction [ $\times 10^{-8}$ ]	4.8	2.4	1.9
	$\mathcal{B}(H \rightarrow \Upsilon\gamma) [\times 10^{-4}]$		
	$\Upsilon(1S)$	$\Upsilon(2S)$	$\Upsilon(3S)$
Expected	$7.3^{+4.0}_{-2.4}$	$8.1^{+4.6}_{-2.8}$	$6.8^{+3.9}_{-2.3}$
Observed	6.9	7.4	5.8
SM Prediction [ $\times 10^{-9}$ ]	5.2	1.4	0.9

Table 5.1: Summary table for the limits on branching ratio of  $Z \rightarrow \Upsilon(1S, 2S, 3S)\gamma$  and  $H \rightarrow \Upsilon(1S, 2S, 3S)\gamma$  decays.

95% C.L. Upper Limit - $\mathcal{B}(Z \rightarrow \Upsilon\gamma) [\times 10^{-6}]$			
	without categorization		
	$\Upsilon(1S)$	$\Upsilon(2S)$	$\Upsilon(3S)$
Expected	$1.7^{+0.9}_{-0.5}$	$2.1^{+1.1}_{-0.7}$	$1.9^{+1.0}_{-0.6}$
Observed	2.6	2.3	1.2
	with categorization		
	$\Upsilon(1S)$	$\Upsilon(2S)$	$\Upsilon(3S)$
Expected	$1.6^{+0.8}_{-0.5}$	$2.0^{+1.0}_{-0.6}$	$1.8^{+1.0}_{-0.6}$
Observed	2.9	2.7	1.4

Table 5.2: Summary table for the limits on branching ratio of  $Z \rightarrow \Upsilon(1S, 2S, 3S)\gamma$ , for the two possible categorization scenarios.

DRAFT

# 860 6 CMS Resistive Plate Chambers - RPC

861 In the course of this PhD study, there were a lot of opportunities to work for the RPC project, in  
 862 the context of the CMS Collaboration. The main activities consists of shifts for the RPC operation  
 863 and data certification, upgrade and maintenance of the online software, R&D activities for the RPC  
 864 upgrade and detector maintenance during the LHC Long Shutdown 2 (2019 to 2020).

865 In this chapter, it is presented a summary of the Resistive Plate Chamber technology and the  
 866 contributions to the RPC project at CMS.

## 867 6.1 Resistive Plate Chambers

868 The seminal paper on the Resistive Plate Chamber (RPC) technology was presented by R.  
 869 Santonico and R. Cardarelli, in which they described a "dc operated particle detector (...) whose  
 870 constituent elements are two parallel electrode Bakelite plates between" [78]. The key idea behind  
 871 the RPC, with respect to other similar gaseous detectors, is the use of two resistive plates as anode  
 872 an cathode, which makes possible to have a small localized region of dead time, achieving very good  
 873 time resolution.

874 The working principle for RPCs relies on the idea that a ionizing particle crossing the detector,  
 875 tend to interact with the gap between the two plates (filled with some specific gas mixture) and  
 876 form a ionizing cascade process, in which the produced charged particle are driven by the strong  
 877 uniform electrical field produced by the two plates.

878 The gas mixture is a key component of a RPC. Even though the first RPCs were produced  
 879 with a mixture of argon and butane, nowadays RPCs use a mixture of gases that would enhance an  
 880 ionization caused by the incident particle and quench secondary (background) effects.

881 Another feature of the RPCs is its construction simplicity and low cost. This allow the use RPC  
 882 to cover larger at a reasonable cost.

883 A extensive review of the RPC technology and its application can be found at [79].

### 884 6.1.1 Principles and operation modes

885 The core of a RPC chamber is a gap made with two parallel high resistivity plates, separated  
 886 by some regular distance (typically millimeters), filled with with a proper gas mixture and under  
 887 appropriate high voltage (HV) applied on the plates (electrodes, from here on). When a ionizing  
 888 particle crosses the gap, there is a high enough chance the the particle will interact with the gas  
 889 and produce a newly created positive ion and a electron. This pair will travel in opposite directions,  
 890 according to the electric field from the electrodes. During this process, the electron will gain kinetic  
 891 energy and inelasticly interact with other neighboring atoms/molecules, creating excitations in their  
 892 energy levels and, potentially, also ionizing them. The secondary ionization electrons will also follow

the same curse, creating an **Avalanche** of positive and negative particle/ions traveling towards the electrodes. This process is proportional to the applied electric field. Figure 6.1 illustrates the avalanche production.

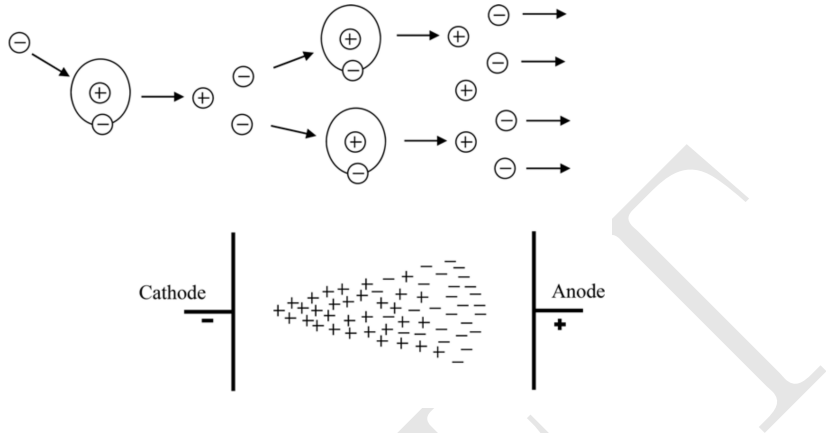


Figure 6.1: The Avalanche production process inside a RPC gap. (Top) The initial process and the secondary electron/ion generation. (Bottom) The overall charge distribution of an Avalanche between the electrodes. Source: [80].

The number of particles composing the avalanche can be expressed as (assuming constant pressure) [80]:

$$n_e = n_0 e^{\alpha d} = n_0 A, \quad (6.1)$$

where  $n_0$  is the number of initial electrons initiating the avalanche,  $A$  is the *gas gain*, or *multiplication factor* and  $d$  is the distance since the avalanche creation. This is also known as Townsend theory for discharges and  $\alpha$  is the first Townsend coefficient.

When the positive ions bunch reaches the cathode, under certain conditions (if the first ionization energy of the ion is greater than the work function of the cathode), the recombination of the ion with the electrode material might release electrons which will also follow the electric field. The relative probability (with respect to the primary electron emission) of this emission to happen ( $\gamma_+$ ) is called the second Townsend coefficient.

$$n_+ = n_0 A \gamma_+. \quad (6.2)$$

Another process which can occur is the secondary photoelectron production, described by a similar equation as above:  $n_{pe} = n_0 A \gamma_{ph}$ . This production is mostly related to de-excitation of molecules and atoms in vicinity of the avalanche. The produced photons might initiate new ionization process.

As an alternative to the Townsend theory, Raether, Meek, and Loeb, proposed the *streamer-leader theory* [81]. This theory is valid when there is a high enough concentration of ions produced. This critical value is called Raether limit.

$$n_0 A > 10^8 \text{ electrons} \quad (6.3)$$

In this limit, the electric field created by the space distribution is high enough to be same order of the external field. In the vicinity of the head (or tail) of the avalanche the field gets disturbed and intensified. The intensification of the field enhances the ionization effect and give rise to secondary avalanches (photoelectrons). The intensified field also makes the photoelectrons produced travel towards the head (positive ions). Their antiquation generates more UV radiation and more secondary avalanches. This whole process is called **Streamer**. If no quenching is imposed, the streamer might evolve to a spark, fully discharging on the electrodes. If the concentration of electrons is high enough, the avalanche tail (electrons) might also give rise to a streamer (namely, negative streamer). Figure 6.2 illustrates the different subprocess related to streamer production.

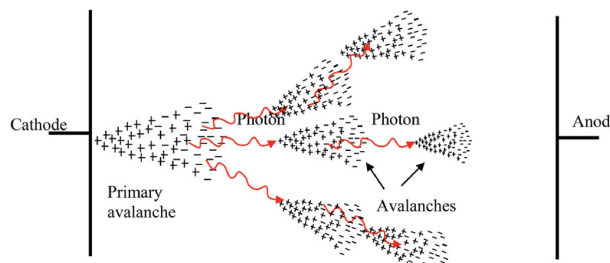


Figure 6.2: Streamer formation process. The distorted electric field around the high positive charge concentration enhances the ionization process, initiating secondary avalanches. Source: [80].

A RPC where most of the charge multiplication process happens in the form of a streamer is said to be working in **Streamer Mode**. The advantage of the streamer mode is the high induced charge which is easily caught by non-sensitive readout electronics. On the other hand, the streamer mode, because of its highly associated charge, will have an impact in the rate capability of the detector (the local dead time will be higher).

Because of the high background environment of LHC, the CMS RPC operates in **Avalanche Mode**, where de discharge is highly quenched and very well localized. On the other hand, a very sensitive readout electronics is required to cope with the high rate demanded.

A good review of electrical discharge on gases can be found at [80].

## 6.2 CMS Resistive Plate Chambers

At CMS, the Resistive Plate Chamber are installed in both the barrel and endcap region, forming a redundant system with the DT (barrel) and CSC (endcap). As described in the CMS Muon Technical Design Report (Muon-TDR) [82], the RPC are composed of 423 Endcap chambers and 633 barrel chambers. Figure 6.3 presents a picture of the CMS RPCs installed on station RE+4 of the Endcap.

Each chamber consists of two gas gaps (double gap), 2 mm tick each, made of Bakelite (phenolic resin) with bulk resistivity of  $10^{10} - 10^{11} \Omega m$ . The choice of the bulk resistivity of the electrode has high impact on the rate capability of the detector.

Each gap has its external surface is coated with a thin layer of graphite paint, which acts as conductive material, distributing the applied high-voltage (HV). On top of the graphite a PET

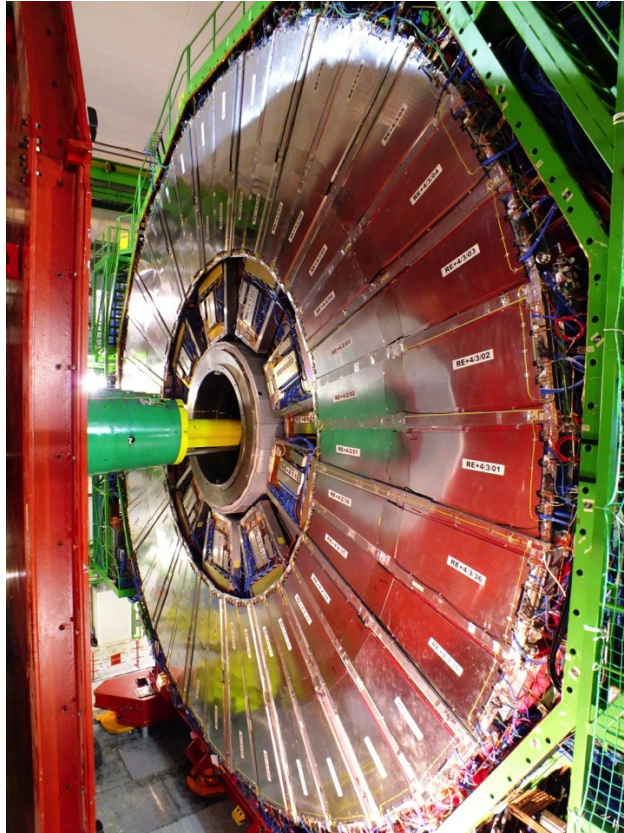


Figure 6.3: RPC chamber on installed on station RE+4 of CMS Endcap. Source: [83].

942 film is used for isolation. A sheet of copper strips is sandwiched between the gaps. Everything is  
943 wrapped in aluminum case.

944 The double gap configuration increases the efficiency of the chamber, since the signal is picked  
945 up from the OR combination of the two gaps. A chamber with only one gap working, loses around  
946 15% of efficiency, even though, this can be recovered by increasing the HV applied during operation  
947 mode (working point - WP).

948 A characteristic that differentiate the CMS RPC from previous RPC application in HEP is  
949 the operation mode. A RPC at CMS, operates in avalanche mode, while previous experiments used  
950 the streamer mode. Both modes are related to the applied HV, in commitment with the strength of  
951 the generated signal, and are capable of generate a well localized signal, which can be picked up by  
952 the readout electronics, but the avalanche mode offer a higher rate capability around  $1 \text{ kHz/cm}^2$ ,  
953 while the streamer mode goes up to  $100 \text{ Hz/cm}^2$ . The high rate capability is a key factor in order  
954 to cope with requirements of the LHC luminosity, specially in the high background regions.

955 Besides the rate capability, the key factors that driven the CMS RPC design were: high effi-  
956 ciency ( $> 95\%$ ), low cluster size ( $> 2$ ) for better spatial resolution (this reflects in the momentum  
957 resolution) and good timing in order to do the readout of the signal within the 25 ns of a LHC  
958 bunch cross (BX) and provide it to the CMS trigger system. These requirements have implications  
959 in the choice of material, dimensions, electronics and gas mixture.

960 In the barrel, along the radial direction, there are 4 muon layers (called stations), MB1 to MB4.  
961 MB1 and MB2 is composed of a DT chamber sandwiched between two RPC chambers (RB1 and

RB2) with rectangular shape. The stations MB3 and MB4 have only one RPC (RB3 and RB4) are composed by two RPC chambers (named - and + chambers with the increase of  $\phi$ ) attached to one DT chamber, except in sector 9 and 11, where there is only one RPC. RE4, sector 10 is a special case, since it is composed of four chambers (-, -, + and ++). These stations are replicated along the z direction in five different wheels of the CMS (W-2, W-1, W0, W+1 and W+2) and in twelve azimuthally distributed sectors (S1 to S12). Figure 6.4 show the different barrel stations and wheel.

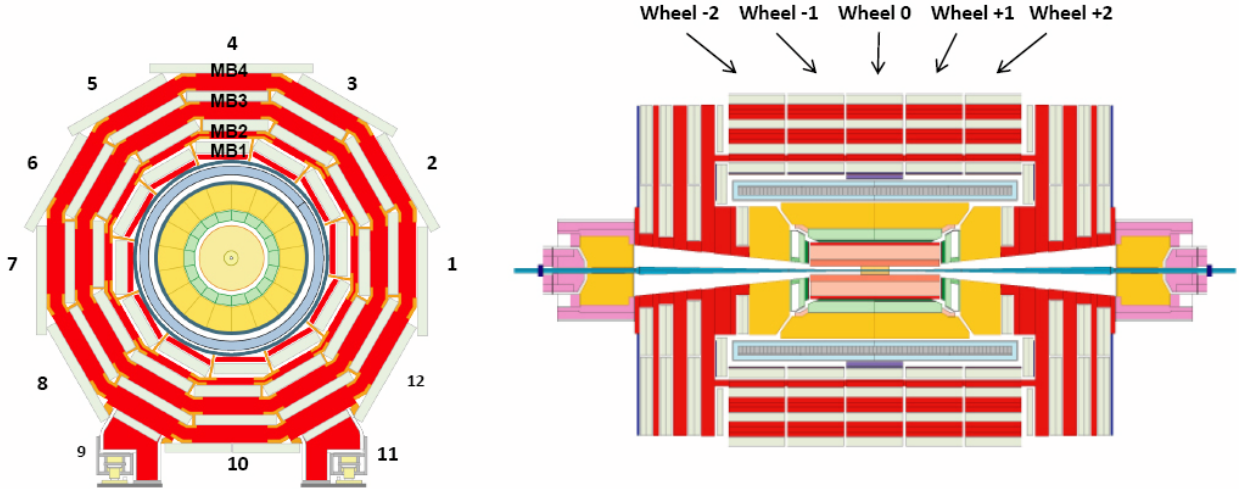


Figure 6.4: R- $\phi$  (left) and R-Z (right) projections of the barrel Muon System.

In the endcap, the RPC chambers have a trapezoidal shape and are distributed in four disks (or stations) each side ( $RE \pm 4$ ,  $RE \pm 3$ ,  $RE \pm 2$ ,  $RE \pm 1$ ), each one with 72 chambers. CMS split up its disks in 3 rings, along the radial direction, and 36 sector in the azimuthal angle. RPCs are present in the two outer rings ( $R2$  and  $R3$ ), in all 36 sectors. The  $RE \pm 4$  are special cases, since these chambers were installed only in 2014, a design choice was made the mechanically attached  $R2$  and  $R3$  chambers, each sector, in what is called, a super-module. Figure 6.5 show the different endcap disks.

The length of the strips is chosen, for both barrel and endcap, in such a way to control the area of each strip, in order to reduce the fake muons, due to random coincidence. This has to do with the time-of-flight and signal propagation along the strip. In the barrel, each chamber readout is divided in two regions (rolls), called forward and backward (along increasing  $|\eta|$ ) <sup>1</sup>. In the endcap, the strips are divided in 3 regions, called partitions A, B and C (from inside the detector to outside).

The gas mixture used in the CMS RPCs is composed by C2H2F4 (Freon R-134a, tetrafluoroethane), C4H10 (isobutane), SF6 (sulphur hexafluoride) (95.2 : 4.5 : 0.3 ratio) and with controlled humidity of 40% at 20-22 °C. The Freon is used to enhance the ionization and charge multiplication that characterizes the avalanche, while the isobutane is introduced for quenching proposes, in order to reduce the secondary ionizations that could lead to formation of streamers and the SF6 is used to reduce the electron background. The choice of Freon over other gases, i.e. argon-based and helium-based, was motivated by previous studies [84, 85].

<sup>1</sup>Some chamber are divided in three rolls, forward, middle and backward, for trigger propose.

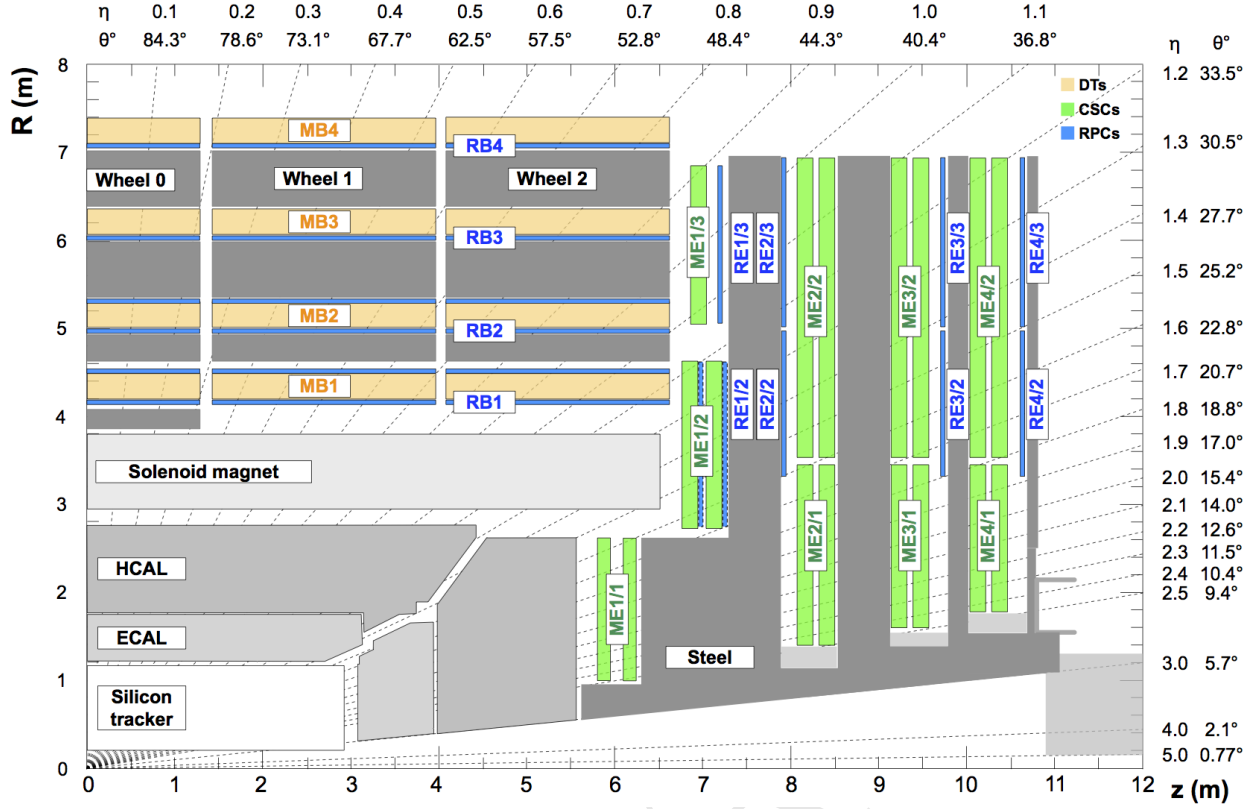


Figure 6.5: R-Z projections of the endcap Muon System (positive Z side). This is the same configuration for the 36  $\phi$  sectors.

Since its R&D, the RPC have shown good performance over aging. This is even historical over previous RPC experiments [86–92]. Even the most recent studies of aging, taking into account future LHC conditions (High-Luminosity LHC - HL-LHC) plus a safety margin of 3 times the expected background ( $600 \text{ Hz/cm}^2$ ) have shown good aging hardness [93].

### 6.2.1 Performance

The RPCs, for the CMS experiment, contribute mainly with triggering inputs, due to its very good time resolution. The important parameters which are monitored to evaluate the RPC performance are the efficiency and cluster size. The former is related to the ratio of the registered hits over the number of muons that passed through the chamber, while the latter one is the number adjacent strip (minimal readout unit) that were fired (activated) per hit. Figures 6.6 and 6.7 present the historical distribution of efficiency and cluster size as a function of the integrated luminosity collect during Run2.

In general, the RPC system operates with efficiency above 95% and cluster size smaller than 3 (a good parameter established during the design phase). The importance of the efficiency is a less complicated concept to catch, on the other hand, the cluster size might not be so straight forward. The optimal regime of RPCs operation at CMS is the avalanche mode, in which the electrical discharge is constrained in a millimeter level size region. Another operation mode is the streamer mode, in which the initial discharge might trigger secondary ones, e.g. by the emission of

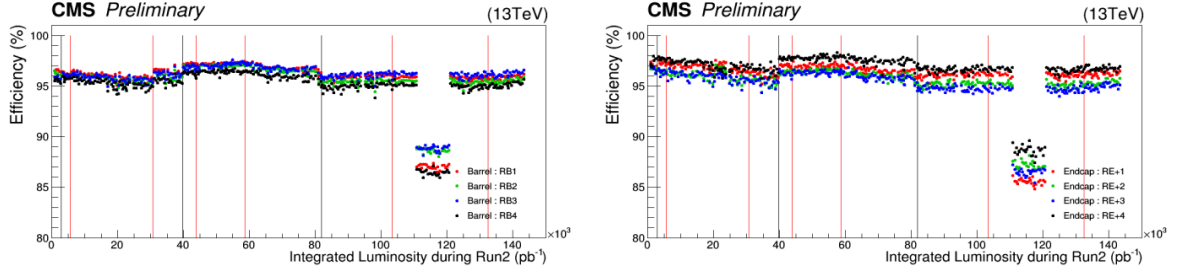


Figure 6.6: RPC efficiencies (per chamber) over Run2 Integrated Luminosity for Barrel (left) and Endcap (right). Red lines indicates technical stops (TS) while grey ones indicates Year-End-Technical stops (YETS). The drop in the efficiency around  $110 \text{ pb}^{-1}$  is related to a known operation mistake. Source: [94].

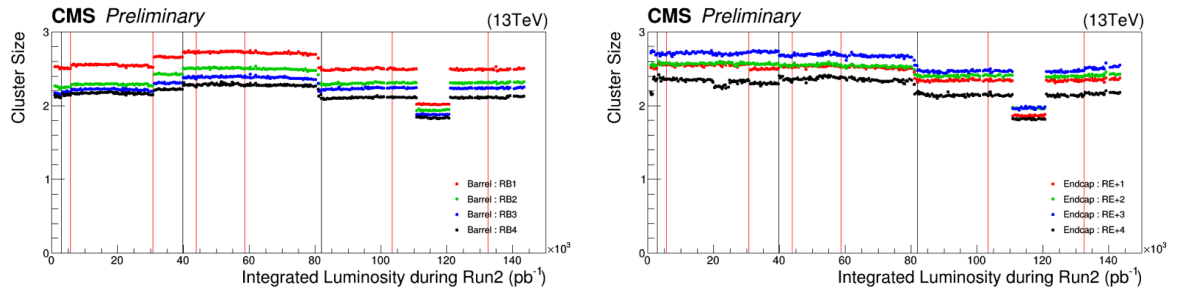


Figure 6.7: RPC cluster size (CLS - per chamber) over Run2 Integrated Luminosity for Barrel (left) and Endcap (right). Red lines indicates technical stops (TS) while grey ones indicates Year-End-Technical stops (YETS). The drop in the cluster size around  $110 \text{ pb}^{-1}$  is related to a known operation mistake. Source: [94].

unquenched photons. A streamer discharge is capable of fire neighbor strips, increasing the cluster size. Operating in avalanche mode is fundamental to keep the RPCs capable of dealing with the high background environment of CMS.

To keep the mean cluster size under control ( $< 3$ ) is important to guarantees enough spatial resolution for the measurements (the geometrical position of a hit is the midpoint of the cluster) and ensures that the system has enough rate capability to operate, since a RPC with a high sensitive front-end electronics (necessary for the avalanche mode operation) could be degraded by pileup of dead time on many channels, including electronics noise, streamers, darks counts and other sources of background.

A third important parameter to be measured and controlled in a RPC system, under the LHC conditions, is the current due to the high voltage applied. This current is known to be proportional to the total charge released in each electrical discharges and to the hit rate on the chamber. The voltage applied is divided, as in a series circuit, between the electrodes and the gap. At increasing background, the current also increases and, since the applied voltage is constant, the voltage across the gap is reduced in favor of the voltage across the electrodes. This reduction of effective voltage on the gas, might have an impact on its gain, imposing a reduction on the detector sensitivity.

Figure 6.8 presents the ohmic currents <sup>2</sup> in different regions of the detector, from 16<sup>th</sup> of April, 2018 to 2<sup>nd</sup> of December, 2018. It is clear how the stations subjected to higher background ( $RE \pm 4 - 40 \text{ Hz/cm}^2$ ) are subjected to a degrading factor that increases with the luminosity (background rate) and decreases when the detector is powered off. This effect is supposed to be related with the Hydrogen Fluoride (HF) production inside the gap, due to the electrical discharges. HF is a conductivity molecule, which can potentially attach to the internal surface of the gap, reducing the overall resistivity. The HF production can be controlled by properly tuning the gas flow as a function of the background that the chamber is subjected. HF concentration can also lead to permanent degradation of the gap, due to its chemical properties. Keeping the currents levels as low as possible is important for aging proposes.

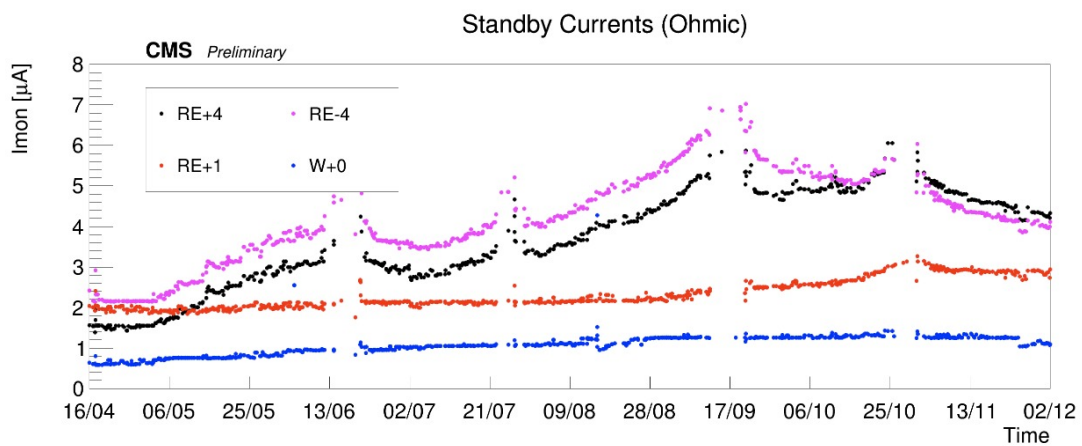


Figure 6.8: Ohmic current history of W+0, RE+1, RE+4 and RE-4. The blank regions, from time to time, corresponds to technical stops (TS), when the detector is off. Source: [94].

<sup>2</sup>Current at 6500 V, which is below the typical working point of a CMS RPC (around 9500 V). In this region, no charge multiplication effect take place and chamber current is governed only by Ohm's Law.

1031 A review of the RPC performance during Run2 can be found at [94].

## 1032 6.3 Contribution to the CMS RPC project

1033 During the course of this study, a head collaboration of our research group and the CMS RPC  
1034 project was established. Many contributions were given to the project as part of the graduation as a  
1035 experimental particle physicist, with focus on getting acquaintance with a subsystem technology and  
1036 give a meaningful collaboration to the detector operation. Those are considered by the community  
1037 important steps on the student graduation.

1038 Below it is described the contributions given to the CMS RPC project.

### 1039 6.3.1 RPC Operation - Shifts and Data Certification

1040 The first activities done for the CMS RPC project were shifts for data certification of data taken.  
1041 This certification is done by specialized people for different CMS subsystems and physics objects  
1042 groups <sup>3</sup>.

1043 This certification is done in order to ensure the quality of the date recorded based on the well  
1044 functionality of each system during the data taking and the reconstruction of the physics objects in  
1045 the expected matter. A certain collection of data (run) is said certificate when all subsystems and  
1046 object experts agrees on this.

1047 Figure 6.9 shows, as an example of the luminosity delivered by the LHC, recorded one by CMS  
1048 and the certified (validated), from the 22nd of April, 2016 to the 27th of October, 2016. Only  
1049 certified data is available for physics analysis.

1050 Shifts are a continuous weekly activity (specially during the data taking period), performed in  
1051 a weekly basis, in order to ensure the availability of certified data, as soon as possible.

## 1052 6.4 RPC Online Software

1053 On what concerns the Online Software (OS) of the CMS RPC system, the main contribution  
1054 given was the upgrade of the Trigger Supervisor libraries.

1055 The Trigger Supervisor is a web-based software, which run over the xDAQ backend and provides,  
1056 through a modules organized in a tree system, called cells, a standard interface for the operation and  
1057 monitoring of different system at CMS. In principle only systems which contribute directly to the  
1058 L1 trigger should have a Trigger Supervisor implementation. This was the case for the RPC during  
1059 the Run1. Since Run2, RPC contributes to the trigger indirectly, by providing data to the muon  
1060 processors (CPPF, OMTF and TwinMux). The Trigger Supervisor implementation is a legacy from  
1061 that period.

1062 Each subsystem is responsible for its own implementation of the Trigger Supervisor, based on  
1063 the functionalities that it wants to have (requirements). The xDAQ [96] is a middleware, developed  
1064 by CERN and widely used at CMS, as a tool for control and monitoring of data acquisition system

<sup>3</sup>Groups of reconstruction and performance experts for different high-level reconstructed objects from CMS, i.e. muons, taus, jets/MET, electrons/photons

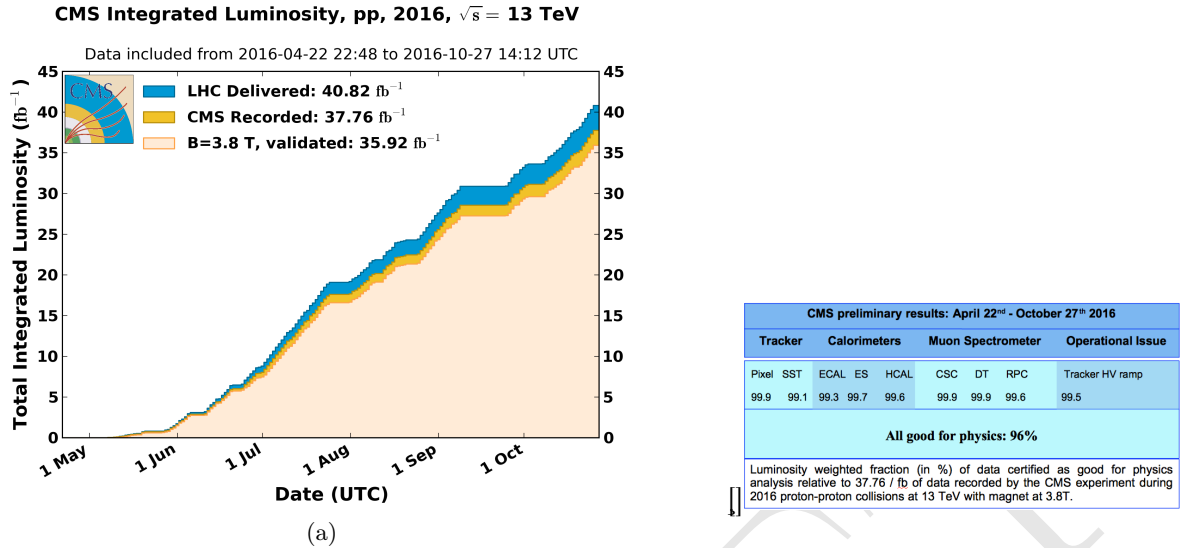


Figure 6.9: (a) Luminosity delivered by the LHC, recorded one by CMS and the certified (validated), from the 22nd of April, 2016 to the 27th of October, 2016. (b) Efficiency of the certification process for each subsystem, from the 22nd of April, 2016 to the 27th of October, 2016. Total CMS efficiency is above 90%. [95]

1065 in a distributed environment. It is capable of providing a software layer for direct access of hardware  
1066 functionalities and monitoring.

1067 The upgrade made (figure 6.10), consists in upgrade the higher level of the RPC online software.  
1068 In summary, up to 2017, the online software, was using Scientific Linux 6 as operational system,  
1069 which executed xDAQ 12, in turn, servers as backend for Trigger Supervisor 2. A upgrade of  
1070 the operational system to Centos 7, demanded the upgrade to xDAQ 14. On top of that, Trigger  
1071 Supervisor 2 would not work and had to be updated to Trigger Supervisor 5 in order to be functional  
1072 in 2018.

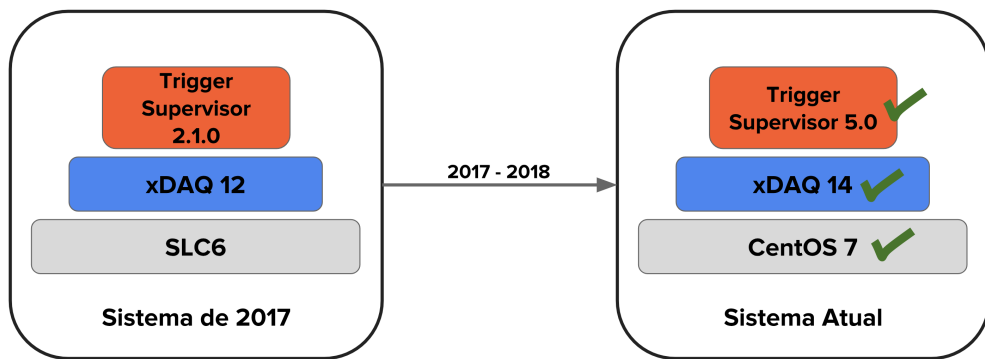


Figure 6.10: Upgrade of the RPC online software.

1073 Between versions 2 and 5 of Trigger Supervisor, part of the source-code had to be reworked,  
1074 keep the majority of the code structures. Most of the changes were made in the front-end of the  
1075 system. The standard JavaScript library Dojo [97], used in version2, was deprecated in favor of  
1076 Google's Polymer[98]. The main reason for this change was to isolate C++ code from HTML, which

1077 was impossible with Dojo. This implied to rewrite all the screen of the RPC Trigger Supervisor  
 1078 implementation, as in figure 6.11.

1079 The upgrade was done in time to ensure the control and operation of the RPC for 2018 data  
 1080 taking.

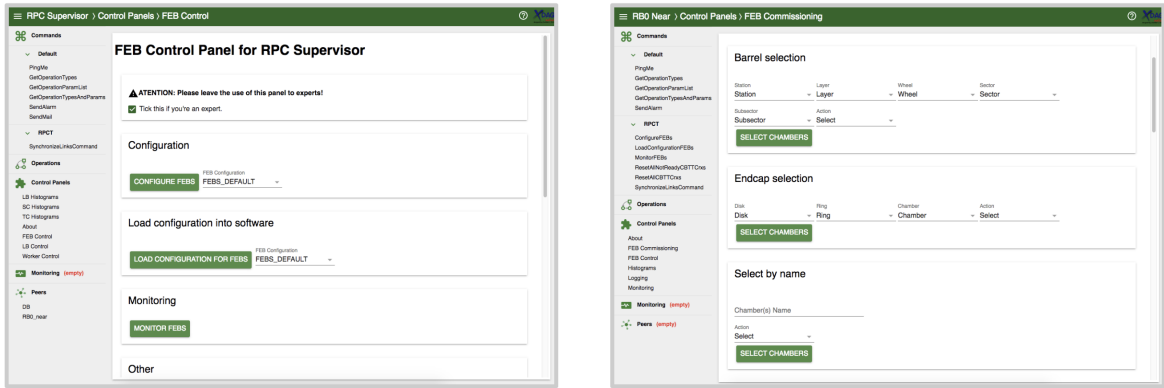


Figure 6.11: Example of the updated screens, using Trigger Supervisor 5.

#### 1081 6.4.1 iRPC R&D

1082 For the next 4 year of CMS activities it is foreseen the upgrade of the the Muon Systems [82].  
 1083 These upgrades are planed in order to extend the pseudorapidity coverage ( $\eta$ ) and to guarantee the  
 1084 operation conditions of the present system in the HL-LHC (High Luminosity LHC) era. The RPC  
 1085 (Resistive Plate Chambers) [82] subsystem, it will have maintenance of the present chambers and  
 1086 installation of new chambers in the region of  $|\eta| < 1,8$  para  $|\eta| < 2,4$  [99]. These new chambers  
 1087 (iRPC) will be added in the most internal part of the muon spectrometer, RE3/1 e RE4/1, as in  
 1088 Figure 6.12.

1089 Even thought this region is covered by the CSC detectors CSC (Cathode Strip Chambers), there  
 1090 are some loss of efficiency due the the system geometry. The installation of additional chambers will  
 1091 mitigate this problem and potentially increase the global efficiency of the muon system. The new  
 1092 chamber, called iRPC (*improved RPC*), will be different them the present one. For a luminosity of  
 1093  $5 \times 10^{34} cm^{-2}s^{-1}$  the neutrons, photons, electrons and positrons background in the high  $|\eta|$  region  
 1094 is expected to be around  $700 Hz/cm^2$  (for the chambers in RE3-4/1). Applying a safety factor  
 1095 of 3, the new chambers should support up to  $2 Hz/cm^2$  of gamma radiation and still keep more  
 1096 than 95% of efficiency. Studies indicate, so far, that the use of High Pressure Laminates (HPL) for  
 1097 the double gap chambers is the most suitable choice. In order to reduce the aging and increase the  
 1098 rate capability, the electrodes and the gap size should be reduced in comparison with the present  
 1099 system.

1100 One of the challenges for the R&D of the iRPC chambers is measuring the their performance  
 1101 in a high radiation environment, as the one for HL-LHC. For this, the CMS RPC project uses the  
 1102 Gamma Irradiation Facility (GIF++) [100], at CERN. The GIF++ is located at the H4 beam line  
 1103 in EHN1 providing high energy charged particle beams (mainly muon beam with momentum up to  
 1104 100 GeV/c), combined with a 14 TBq 137-Cesium source. In the GIFF++ it is possible to achieve

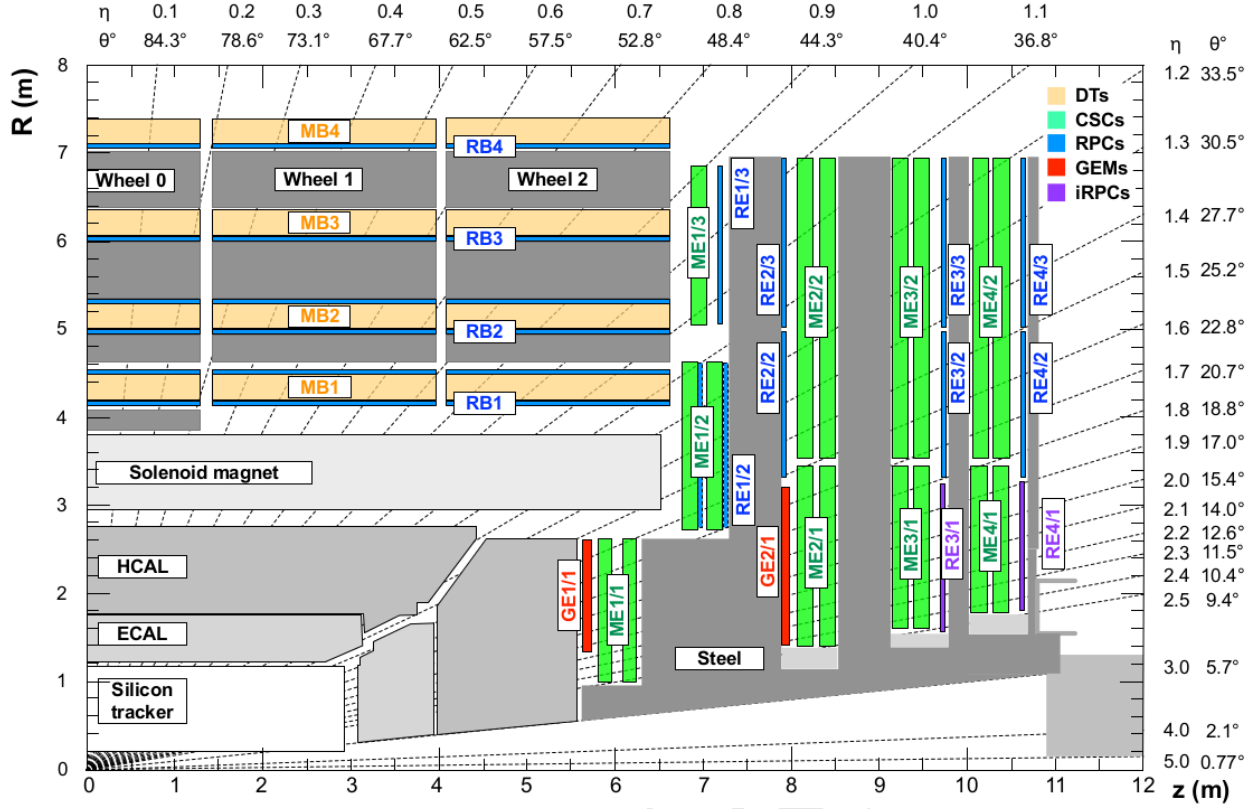


Figure 6.12:  $\eta$  projection of the Muon System subdetectors. In purple, is labeled the iRPCs to be installed during the CMS upgrade.

the HL-LHC total dose in a much reasonable amount of time. With the shutdown of LHC, the muon beam source is also off and will stay like this for 3 years. This means that the only muon sources for studies in GIF++ are cosmic muons.

In order to create a trigger system for iRPC R&D, the usual procedure is to use scintillators, on the top and on the bottom of the chamber. This is effective, but in a high gamma radiation environment, scintillators can be very sensitive which could lead to an undesirable amount of fake triggers which can degrade the measurements. Also, if one wants to covers a large area with scintillators, this can be expensive and they will not provide any means of tracking to measuring not only the global, but also the local chamber performance.

To provide a solution, the CMS RPC got in agreement with the LHCb [101] Muon Project to use their Multiwire Proportional Chambers (MWPC) [102], which were removed from LHCb, to be replaced by new chambers, and use them as trigger and/or tracking system at GIF++. This chambers, by design, have relatively low gamma sensitivity, already have some 1-dimensional resolution ( $O(cm)$ ) and, the biggest advantage, with respect to any other gaseous particle detector option: LHCb has hundreds of vacant chambers. Any other detector would have to be build.

Not going in details of the MWPC technology nor the LHCb chamber construction [103], these chambers have a total active area of  $968 \times 200 \text{ mm}^2$  divided 2 layers (top and bottom) of 24 wire pads ( $40 \times 200 \text{ mm}^2$ ) composed of around 25 wires/channel, grouped by construction. Each chamber is equipped with 3 FEBs (Front-End Boards) with 16 pads each.

A channel is a logical combination of a top layer (pads) and a bottom layer readout. These readouts can be combined in AND or OR logics. One can have 8 channels per FEB, each channel being a logical combination of top and bottom pads. In this mode they are called AND2 and OR2. It is also possible to have the FEB configured in a 2 channels mode, each one corresponding to one sixth of the total readout pads. In this mode, all the pads can be combined in OR (called OR8) or they can be AND'ed in top and bottom pads and then group in OR (called OR4AND2). Figures 6.13 and 6.14 presents a logical diagram for each readout mode.

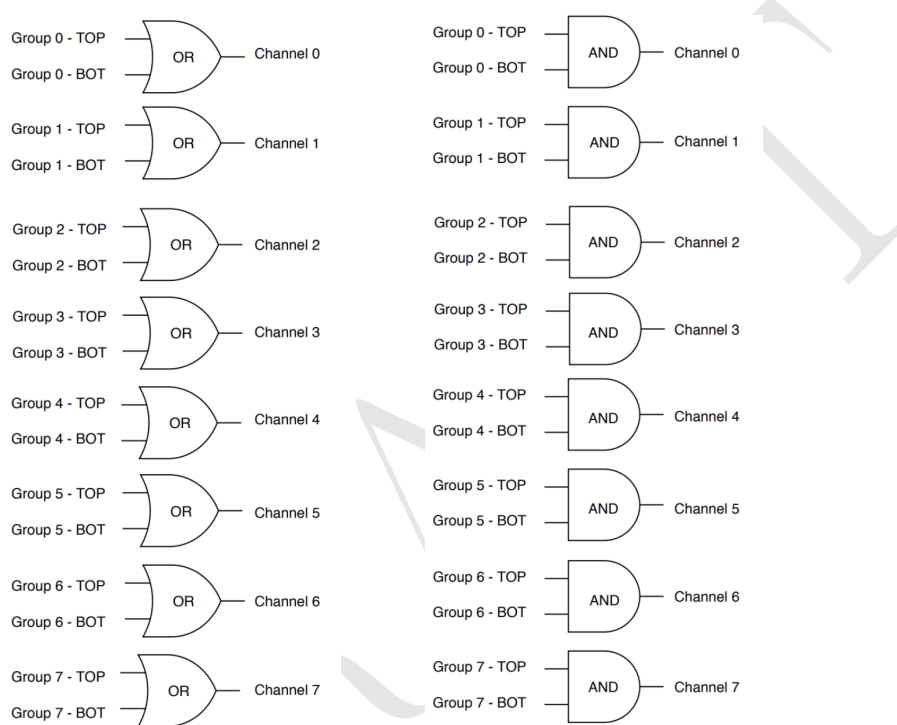


Figure 6.13: FEB configured 8 channels modes. Group should be understood as wire pad. Left: Logical diagram for OR2. Right: Logical diagram for AND2.

The nominal gas mixture for these chambers is Ar/CO<sub>2</sub>/CF<sub>4</sub> (40:55:5). For a matter of simplicity, it was used an already available similar gas line in the same building, used by CMS CSC (Cathode Strip Chamber) [82], which has a similar composition (40:50:10). Optimal conditions are obtained with 2 to 4 liters/hour of gas flux and 2.65 kV of applied voltage.

Figure 6.15 shows the setup that was prepared for commissioning of this chambers. It was mounted two chambers on top of another (chambers A and B) above an RPC R&D chamber and two other chambers on the bottom (chambers C and D). These four MWPC will be used as telescope for the RPC chamber. All the services were mounted in rack, as in Figure 6.15. This includes power supply (low voltage and high voltage), distribution panel, VME crate and boards for FEB control, computer for control (high voltage, and FEB control) and NIM crate and boards for LVDS to NIM signal conversion, logics and counting.

Due to the short amount of time available for the commissioning, only two measurements measurements were made with these chambers. They were meant to be a proof of concept for future activities.

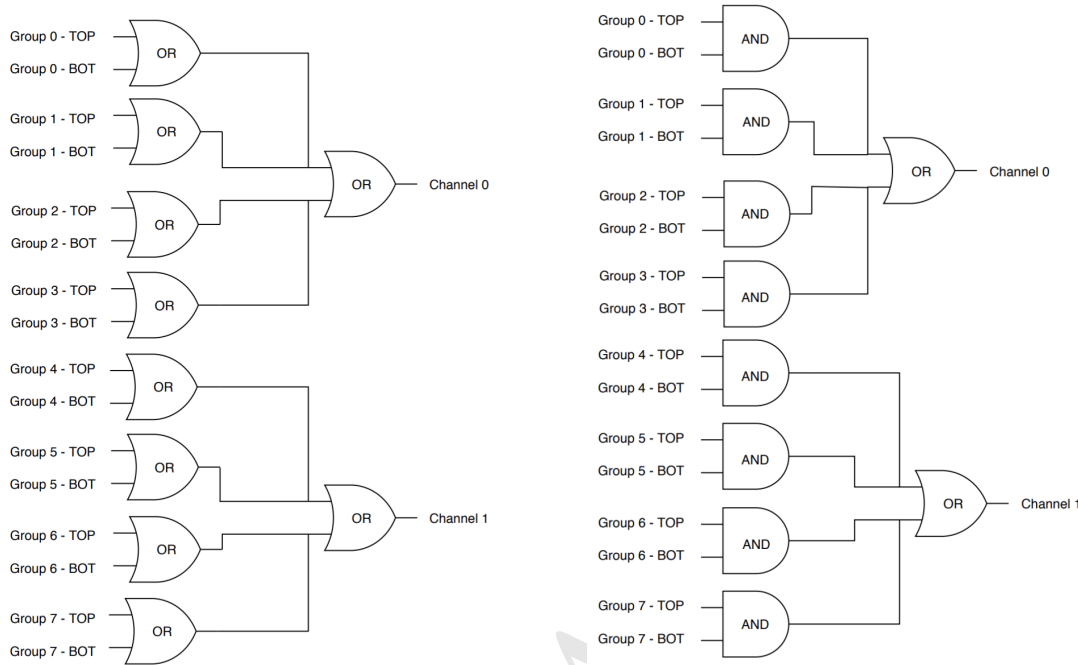


Figure 6.14: FEB configured 2 channels modes. Left: Logical diagram for OR8. Group should be understood as wire pad. Right: Logical diagram for OR4AND2.

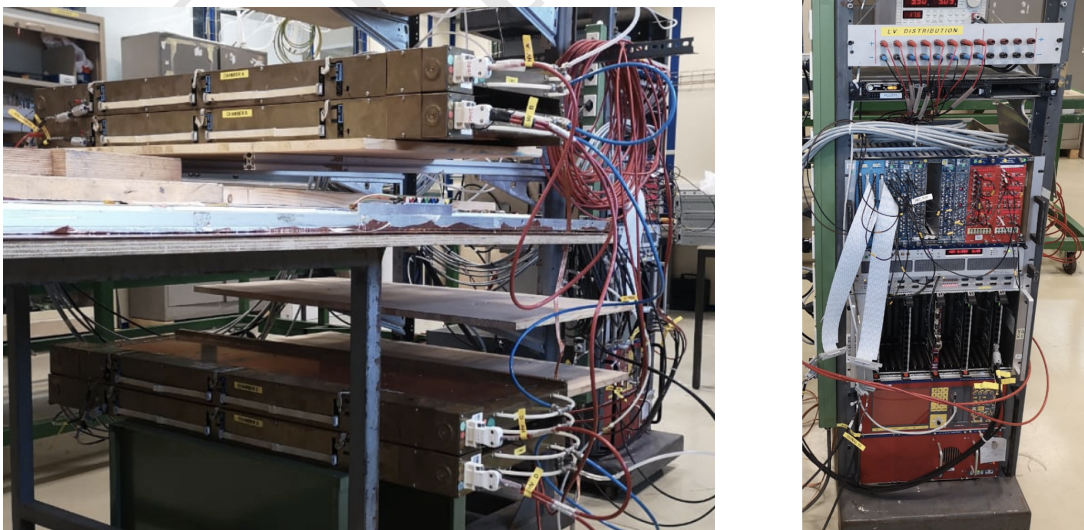


Figure 6.15: Left: Setup mounted for commissioning. Two MWPC chamber on the top (chambers A and B) and two (chambers C and D) on the bottom with a RPC R&D in the middle. Right: Rack with all the services for the operation of these chambers.

The first measurement was to measure the coincidence rate of two chambers as a function of the distance between the two top planes (Figure 6.16). This measurements were done with nominal working point, with one FEB configured in 2 channels mode with 7 pC threshold, in (160 mm x 160 mm) area per chamber. One can observe that, if we go for a telescope trigger in the order of 1 meter of separation between the chamber, the logical combination chosen has negligible effect in the coincidence rate. Also, the fits can be used to estimate the rate in a configuration with chamber on the roof and under the floor. This could be the case of a universal trigger, to be mounted in GIF++ with these chamber.

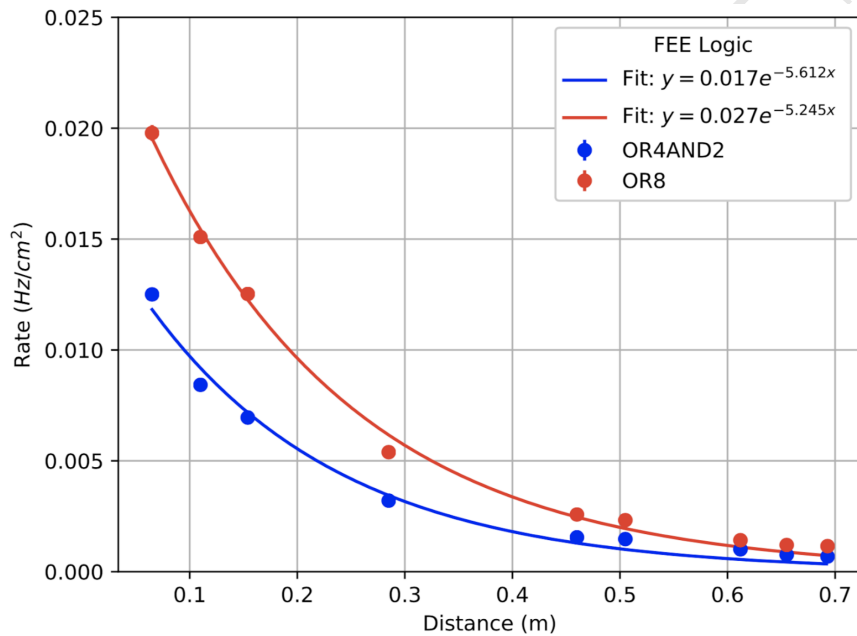


Figure 6.16: Coincidence rate of two chambers with respect to an arbitrary distance between the two top planes. Measured in 10 minutes, for 2 logical combinations (OR8 and OR4AND2). Applied high voltage: 2.65 kV. Threshold: 7 pC. Active area: readout of 160 mm x 160 mm per chamber.

The second measurement consist on evaluate the impact of  $\gamma$  background by placing a small Cs-137 source on top of the chamber A (Figure 6.17). For this measurement, the distance between top planes of each pair of chamber (A to B and C to D) is 65 mm, while the distance between the top planes of A and C is 570 mm. It is clear the the  $\gamma$  source has an impact on chamber A rate, but this is negligible when we take into account the coincidence between two chambers.

This two measurements were enough to validate this chambers as possible trigger pro RPC R&D with cosmic muons in the laboratory and at GIF++. The next steps would be use this MWPC chamber to implement a tracking system from triggering. This would demand some developments, since, due to bandwidth restrictions, the signal from each FEB would have to go to a programmable fast electronics, i.e. a FPGA, which would reconstruct muon tracks and provide the trigger to the DAQ system. This can be done by placing the two pair of chambers (AB and CD) in orthogonal configuration and read the signal in a CAEN V2495 board [104].

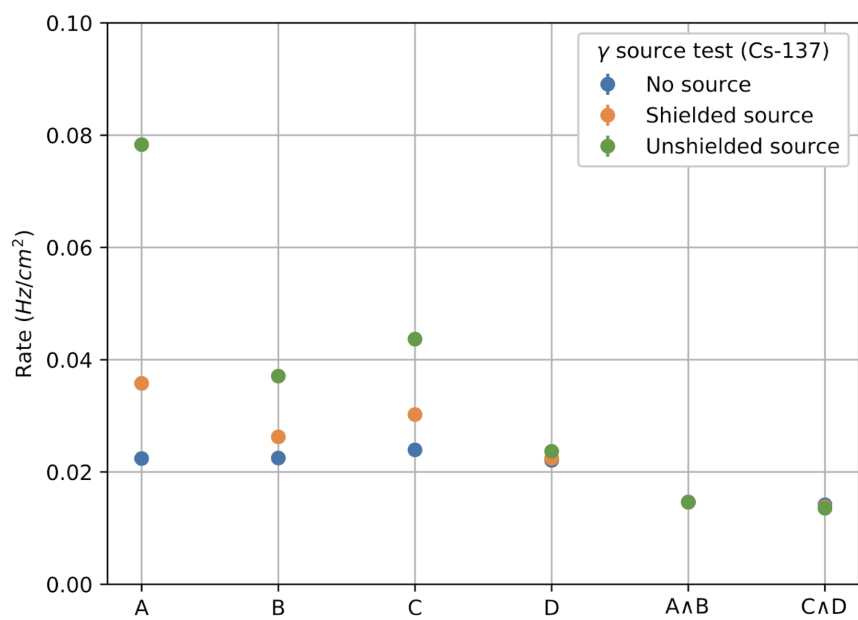


Figure 6.17: Individual rates (chambers A, B, C and D) and coincidence rates for two chambers (A AND B, C AND D), for without  $\gamma$  source (blue), a shielded  $\gamma$  source (orange) and an unshielded  $\gamma$  source (green). Source sitting on top of chamber A. Applied high voltage: 2.65 kV. Threshold: 7 pC. Active area: readout of 160 mm x 320 mm per chamber. Logical combination: AND2

**6.4.2 LS2 and the RPC Standard Maintenance**

In December 2018, the LS2 (Long Shutdown 2) was started. This a period in which the LHC and its detectors (CMS included) stop their operation for maintenance and upgrade. The LS2 will go up to 2021, when LHC and CMS restart the data taking with the Run3.

During the LS2 it is being installed services for the new chambers (gas pipes, low voltage (LV), cables, signal and control optical fibers, high voltage (HV) cable and support equipment, and HV/LV power supplies), as well as continuity to the to the RPC R&D studies, besides the reparation of broken elements of the present system, i.e. chamber in the barrel region which present gas leak problems, maintenance of the LV and HV connectivity and power system, maintenance of the control system of problematic chambers (Front-Ends boards, cabling and Distribution Boards) and the dismount and reinstallation of four stations in the endcap (RE4) on both sides of CMS [105].

What concerns the standard maintenance of the present RPC system, the main LS2 activities in which the student was involved, can be divided in three main tasks: (a) HV maintenance, (b) LV and control maintenance and (c) detector commissioning.

**HV maintenance**

A key factor of and RPC performance is the applied high voltage (HV). The CMS RPC achieve their optimal performance with, around, 9.5 kV applied in each gap. This voltage is in the range of the dielectric breakdown of many gases, which could lead to potential current leakages, if some part of the system is damaged, poorly operated or badly installed. If the currents are high enough this can make impossible the operation of the chamber. In cases like this, during the operation period (data taking), the problematic HV channel is identified and turned off (each chamber has two channels, one for each lawyer of gaps). Chambers in this situation are said to be operating in single gap mode (SG).

The goal for the HV maintenance is to, now that the CMS is off and the chambers are accessible, identify which part of the HV supply system is causing the current leak and fix it the best way possible. Usually the problem is beyond the power supply, very often connectors or the gap itself are damaged.

The CMS RPCs uses two kind of HV connectors, monopolar and tripolar connector. The monopolar are used to connect the chamber to the power supply. If mounted properly, rarely they present problems. The connection to the chamber is made by tripolar connectors, in which the ground and the HV for both gaps arrives to the chamber in a single connector, for simplicity and to save space in the patch panel. Unfortunately these connectors are relatively fragile, and they could be a potential source of leak, specially if they were poorly mounted, badly operated or with aging itself. Also, since this was a connector made exclusively for the CMS RPC system, some design choices had to be improved after the installation of other chamber. Those installed with old batches of tripolar connectors are sensitive ones. The reparation of this connectors consists in isolate the connector from the chamber and power it up to 15 kV (maximum voltage allowed by the system). If the tested connector is broken one will observe a very fast increase in the current of the HV channel. The only solution to this kind of problem is to replace the connector.

On the other hand, if the connector is powered isolated and pass the test, the problem beyond the connector (assuming that the power system have already been tested), i.e. inside the chamber. When a chamber is in SG mode it means that a full layer is off, but not necessarily all the gaps in that layer are bad (a RPC can have up to three per layer). In this situation, the procedure consists in cutting the cables that comes from the gaps to the chamber side connector one by one and identify which gap of the problematic layer is the broken by powering it. Once identified, this gap should isolated and the other ones reconnected. The broken gap is unrecoverable, since it is inside the chamber, but 5% to 10 % of efficiency can be retaken, without changing the applied HV and increasing the longevity of the chamber.

Another contribution to the HV maintenance was the proposal of a procedure to replace the problematic tripolar connector by a monopolar (also called jupiter) connector, which are known for being much more stable and reliable. The figure 6.18 (left) show the designed adapter for the chamber patch panel which would made this change possible. Figure 6.18 (right) shows a tryout of a chamber in which this procedure was tested. The proposal was presented to the RPC community and approved to be used from now on. Technical drawings and instructions were provided.

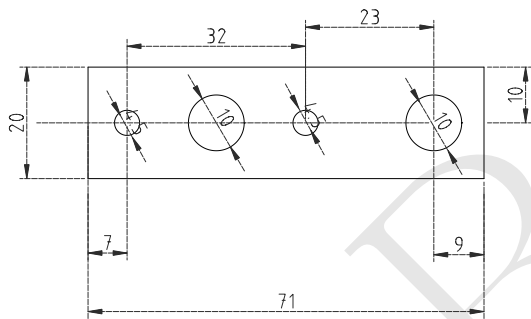


Figure 6.18: Left: Proposed adapter the chamber patch panel which make it possible to replace a tripolar by a jupiter HV connector. Right: Try out of the proposed HV connector replacement.

## 1219 LV and control maintenance

The low voltage (LV) and control maintenance consists in make sure that the Front-End Boards (FEBs) are powered and configurable, which means that the LV power system is working from supply board to the cable, that the signal cables are in good state and properly connected to the chamber and to the link boards and that the on-detector electronics (FEBs and Distribution Boards - DBs) are working fine.

Usually, this system is very reliable. The weak point, in most of the cases, is the detector electronics. When a FEB [106] (as in Figure 6.19) is problematic it can present regions of very high noise or no signal at all (silent), which can not be recovered by the threshold control. In cases like this, when the FEB is accessible, it can be replaced in order to recover efficiency in the problematic chamber. This procedure is done by extracting the chamber from inside the detector (only for barrel chamber) and opening its cover to have access to the problematic component. Removed boards are send back to production labs for refurbishment.

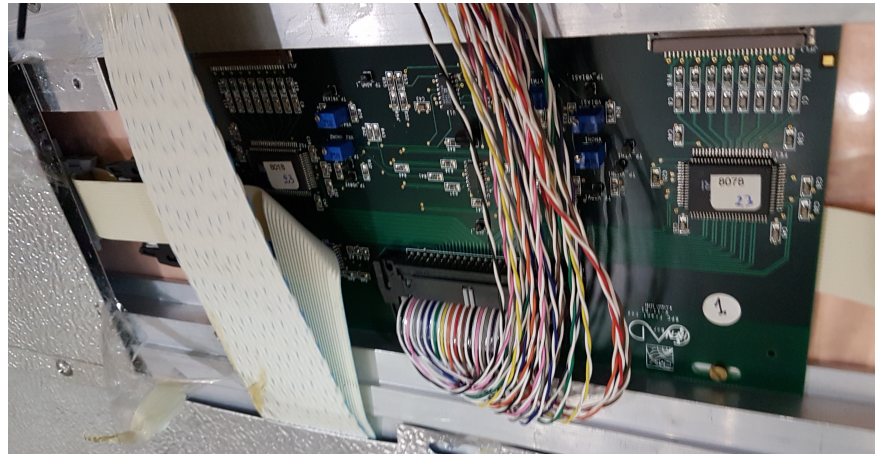


Figure 6.19: RPC Front-end board (FEB) used in the barrel chambers.

1232     The most usual problem is a chamber in which the threshold control was lost. For those chamber,  
 1233     most probably, the problem is in the distribution board of the chamber, which is a piece of hardware  
 1234     responsible for distribute the LV power to the FEBs (3 to 6 per chamber) and send the threshold  
 1235     control signal to the FEBs via I2C line. If a chamber has no threshold control, it means that the  
 1236     RPC operation has no control over the signal selection, which can potentially induce performance  
 1237     issues.

1238     For the barrel this maintenance happens concomitantly with the gas leak reparations on the  
 1239     barrel chamber, since both demands the chamber extraction, which is a complex procedure in terms  
 1240     of operation and demands specialized equipment and manpower. For technical reasons, the gas leak  
 1241     extractions have precedence over LV ones.

## 1242     **Detector commissioning**

1243     All the LS2 activities demands uncabling of the chamber to be repaired and possibly some  
 1244     neighbor chambers. Also, it can involve the replacement of components of the chamber. To avoid  
 1245     damage to the system a compromising procedure is needed after all this activities. Given the  
 1246     responsibilities of the commissioning it was necessary to: (a) make sure that the the RPC system  
 1247     keep tracks of all the interventions, (b) maintain all the algorithms used in the commissioning  
 1248     procedure, (c) together with the RPC Coordination, define a pool of people and a schedule to the  
 1249     commissioning of the system and (d) follow-up, with other CMS RPC experts, the availability of  
 1250     materials and resources for the commissioning operations.

1251     Besides the organizational tasks, the commissioning demanded to establish procedures to ensure  
 1252     the connectivity and functionality of HV and LV connections. For the HV, it is needed to make sure  
 1253     that the chambers are properly connected, without miscabling<sup>4</sup> and that the currents at stand-by  
 1254     HV and working point HV are compatible with the ones in the end of last data-taking (end of  
 1255     2018). This activity will start in November/2019, when the CMS RPC Standard Gas Mixture will  
 1256     be available again.

---

<sup>4</sup>Mixed cable connections.

1257 For the LV point of view, the LV power cable and signal cables should also be properly connected,  
 1258 and presenting a noise profile compatible with last data-taking. One key point for this task is to  
 1259 make sure that there are no miscabling of signal cable. One RPC chamber can have from 6  
 1260 to 18 signal cable, which are connected very close one to another. There is a good chance that a  
 1261 chamber, after reparation, have its signal cables mixed. In order to diagnose situations like this, it  
 1262 was validated a algorithm present in the RPC Online Software, but never used since LS1, which,  
 1263 by changing the threshold of each component of the RPC system, from very high to very low values  
 1264 (component by component), can spot miscabled chambers. Since the control line is independent of  
 1265 the signal line, a mislabeled will present a different noise from what is expected.

1266 Besides the validation of this algorithm, it was also implemented a web system (Figure 6.20),  
 1267 developed in Flask [107] which automatize the execution of the algorithm, making transparent to the  
 1268 shifter (or the one performing the commissioning) the procedure to get miscabling report.

#### FEB Connectivity Test - Analysis

Worker	Date (YY-MM-DD)	Time (HH:MM:SS)	Hash	
RBP2_Far	2019-06-20	23:43:19	387534dst	<button>Run Analyzer</button>
RBP1_Far	2019-06-20	20:12:20	458306dst	<button>Run Analyzer</button>
RBP1_Far	2019-06-20	20:04:46	336162dst	<button>Run Analyzer</button>
RBP1_Near	2019-06-20	19:02:00	377863dst	<button>Run Analyzer</button>
RBP1_Near	2019-06-19	18:59:00	858950dst	<button>Run Analyzer</button>
RBP1_Far	2019-06-19	18:58:26	994787dst	<button>Run Analyzer</button>
YEN3_Far	2019-05-07	10:28:23	176278dst	<button>Run Analyzer</button>
YEN3_Near	2019-05-07	10:28:08	347504dst	<button>Run Analyzer</button>
YEN1_Far	2018-12-07	15:03:24	575561	<button>Run Analyzer</button>
RBO_Far	2018-12-07	14:45:42	101463	<button>Run Analyzer</button>
RBP1_Far	2018-12-07	09:12:00	477689	<button>Run Analyzer</button>

Figure 6.20: RPC FEB Commissioning Analyzer.

1269 The LV commissioning is ongoing, since it happens, as much as possible, right after the chamber  
 1270 reparation.

# 1271 Bibliography

- 1272 [1] Wikimedia Commons. *Standard Model*. 2020. URL: [https://en.wikipedia.org/wiki/File:Standard\\_Model\\_of\\_Elementary\\_Particles.svg](https://en.wikipedia.org/wiki/File:Standard_Model_of_Elementary_Particles.svg).
- 1273
- 1274 [2] C. Patrignani et al. “Review of Particle Physics”. In: *Chin. Phys. C* 40.10 (2016), p. 100001.
- 1275 DOI: 10.1088/1674-1137/40/10/100001.
- 1276 [3] A. Salam and J. C. Ward. “On a gauge theory of elementary interactions”. In: *Il Nuovo Cimento (1955-1965)* 19.1 (1961), pp. 165–170. DOI: 10.1007/BF02812723. URL: <https://doi.org/10.1007/BF02812723>.
- 1277
- 1278
- 1279 [4] G. Aad et al. “Observation of a new particle in the search for the Standard Model Higgs boson with the ATLAS detector at the LHC”. In: *Physics Letters B* 716.1 (2012), pp. 1–29. ISSN: 0370-2693. DOI: <https://doi.org/10.1016/j.physletb.2012.08.020>. URL: <http://www.sciencedirect.com/science/article/pii/S037026931200857X>.
- 1280
- 1281
- 1282
- 1283 [5] Serguei Chatrchyan et al. “Observation of a new boson at a mass of 125 GeV with the CMS experiment at the LHC”. In: *Phys. Lett. B* 716 (2012), pp. 30–61. DOI: 10.1016/j.physletb.2012.08.021. arXiv: 1207.7235 [hep-ex].
- 1284
- 1285
- 1286 [6] Geoffrey Bodwin et al. “Higgs boson decays to quarkonia and the  $H\bar{c}c$  coupling”. In: *Phys. Rev. D* 88 (5 Sept. 2013), p. 053003. DOI: 10.1103/PhysRevD.88.053003. URL: <https://link.aps.org/doi/10.1103/PhysRevD.88.053003>.
- 1287
- 1288
- 1289 [7] Geoffrey T. Bodwin et al. “Relativistic corrections to Higgs boson decays to quarkonia”. In: *Phys. Rev. D* 90 (11 Dec. 2014), p. 113010. DOI: 10.1103/PhysRevD.90.113010. URL: <https://link.aps.org/doi/10.1103/PhysRevD.90.113010>.
- 1290
- 1291
- 1292 [8] G. Aad, B. Abbott, et al. “Combined Measurement of the Higgs Boson Mass in  $pp$  Collisions at  $\sqrt{s} = 7$  and 8 TeV with the ATLAS and CMS Experiments”. In: *Phys. Rev. Lett.* 114 (19 May 2015), p. 191803. DOI: 10.1103/PhysRevLett.114.191803. URL: <https://link.aps.org/doi/10.1103/PhysRevLett.114.191803>.
- 1293
- 1294
- 1295
- 1296 [9] Cédric Delaunay et al. “Enhanced Higgs boson coupling to charm pairs”. In: *Phys. Rev. D* 89 (3 Feb. 2014), p. 033014. DOI: 10.1103/PhysRevD.89.033014. URL: <https://link.aps.org/doi/10.1103/PhysRevD.89.033014>.
- 1297
- 1298
- 1299 [10] M. A. PÉREZ, G. TAVARES-VELASCO, and J. J. TOSCANO. “NEW PHYSICS EFFECTS IN RARE Z DECAYS”. In: *International Journal of Modern Physics A* 19.02 (2004), pp. 159–178. DOI: 10.1142/S0217751X04017100.
- 1300
- 1301

- [11] Grossman, Yuval and König, Matthias and Neubert, Matthias. “Exclusive radiative decays of W and Z bosons in QCD factorization”. In: *Journal of High Energy Physics* 2015.4 (Apr. 2015), p. 101. ISSN: 1029-8479. DOI: 10.1007/JHEP04(2015)101. URL: [https://doi.org/10.1007/JHEP04\(2015\)101](https://doi.org/10.1007/JHEP04(2015)101).
- [12] Geoffrey T. Bodwin et al. “Z-boson decays to a vector quarkonium plus a photon”. In: *Phys. Rev. D* 97 (1 Jan. 2018), p. 016009. DOI: 10.1103/PhysRevD.97.016009. URL: <https://link.aps.org/doi/10.1103/PhysRevD.97.016009>.
- [13] Geoffrey T. Bodwin et al. “Addendum: New approach to the resummation of logarithms in Higgs-boson decays to a vector quarkonium plus a photon [Phys. Rev. D 95, 054018 (2017)]”. In: *Phys. Rev. D* 96 (11 Dec. 2017), p. 116014. DOI: 10.1103/PhysRevD.96.116014. URL: <https://link.aps.org/doi/10.1103/PhysRevD.96.116014>.
- [14] Gino Isidori, Aneesh V. Manohar, and Michael Trott. “Probing the nature of the Higgs-like boson via  $h \rightarrow Vf$  decays”. In: *Physics Letters B* 728 (2014), pp. 131–135. ISSN: 0370-2693. DOI: <https://doi.org/10.1016/j.physletb.2013.11.054>. URL: <http://www.sciencedirect.com/science/article/pii/S037026931300960X>.
- [15] Alexander L. Kagan et al. “Exclusive Window onto Higgs Yukawa Couplings”. In: *Phys. Rev. Lett.* 114 (10 Mar. 2015), p. 101802. DOI: 10.1103/PhysRevLett.114.101802. URL: <https://link.aps.org/doi/10.1103/PhysRevLett.114.101802>.
- [16] Dao-Neng Gao. “A note on Higgs decays into Z boson and  $J/\psi(\Upsilon)$ ”. In: *Physics Letters B* 737 (2014), pp. 366–368. ISSN: 0370-2693. DOI: <https://doi.org/10.1016/j.physletb.2014.09.019>. URL: <http://www.sciencedirect.com/science/article/pii/S0370269314006698>.
- [17] A. M. Sirunyan et al. “Observation of Higgs Boson Decay to Bottom Quarks”. In: *Phys. Rev. Lett.* 121 (12 Sept. 2018), p. 121801. DOI: 10.1103/PhysRevLett.121.121801. URL: <https://link.aps.org/doi/10.1103/PhysRevLett.121.121801>.
- [18] G Apollinari et al. *High-Luminosity Large Hadron Collider (HL-LHC): Preliminary Design Report*. CERN Yellow Reports: Monographs. Geneva: CERN, 2015. DOI: 10.5170/CERN-2015-005. URL: <https://cds.cern.ch/record/2116337>.
- [19] The ATLAS Collaboration et al. “The ATLAS Experiment at the CERN Large Hadron Collider”. In: *Journal of Instrumentation* 3.08 (Aug. 2008), S08003–S08003. DOI: 10.1088/1748-0221/3/08/s08003. URL: <https://doi.org/10.1088%2F1748-0221%2F3%2F08%2Fs08003>.
- [20] G. Aad et al. “Search for Higgs and Z Boson Decays to  $J/\psi\gamma$  and  $\Upsilon(nS)\gamma$  with the ATLAS Detector”. In: *Phys. Rev. Lett.* 114 (12 Mar. 2015), p. 121801. DOI: 10.1103/PhysRevLett.114.121801. URL: <https://link.aps.org/doi/10.1103/PhysRevLett.114.121801>.
- [21] Morad Aaboud et al. “Searches for exclusive Higgs and Z boson decays into  $J/\psi\gamma$ ,  $\psi(2S)\gamma$ , and  $\Upsilon(nS)\gamma$  at  $\sqrt{s} = 13$  TeV with the ATLAS detector”. In: *Phys. Lett. B* 786 (2018), pp. 134–155. DOI: 10.1016/j.physletb.2018.09.024. arXiv: 1807.00802 [hep-ex].
- [22] S. Chatrchyan et al. “The CMS experiment at the CERN LHC”. In: *JINST* 3 (2008), S08004. DOI: 10.1088/1748-0221/3/08/S08004.

- [23] Albert M Sirunyan et al. “Search for rare decays of Z and Higgs bosons to  $J/\psi$  and a photon in proton-proton collisions at  $\sqrt{s} = 13$  TeV”. In: *Eur. Phys. J.* C79.2 (2019), p. 94. DOI: 10.1140/epjc/s10052-019-6562-5. arXiv: 1810.10056 [hep-ex].
- [24] Albert M Sirunyan et al. “Search for Higgs and Z boson decays to  $J/\psi$  or  $\Upsilon$  pairs in proton-proton collisions at  $\sqrt{s} = 13$  TeV”. In: *Phys. Lett. B* 797.arXiv:1905.10408. CMS-HIG-18-025-003 (May 2019). All figures and tables can be found at <http://cms-results.web.cern.ch/cms-results/public-results/publications/HIG-18-025> (CMS Public Pages), 134811. 31 p. DOI: 10.1016/j.physletb.2019.134811. URL: <https://cds.cern.ch/record/2676242>.
- [25] Albert M. Sirunyan et al. “Observation of the  $Z \rightarrow \psi\ell^+\ell^-$  decay in pp collisions at  $\sqrt{s} = 13$  TeV”. In: *Phys. Rev. Lett.* 121.arXiv:1806.04213. CMS-BPH-16-001-003 (June 2018). Submitted to Phys.Rev.Lett., 141801. 17 p. DOI: 10.1103/PhysRevLett.121.141801. URL: <https://cds.cern.ch/record/2623687>.
- [26] Serguei Chatrchyan et al. “Description and performance of track and primary-vertex reconstruction with the CMS tracker”. In: *JINST* 9 (2014), P10009. DOI: 10.1088/1748-0221/9/10/P10009. arXiv: 1405.6569 [physics.ins-det].
- [27] Vardan Khachatryan et al. “Performance of electron reconstruction and selection with the CMS detector in proton-proton collisions at  $\sqrt{s} = 8$  TeV”. In: *JINST* 10 (2015), P06005. DOI: 10.1088/1748-0221/10/06/P06005. arXiv: 1502.02701 [physics.ins-det].
- [28] Vardan Khachatryan et al. “Performance of photon reconstruction and identification with the CMS detector in proton-proton collisions at  $\sqrt{s} = 8$  TeV”. In: *JINST* 10 (2015), P08010. DOI: 10.1088/1748-0221/10/08/P08010. arXiv: 1502.02702 [physics.ins-det].
- [29] A M Sirunyan et al. “Performance of the CMS muon detector and muon reconstruction with proton-proton collisions at  $\sqrt{s} = 13$  TeV”. In: *JINST* 13 (2018), P06015. DOI: 10.1088/1748-0221/13/06/P06015. arXiv: 1804.04528 [physics.ins-det].
- [30] Vardan Khachatryan et al. “The CMS trigger system”. In: *JINST* 12 (2017), P01020. DOI: 10.1088/1748-0221/12/01/P01020. arXiv: 1609.02366 [physics.ins-det].
- [31] S. Chatrchyan et al. “The CMS experiment at the CERN LHC”. In: *JINST* 3 (2008), S08004. DOI: 10.1088/1748-0221/3/08/S08004.
- [32] *CMS Luminosity Measurements for the 2016 Data Taking Period*. Tech. rep. CMS-PAS-LUM-17-001. Geneva: CERN, 2017. URL: <https://cds.cern.ch/record/2257069>.
- [33] S. Agostinelli et al. “GEANT4—a simulation toolkit”. In: A506 (2003), pp. 250–303. DOI: 10.1016/S0168-9002(03)01368-8.
- [34] Paolo Nason. “A New method for combining NLO QCD with shower Monte Carlo algorithms”. In: *JHEP* 11 (2004), p. 040. DOI: 10.1088/1126-6708/2004/11/040. arXiv: hep-ph/0409146 [hep-ph].
- [35] Stefano Frixione, Paolo Nason, and Carlo Oleari. “Matching NLO QCD computations with Parton Shower simulations: the POWHEG method”. In: *JHEP* 11 (2007), p. 070. DOI: 10.1088/1126-6708/2007/11/070. arXiv: 0709.2092 [hep-ph].

- [36] Simone Alioli et al. “A general framework for implementing NLO calculations in shower Monte Carlo programs: the POWHEG BOX”. In: *JHEP* 06 (2010), p. 043. DOI: 10.1007/JHEP06(2010)043. arXiv: 1002.2581 [hep-ph].
- [37] Abdelhak Djouadi. “The anatomy of electroweak symmetry breaking: Tome I: The Higgs boson in the Standard Model”. In: *Physics Reports* 457.1 (2008), pp. 1–216. ISSN: 0370-1573. DOI: <https://doi.org/10.1016/j.physrep.2007.10.004>. URL: <http://www.sciencedirect.com/science/article/pii/S0370157307004334>.
- [38] Torbjörn Sjöstrand, Stephen Mrenna, and Peter Skands. “A brief introduction to PYTHIA 8.1”. In: *Computer Physics Communications* 178.11 (2008), pp. 852–867. ISSN: 0010-4655. DOI: <https://doi.org/10.1016/j.cpc.2008.01.036>. URL: <http://www.sciencedirect.com/science/article/pii/S0010465508000441>.
- [39] Torbjörn Sjöstrand et al. “An Introduction to PYTHIA 8.2”. In: *Comput. Phys. Commun.* 191 (2015), pp. 159–177. DOI: 10.1016/j.cpc.2015.01.024. arXiv: 1410.3012 [hep-ph].
- [40] Vardan Khachatryan et al. “Event generator tunes obtained from underlying event and multiparton scattering measurements”. In: *Eur. Phys. J. C* 76.3 (2016), p. 155. DOI: 10.1140/epjc/s10052-016-3988-x. arXiv: 1512.00815 [hep-ex].
- [41] The NNPDF collaboration et al. “Parton distributions for the LHC run II”. In: *Journal of High Energy Physics* 2015.4 (Apr. 2015), p. 40. ISSN: 1029-8479. DOI: 10.1007/JHEP04(2015)040. URL: [https://doi.org/10.1007/JHEP04\(2015\)040](https://doi.org/10.1007/JHEP04(2015)040).
- [42] J. Alwall et al. “The automated computation of tree-level and next-to-leading order differential cross sections, and their matching to parton shower simulations”. In: *Journal of High Energy Physics* 2014.7 (July 2014), p. 79. ISSN: 1029-8479. DOI: 10.1007/JHEP07(2014)079. URL: [https://doi.org/10.1007/JHEP07\(2014\)079](https://doi.org/10.1007/JHEP07(2014)079).
- [43] Ali Abbasabadi et al. “Radiative Higgs boson decays  $H \rightarrow f\bar{f}\gamma$ ”. In: *Phys. Rev. D* 55 (9 May 1997), pp. 5647–5656. DOI: 10.1103/PhysRevD.55.5647. URL: <https://link.aps.org/doi/10.1103/PhysRevD.55.5647>.
- [44] D. de Florian et al. *Handbook of LHC Higgs Cross Sections: 4. Deciphering the Nature of the Higgs Sector*. CERN Yellow Reports: Monographs. 869 pages, 295 figures, 248 tables and 1645 citations. Working Group web page: <https://twiki.cern.ch/twiki/bin/view/LHCPhysics/LHCHXSWG>. Oct. 2016. DOI: 10.23731/CYRM-2017-002. URL: <https://cds.cern.ch/record/2227475>.
- [45] Ye Li and Frank Petriello. “Combining QCD and electroweak corrections to dilepton production in the framework of the FEWZ simulation code”. In: *Phys. Rev. D* 86 (9 Nov. 2012), p. 094034. DOI: 10.1103/PhysRevD.86.094034. URL: <https://link.aps.org/doi/10.1103/PhysRevD.86.094034>.
- [46] John M. Campbell and R.K. Ellis. “MCFM for the Tevatron and the LHC”. In: *Nuclear Physics B - Proceedings Supplements* 205-206 (2010). Loops and Legs in Quantum Field Theory, pp. 10–15. ISSN: 0920-5632. DOI: <https://doi.org/10.1016/j.nuclphysbps.2010.08.011>. URL: <http://www.sciencedirect.com/science/article/pii/S0920563210001945>.

- [47] Vardan Khachatryan et al. “Search for a Higgs boson decaying into  $\gamma^*\gamma \rightarrow \ell\ell\gamma$  with low dilepton mass in pp collisions at  $\sqrt{s} = 8$  TeV”. In: *Phys. Lett.* B753 (2016), pp. 341–362. DOI: 10.1016/j.physletb.2015.12.039. arXiv: 1507.03031 [hep-ex].
- [48] N. Brambilla, S. Eidelman, B.K. Heltsley, et al. “Heavy quarkonium: progress, puzzles, and opportunities”. In: *The European Physical Journal C* 71.2 (Feb. 2011), p. 1534. ISSN: 1434-6052. DOI: 10.1140/epjc/s10052-010-1534-9. URL: <https://doi.org/10.1140/epjc/s10052-010-1534-9>.
- [49] Sandro Palestini. “Angular distribution and rotations of frame in vector meson decays into lepton pairs”. In: *Phys. Rev. D* 83 (3 Feb. 2011), p. 031503. DOI: 10.1103/PhysRevD.83.031503. URL: <https://link.aps.org/doi/10.1103/PhysRevD.83.031503>.
- [50] A.M. Sirunyan et al. “Particle-flow reconstruction and global event description with the CMS detector”. In: *Journal of Instrumentation* 12.10 (2017), P10003. URL: <http://stacks.iop.org/1748-0221/12/i=10/a=P10003>.
- [51] Matteo Cacciari, Gavin P. Salam, and Gregory Soyez. “The anti- $k_t$  jet clustering algorithm”. In: *JHEP* 04 (2008), p. 063. DOI: 10.1088/1126-6708/2008/04/063. arXiv: 0802.1189 [hep-ex].
- [52] Matteo Cacciari, Gavin P. Salam, and Gregory Soyez. “FastJet User Manual”. In: *Eur. Phys. J.* C72 (2012), p. 1896. DOI: 10.1140/epjc/s10052-012-1896-2. arXiv: 1111.6097 [hep-ph].
- [53] Albert M Sirunyan et al. “Measurements of properties of the Higgs boson decaying into the four-lepton final state in pp collisions at  $\sqrt{s} = 13$  TeV”. In: *JHEP* 11 (2017), p. 047. DOI: 10.1007/JHEP11(2017)047. arXiv: 1706.09936 [hep-ex].
- [54] V. Khachatryan et al. “Observation of the diphoton decay of the Higgs boson and measurement of its properties”. In: *The European Physical Journal C* 74.10 (Oct. 2014), p. 3076. ISSN: 1434-6052. DOI: 10.1140/epjc/s10052-014-3076-z. URL: <https://doi.org/10.1140/epjc/s10052-014-3076-z>.
- [55] S. Bernstein. “Démonstration du théorème de Weierstrass fondée sur le calcul des probabilités”. In: *Commun. Soc. Math. Kharkov* 13.1–2 (1912).
- [56] John Erthal Gaiser. “Charmonium Spectroscopy From Radiative Decays of the  $J/\psi$  and  $\psi'$ ”. PhD thesis. SLAC, 1982. URL: <http://www-public.slac.stanford.edu/sciDoc/docMeta.aspx?slacPubNumber=slac-r-255.html>.
- [57] P. D. Dauncey et al. “Handling uncertainties in background shapes: the discrete profiling method”. In: *JINST* 10.04 (2015), P04015. DOI: 10.1088/1748-0221/10/04/P04015. arXiv: 1408.6865 [physics.data-an].
- [58] S. S. Wilks. “The Large-Sample Distribution of the Likelihood Ratio for Testing Composite Hypotheses”. In: *Ann. Math. Statist.* 9.1 (Mar. 1938), pp. 60–62. DOI: 10.1214/aoms/1177732360. URL: <https://doi.org/10.1214/aoms/1177732360>.

- [59] Higgs to Gamma Gamma Working Group. *Further measurement of  $H \rightarrow \gamma\gamma$  at  $\sqrt{13}$  TeV*. CMS Note 2016/209. CERN, 2016. URL: [http://cms.cern.ch/iCMS/jsp/db\\_notes/noteInfo.jsp?cmsnoteid=CMSSW\\_20AN-2016/209](http://cms.cern.ch/iCMS/jsp/db_notes/noteInfo.jsp?cmsnoteid=CMSSW_20AN-2016/209).
- [60] *Updated measurements of Higgs boson production in the diphoton decay channel at  $\sqrt{s} = 13$  TeV in pp collisions at CMS*. Tech. rep. CMS-PAS-HIG-16-020. Geneva: CERN, 2016. URL: <http://cds.cern.ch/record/2205275>.
- [61] D. de Florian et al. “Handbook of LHC Higgs Cross Sections: 4. Deciphering the Nature of the Higgs Sector”. In: (2016). DOI: 10.23731/CYRM-2017-002. arXiv: 1610.07922 [hep-ph].
- [62] Jon Butterworth et al. “PDF4LHC recommendations for LHC Run II”. In: *J. Phys.* G43 (2016), p. 023001. DOI: 10.1088/0954-3899/43/2/023001. arXiv: 1510.03865 [hep-ph].
- [63] A. D. Martin et al. “Parton distributions for the LHC”. In: *Eur. Phys. J.* C63 (2009), pp. 189–285. DOI: 10.1140/epjc/s10052-009-1072-5. arXiv: 0901.0002 [hep-ph].
- [64] Hung-Liang Lai et al. “New parton distributions for collider physics”. In: *Phys. Rev.* D82 (2010), p. 074024. DOI: 10.1103/PhysRevD.82.074024. arXiv: 1007.2241 [hep-ph].
- [65] Sergey Alekhin et al. “The PDF4LHC Working Group Interim Report”. In: (2011). arXiv: 1101.0536 [hep-ph].
- [66] Michiel Botje et al. “The PDF4LHC Working Group Interim Recommendations”. In: (2011). arXiv: 1101.0538 [hep-ph].
- [67] Richard D. Ball et al. “Impact of Heavy Quark Masses on Parton Distributions and LHC Phenomenology”. In: *Nucl. Phys.* B849 (2011), pp. 296–363. DOI: 10.1016/j.nuclphysb.2011.03.021. arXiv: 1101.1300 [hep-ph].
- [68] Giampiero Passarino. “Higgs Boson Production and Decay: Dalitz Sector”. In: *Phys. Lett.* B727 (2013), pp. 424–431. DOI: 10.1016/j.physletb.2013.10.052. arXiv: 1308.0422 [hep-ph].
- [69] A.M. Sirunyan et al. “Performance of the CMS muon detector and muon reconstruction with proton-proton collisions at  $\sqrt{s}=13$  TeV”. In: *Journal of Instrumentation* 13.06 (June 2018), P06015–P06015. DOI: 10.1088/1748-0221/13/06/p06015. URL: <https://doi.org/10.1088/1748-0221/13/06/p06015>.
- [70] Vardan Khachatryan et al. “Performance of photon reconstruction and identification with the CMS detector in proton-proton collisions at  $\sqrt{s} = 8$  TeV”. In: *JINST* 10.CMS-EGM-14-001. CMS-EGM-14-001. CERN-PH-EP-2015-006 (Feb. 2015). Comments: Submitted to JINST, P08010. 59 p. DOI: 10.1088/1748-0221/10/08/P08010. URL: <http://cds.cern.ch/record/1988093>.
- [71] A L Read. “Presentation of search results: the CL<sub>s</sub> technique”. In: *Journal of Physics G: Nuclear and Particle Physics* 28.10 (Sept. 2002), pp. 2693–2704. DOI: 10.1088/0954-3899/28/10/313. URL: <https://doi.org/10.1088/0954-3899/28/10/313>.

- [72] J. Neyman and E. S. Pearson. "On the Problem of the Most Efficient Tests of Statistical Hypotheses". In: *Philosophical Transactions of the Royal Society of London. Series A, Containing Papers of a Mathematical or Physical Character* 231 (1933), pp. 289–337. ISSN: 02643952. URL: <http://www.jstor.org/stable/91247>.
- [73] Glen Cowan et al. "Asymptotic formulae for likelihood-based tests of new physics". In: *The European Physical Journal C* 71.2 (Feb. 2011), p. 1554. ISSN: 1434-6052. DOI: 10.1140/epjc/s10052-011-1554-0. URL: <https://doi.org/10.1140/epjc/s10052-011-1554-0>.
- [74] *Procedure for the LHC Higgs boson search combination in Summer 2011*. Tech. rep. CMS-NOTE-2011-005. ATL-PHYS-PUB-2011-11. Geneva: CERN, Aug. 2011. URL: <https://cds.cern.ch/record/1379837>.
- [75] David H. Annis. "Kendall's Advanced Theory of Statistics, Vol. 1: Distribution Theory (6th ed.). Alan Stuart and J. Keith Ord; Kendall's Advanced Theory of Statistics, Vol. 2A: Classical Inference and the Linear Model (6th ed.). Alan Stuart and J. Keith Ord, and Steven F. Arnold". In: *Journal of the American Statistical Association* 101 (2006), pp. 1721–1721. URL: <https://EconPapers.repec.org/RePEc:bes:jnlasa:v:101:y:2006:p:1721-1721>.
- [76] *Procedure for the LHC Higgs boson search combination in Summer 2011*. Tech. rep. CMS-NOTE-2011-005. ATL-PHYS-PUB-2011-11. Geneva: CERN, Aug. 2011. URL: <https://cds.cern.ch/record/1379837>.
- [77] M. Aaboud et al. "Searches for exclusive Higgs and  $Z$  boson decays into  $J/\psi\gamma$ ,  $\psi(2S)\gamma$ , and  $\Upsilon(nS)\gamma$  at  $\sqrt{s} = 13\text{TeV}$  with the ATLAS detector". In: *Physics Letters B* 786 (Nov. 2018), pp. 134–155. ISSN: 0370-2693. DOI: 10.1016/j.physletb.2018.09.024. URL: <http://dx.doi.org/10.1016/j.physletb.2018.09.024>.
- [78] R. Santonico and R. Cardarelli. "Development of resistive plate counters". In: *Nuclear Instruments and Methods in Physics Research* 187.2 (1981), pp. 377–380. ISSN: 0167-5087. DOI: [https://doi.org/10.1016/0029-554X\(81\)90363-3](https://doi.org/10.1016/0029-554X(81)90363-3). URL: <http://www.sciencedirect.com/science/article/pii/0029554X81903633>.
- [79] Marcello Abbrescia, Paulo Fonte, and Vladimir Peskov. *Resistive gaseous detectors: designs, performance, and perspectives*. Weinheim: Wiley-VCH, 2018. DOI: 10.1002/9783527698691.
- [80] A Beroual and I Fofana. "The background of air gap discharge theory". In: *Discharge in Long Air Gaps*. 2053-2563. IOP Publishing, 2016, 2-1 to 2-22. ISBN: 978-0-7503-1236-3. DOI: 10.1088/978-0-7503-1236-3ch2. URL: <http://dx.doi.org/10.1088/978-0-7503-1236-3ch2>.
- [81] Leonard B. Loeb and John M. Meek. "The Mechanism of Spark Discharge in Air at Atmospheric Pressure. I". In: *Journal of Applied Physics* 11.6 (1940), pp. 438–447. DOI: 10.1063/1.1712792. eprint: <https://doi.org/10.1063/1.1712792>. URL: <https://doi.org/10.1063/1.1712792>.
- [82] *The CMS muon project: Technical Design Report*. Technical Design Report CMS. Geneva: CERN, 1997. URL: <https://cds.cern.ch/record/343814>.

- [83] Dong Hyun, Kim. "Work on CMS Muon Detector (RPC) during Long Shutdown 1 (LS1) - Point 5, Cessy, CMS cavern". CMS Collection. May 2015. URL: <https://cds.cern.ch/record/2016815>.
- [84] P. Bernardini et al. "Precise measurements of drift velocities in helium gas mixtures". In: *Nuclear Instruments and Methods in Physics Research Section A: Accelerators, Spectrometers, Detectors and Associated Equipment* 355.2 (1995), pp. 428–433. ISSN: 0168-9002. DOI: [https://doi.org/10.1016/0168-9002\(94\)01144-3](https://doi.org/10.1016/0168-9002(94)01144-3). URL: <http://www.sciencedirect.com/science/article/pii/0168900294011443>.
- [85] E. Gorini et al. "Drift velocity measurements in C<sub>2</sub>H<sub>2</sub>F<sub>4</sub> based mixtures". In: *Proceedings of the 4th International Workshop on Resistive Plate Chamber and Related Detectors, in Napoli, Italy, 15-16 October* (1997).
- [86] G. Bressi et al. "AN APPARATUS TO SEARCH FOR FREE NEUTRON ANTI-NEUTRON OSCILLATIONS". In: *Nucl. Instrum. Meth. A* 261 (1987), pp. 449–461. DOI: [10.1016/0168-9002\(87\)90353-6](https://doi.org/10.1016/0168-9002(87)90353-6).
- [87] H.L. Ge et al. "The production of residual nuclides in Pb irradiated by 400 MeV/u carbon ions". In: *Nucl. Instrum. Meth. B* 337 (2014), pp. 34–38. DOI: [10.1016/j.nimb.2014.07.024](https://doi.org/10.1016/j.nimb.2014.07.024).
- [88] M. Abbrescia et al. "A Horizontal muon telescope implemented with resistive plate chambers". In: *Nucl. Instrum. Meth. A* 336 (1993), pp. 322–329. DOI: [10.1016/0168-9002\(93\)91116-5](https://doi.org/10.1016/0168-9002(93)91116-5).
- [89] L. Antoniazzi et al. "The E771 RPC muon detector". In: *Nucl. Instrum. Meth. A* 315 (1992), pp. 92–94. DOI: [10.1016/0168-9002\(92\)90686-X](https://doi.org/10.1016/0168-9002(92)90686-X).
- [90] A. Di Ciaccio et al. "Muon tracking and hadron punchthrough measurements using resistive plate chambers". In: *Nucl. Instrum. Meth. A* 315 (1992), pp. 102–108. DOI: [10.1016/0168-9002\(92\)90688-Z](https://doi.org/10.1016/0168-9002(92)90688-Z).
- [91] R. de Asmundis. "Performances of the RPC trigger system in the L3 experiment". In: *3rd International Workshop on Resistive Plate Chambers and Related Detectors (RPC 95)*. 1995, pp. 139–155.
- [92] D. Boutigny et al. "BaBar technical design report". In: (Mar. 1995).
- [93] Andrea Gelmi. *Longevity studies for the CMS-RPC system*. Tech. rep. CMS-CR-2018-136. Geneva: CERN, July 2018. URL: <https://cds.cern.ch/record/2634505>.
- [94] M.A. Shah et al. "Experiences from the RPC data taking during the CMS RUN-2". In: *15th Workshop on Resistive Plate Chambers and Related Detectors*. May 2020. arXiv: [2005.12532 \[physics.ins-det\]](https://arxiv.org/abs/2005.12532).
- [95] *Public CMS Data Quality Information*. twiki.cern.ch/twiki/bin/view/CMSPublic/DataQuality. Acessado em: 20/02/2018.
- [96] Johannes Guteleber, Steven Murray, and Luciano Orsini. "Towards a homogeneous architecture for high-energy physics data acquisition systems". In: *Computer Physics Communications* 153.2 (2003), pp. 155–163. ISSN: 0010-4655. DOI: [https://doi.org/10.1016/S0010-4655\(03\)00161-9](https://doi.org/10.1016/S0010-4655(03)00161-9). URL: <http://www.sciencedirect.com/science/article/pii/S0010465503001619>.

- 1567 [97] *Dojo*. <https://dojotoolkit.org/>. Acessado em: 20/02/2018.
- 1568 [98] *Polymer Project*. Acessado em: 20/02/2018.
- 1569 [99] M. I. Pedraza-Morales. *RPC upgrade project for CMS Phase II*. 2018. arXiv: 1806.11503  
1570 [physics.ins-det].
- 1571 [100] Dorothea Pfeiffer et al. “The radiation field in the Gamma Irradiation Facility GIF++ at  
1572 CERN”. In: *Nuclear Instruments and Methods in Physics Research Section A: Accelerators,*  
1573 *Spectrometers, Detectors and Associated Equipment* 866 (2017), pp. 91–103. ISSN: 0168-9002.  
1574 DOI: <https://doi.org/10.1016/j.nima.2017.05.045>. URL: <http://www.sciencedirect.com/science/article/pii/S0168900217306113>.
- 1576 [101] A. Augusto Alves Jr. et al. “The LHCb Detector at the LHC”. In: *JINST* 3 (2008), S08005.  
1577 DOI: 10.1088/1748-0221/3/08/S08005.
- 1578 [102] Georges Charpak et al. “The Use of Multiwire Proportional Counters to Select and Localize  
1579 Charged Particles”. In: *Nucl. Instrum. Meth.* 62 (1968), pp. 262–268. DOI: 10.1016/0029-  
1580 554X(68)90371-6.
- 1581 [103] *LHCb Muon Group Home Page*. [Online; accessed 1-October-2019]. 2019. URL: <http://lhcb-muon.web.cern.ch/lhcb-muon/>.
- 1583 [104] *CAEN Programmable Logic Unit - V2495*. [Online; accessed 1-October-2019]. 2019. URL:  
1584 <https://www.caen.it/products/v2495/>.
- 1585 [105] *Resistive Plate Chambers are getting dolled up*. <https://cms.cern/news/resistive-plate-chambers-are-getting-dolled>. Acessado em: 20/09/2019.
- 1587 [106] C. Binetti et al. “A new Front-End board for RPC detector of CMS”. In: (Sept. 1999).
- 1588 [107] *Flask (web framework)*. [Online; accessed 1-October-2019]. 2019. URL: <https://palletsprojects.com/p/flask/>.